TEMPERATURE AND VELOCITY MEASUREMENTS IN SUB-COOLED BOILING THROUGH A VERTICAL RECTANGULAR TEST CHANNEL

A Dissertation

by

BANDAR ABDULLAH S. ALKHUDHIRI

Submitted to the Office of Graduate and Professional Studies of
Texas A&M University
in partial fulfillment of the requirements for the degree of

DOCTOR OF PHILOSOPHY

Chair of Committee,	Yassin Hassan
Committee Members,	Nagamangala Anand
	Maria King
	Rodolfo Vaghetto
Head of Department,	Andreas Polycarpou

August 2019

Major Subject: Mechanical Engineering

ABSTRACT

Temperature and velocity measurements are performed in sub-cooled boiling experiments through a single-heated side rectangular test channel at various conditions. The temperature measurements involve the use of the Laser Induced Fluorescence (LIF) method with one heated single-phase (3.9 kw/m^2) and two boiling conditions (30.9 and 36.6 kw/m^2). Two flow rates are considered, for each heating level, and given by the Reynold's number (Re) of 8121 and 20523. For the boiling cases, bubbles are allowed to slide along the heated surface and temperature fields are obtained along the bubbles sliding distance in the axial direction. Radial temperature profiles are mapped out to display the temperature distributions at various axial locations. The resultant temperature fields reveal insightful information about the temperature distribution in each condition. Boiling bubbles induce major changes to the temperature fields. In regions far from the heated wall, the temperature profiles are seen to fall within the range of the bulk fluid temperature values (21.6 ºC ± 1 ºC), as registered by the means of thermocouples. A large increase in temperature is observed near the heated wall (and at the sliding distance) to approximately 29.6 ºC ± 2 ºC. The reference temperature values obtained for this region by the infrared camera are seen to fluctuate between 30.9 and 31.9 ºC. A higher discrepancy is observed near the heated wall area due to weaker fluorescent signals can be captured in this region. The thermal boundary layers are shown to grow thicker with higher heating input and higher flow rates.

The liquid velocity measurements are performed with the Particle Imaging Velocimetry (PIV) method. The liquid turbulence statistics are obtained for a heated single-phase (2.7 kw/m^2) and two boiling conditions of varying heat flux (16.4 kw/m^2 and 42.8 kw/m^2). The same Reynold’s numbers used in temperature measurements are considered here as well (8121 and 20523). Velocity components, turbulence intensities, and Reynold’s stresses are obtained against the radial distance from the heated wall. The effect of the boiling bubbles on the flow structural behavior is clearly evident, as the liquid velocity values and turbulent intensities appear to increase near the bubble regions. This increase in liquid velocity is a function of the bubble sizes and flow rates. The sliding bubbles tend to grow in size and gain momentum as moving along the heater. The velocity boundary layer thickness is shown to grow with higher heat flux and bigger bubble’s size. This increase in the layer thickness is concomitant with the axial distance.

DEDICATION

To my mother and father, to my family and those who made a difference in my life, I dedicate this work.

ACKNOWLEDGEMENTS

All praises are due to God, whose blessings made this work possible. I would love to thank my mother and father for the love and support they have giving me throughout my learning journey as their belief in me has made me a better person. I would like to thank my entire family and friends who showed me love and encouragement that have brought the best out of me. I would like to give my major advisor, Dr. Hassan, special thanks for the opportunity he provided me with, as well as I am grateful to all my lab mates and collages for the help I received every step in the way. I, also, thank my committee members for their help and positive feedbacks. I would like to express my gratitude to the Saudi Arabia's Ministry of Higher Education for the financial support and coverage throughout my learning run. This work has been a result of great efforts, and I am, genuinely, thankful to everyone who has contributed to make it happen.

CONTRIBUTORS AND FUNDING SOURCES

This work has been sponsored by the Consortium for Advanced Simulations of Light Water Reactors (CASAL).

TABLE OF CONTENTS

Page

LIST OF FIGURES

LIST OF TABLES

Page

CHAPTER I

INTRODUCTION AND OBJECTIVES

1.1 Introduction

Turbulent Subcooled flow boiling is widely useable in research due to its high efficiency in heat and mass transfer mechanisms. However, the complexity of the subcooled boiling process stems from the presence of thermodynamic non-equilibrium between the liquid and vapor phases. The continuous mixing and stirring of liquid generated during the bubble's life cycle give rise to local enhancing mechanisms of heat and momentum transfer. The vapor bubble generation have been found to be an important heat transfer machoism in subcooled boiling. The contribution of the vapor bubble to the overall heat transfer is believed to stem from the evaporation of the liquid micro-layer present between the bubble and heated surface and from the disturbance to the thermal boundary layer due to the motion of the bubble and its associated wake. The heated surface and fluid characteristics on nucleate boiling need to be investigated. Also, the liquid turbulence modifications generated by these mechanisms need to be accurately measured in correlations and equations employed in flow structure modeling.

Several approaches have been developed to predict the heat transfer mechanisms and temperature influence on liquid velocity profiles during the subcooled flow boiling. These approaches include empirical correlations and mechanistic models for the wall heat flux partitioning and liquid velocities. Although our general understanding of the basic heat transport mechanisms has improved with time, the significant mechanism contributing to nucleate boiling heat transfer is still subject to discussion. In general, a fundamental understanding of nucleate boiling heat transfer mechanism is lacking and there still ongoing debate in the literature as to what predominant heat transfer mechanisms.

Several parameters are essential in the study of the wall heat flux partitioning in subcooled boiling systems. Among those parameters are those related to bubble vapor generations, which have been studied experimentally under different boiling conditions. In heat transfer, evaporation is an interesting way to transport heat due the low temperature difference required to transfer a large amount of heat. Extensive studies have been developed over the last few decades to investigate the evaporation processes but the main physical principals are still not fully understood. The lack of a complete understanding limits the usability and usefulness of the predictive models, in subcooled flow boiling, developed to describe this phenomena.

1.2 Objectives

This work primarily aims to advance the existing studies done on parameters with close relevance to vapor bubble generations and sliding mechanisms in turbulent subcooled boiling flow through a vertical rectangular channel. Such studies were shown to be important in wall heat flux partitioning. I set out to primarily study temperature distributions near the liquid interfaces and especially around a growing and sliding vapor bubble as well as the turbulence statistics associated with the bubble wake under various conditions. This study will present a detailed experimental investigation addressing the boiling bubble influences on near wall/liquid region. The bubble dynamics will be captured using high speed cameras with different visual perspectives (Side and back-views), and the temperature will be measured contactlessly by employing a non-intrusive and whole-field technique. This will allow mapping out whole-field temperature distributions with time evolutions of developing and sliding bubbles from birth to detachment. The local thermal response of the liquid due to the presence of these sliding bubbles can also be looked at and measured with an infrared camera, which has a back view of a transparent heated surface. These results are believed to be relevant for the understanding of near-wall liquid-vapor heat transfer which are not available through traditional visualization methods.

In addition, the liquid velocity and turbulence structure are essential components in the heat flux modeling. To this end, the time resolved Particle Imaging Velocimetry (PIV) algorithm along with shadowgraph technique will be used to measure the instantaneous two-dimensional velocity fields and time-averaged axial velocities and to infer the turbulence statistics.

These quantities will be investigated based on experimental data obtained under different conditions of various flow rates (given by Reynold numbers), and the sub-cooling level in forced convection boiling through a narrow rectangular channel. It is believed that this work will support various models have been developed to predict the wall heat flux partitioning that can be adopted in computational fluid dynamics (CFD) studies.

CHAPTER II

TEMPERATURE FIELD MEASUREMENTS USING LASER INDUCED FLUORESCENCE (LIF)

2.1 Introduction

In today’s industry, the temperature measurements is of critical importance especially in systems involving high energy heat transfer such as nuclear reactors. The need for experimental studies to improve and validate the existing models is growing. Such experimental investigations are necessary to describe the temperature distributions in complex flow phenomena with an instantaneous fashion and a high frequency resolution. Recently, most of the temperature measurements have been conducted by the means of intrusive sensors at high frequency but with a low spatial resolution (Estrada-Perez, 2014). Therefore, there is a need for state-of-the art techniques employing non-intrusive whole-field measurement methods. Laser induced fluorescence (LIF) is non-intrusive method that is shown to provide high fidelity full-field temperature measurements. The underlying principal behind the LIF technique is that a laser light is employed to excite a fluorescent dye molecule, which in turn de-excites by emitting a photon of a lower energy and a higher wavelength than the absorbed one (Jones, 2010). The emitted photons in a form of light is called fluorescence, and it is dependent on multiple factors such as incident laser light intensity, the type of dye used, the dye concentration, and temperature. (Estrada-Perez, 2014). Because the absorbed photo (from a laser source) have a wavelength different from the emitted one, optical filters can be used to remove the laser light from the imaging systems, and so only fluorescent light is recorded. Therefore, the process of using laser light to produce fluorescent light is called laser induced fluorescence (LIF). This method have been utilized in different studies to indirectly measure the temperature distributions in fluid containing fluorescent dyes.

2.2 Literature Review

One of the earliest LIF studies involved using a single-dye and one-color LIF technique (coolen et al., 1999; Lavieille et al., 200 ; Lemonie et al., 1999; Ross et al., 2001; Sakakibara et al.; 1997; Seutiens et al., 2001). These studies were reported to suffer significant uncertainties due to high laser light fluctuations. To better improve the temperature measurements using LIF, a ratiometric method was applied in which two colors dye was utilized (Estrada-Perez, 2014). This method is reported to reduce the laser light fluctuations. The radiometric technique can be used with two colors and a single dye (Bruchhausen et al. 2005; Castanet et al., 2003; Lavieille et al., 2001, 2002) or two colors and two dyes (Coppeta and Rogers, 1998; Funatani et al., 2004; Hishida and Sakakibara, 2000; Kim et al., 2003; Natrajan and Chistersen, 2009; Sakakibara and Adrian, 1999, 2004, Estrada-Perez, 2014). As an example of a study done using two colors and one dye, Lavieille et al. (1998) used Rhodamine B in two spectral bands (523 nm > λ > 535 nm and λ > 590) to measure the average temperature of evaporating and collapsing droplets. Their temperature measurements suffered some noise due to weak signals from the first spectral band (Jones, 2010). In another study, Fogg et al. (2010) measured the void fraction and liquid temperature in two phase flow using two colors and two dyes. Their liquid temperature measurements were reported showing insufficient information due to low spatial resolutions and low void fractions.

The dye selection is an important factor in LIF studies. The standard organic dyes such as Rhodamine B (a temperature dependent dye) and Rohamine-110 (a temperature independent dye) are used in various studies (Sakakibara and Adrian, 2004). Estrada-Perez et al., 2001) used Rhodamine B and Fluorescein-27 in which both dyes are temperature dependent. It has been reported that using two temperature sensitive dyes can increase the measurement accuracy (Sutton et al., 2008).

A few studies in the literature have been found utilizing the laser induced fluorescence (LIF) method to investigate the evaporation processes and the temperature distribution at the liquid interfaces and around growing bubble. Jone et al. used plenary laser induced fluoresces-Thermography in water to study the temperature distribution inside the liquid and around a single vapor bubble in nucleate boiling. He was able resolve the thermal boundary layer at the heated surface. However, his study suffers some uncertainties due to some inhomogeneity of illumination with the laser light reflection off the heated surface at the liquid-vapor interface. He observed a dependence of the measured temperature on the local illumination intensity by the laser light. He concludes that LIF method can yield important insights into the nucleate boiling. Like Jone, Vogt has also used of LIF in studying the temperature field around a single bubble in acetone using Rhodamine 19 and DCM as a combination of fluorescence dyes. He also has found the dependence of the measured temperature on the local laser illumination and reflection. His study has also suffered high uncertainty due to a low fluorescence signal obtained from the illumined combination of dyes. He also concluded that LIF method can be useful in obtaining temperature information in nucleate boiling. He also studied the applicability of LIF in temperature measurement in nucleate boiling. Fenner has also investigated the applicability of the LIF method to a stationary evaporating liquid meniscus. He suggested that the temperature measurement at the wall and near liquid-vapor interface is only possible at low evaporation rates.

2.3 Background

The laser-induced fluorescence technique is based on the temperature dependence of a fluorescence signal of a dissolved fluorescent dye excited by laser light. The fluorescence intensity of the fluorescent dye is defined, according to Sakakibara, Hishida and Maeda, as the following,

$$I = I_o \varepsilon A \Phi L C \tag{2.1}$$

Where I_o is the laser intensity; ε is the molar absorption coefficient at a given wave length of laser light, A is the fraction of light collected, is L the sampling length, C is the concertation of fluorescent dye, and Φ is the temperature dependent quantum yield. The assumption embedded in this relationship is that the fluorescence intensity is linear to both concertation and laser intensity. According to Fenner, this assumption is only valid for low dye concentrations and laser intensities. The linearity assumption can also depend on the fluorescent dye and solvent type used. Rhodamine B is a type of dye that has been used widely in the literature, and it is shown to have a considerable temperature coefficient of about -2%/K in water at low concertation (below 1 mg/L). At sufficiently high concertation, a reduction in the fluorescence intensity known as self-quenching is expected to happen. Quenching in Rhodamine B is reported to happen at concentrations higher than 50 mg/L. Typically, 1 mg/L or less of Rhodamine B is the concertation value used in laser-induced fluorescence thermography studies.

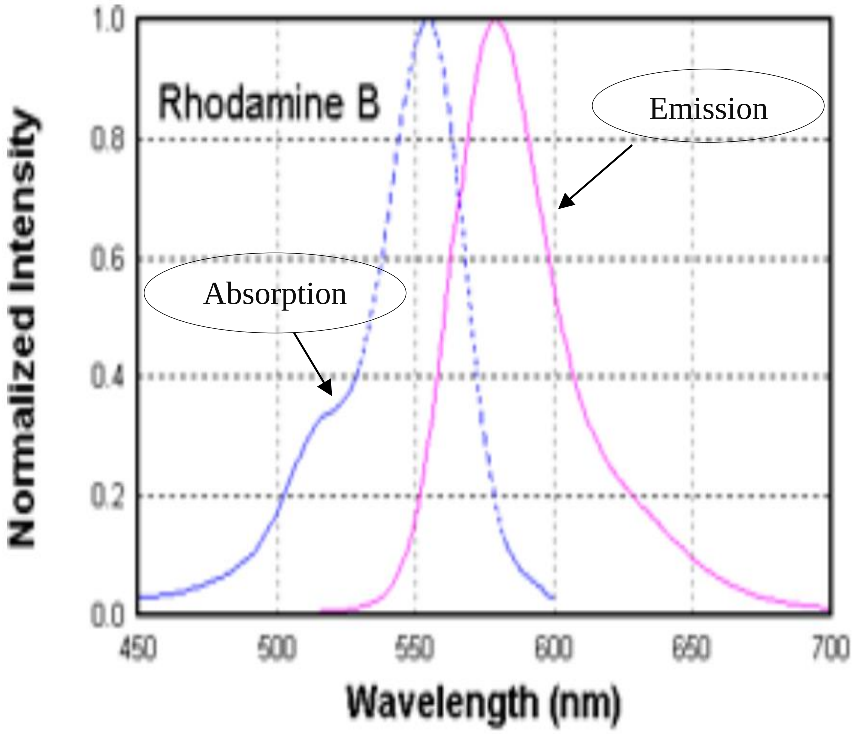

Figure 2.1: Emission and absorption spectra of Rhodamine B.[1]

2.4 Materials and Methods

2.4.1 An Overview on the Experimental Facility

The experimental facility consists of a Coriolis flow-meter, a centrifugal pump, a heat exchanger, a condenser, a test section and flow control valves. Figure 2.2 shows a schematic of the experimental facility. As shown in Figure 2.3 (a photograph of the

---

[1] Reprinted from: Terpetschnig, E., Yevgen, P., Eichorst, J. (2015). Polarization Standards. ISS

experimental facility), most of test loop components are made of glass. The reason for the glass choice is to reduce the chemical interactions between the working fluid and the loop materials and to enhance the working temperature limits (Estrada-Perez et al., 2017). The test section consists of separate glass windows attached with a ceramic epoxy forming a rectangle channel with an inner flow area of 23.8 x 33.3 mm^2 and a length of 600 mm. A similar channel is located below the test section to provide a fully developing flow with length of 600 mm. The test section back-side, facing the infrared camera (IR), is cut to leave a rectangular opening of about 15 x 235 mm^2. A heated surface (made of a silicon wafer that is transparent to the infrared radiation) is attached over this opening. The open window allows direct optical access from the infrared camera to the heater surface. The infrared camera model (IR) used in this study is FLIR SC8000 (shown in Figure 2.6 (right)). Silver electrodes are attached along the sides of the eternal face of the heated surface. These electrodes are responsible for delivering power from a power supply control to the heated surface, and they are identified as anode and cathode. Each electrode has a length of about 200 mm. The power to the heater is supplied and controlled by a DC power supply through two long copper sheets to provide a uniform current distribution from each electrode. The active heating area is fully exposed to the infrared camera view. The working fluid temperature is adjusted by a chilling unit and through a heat exchanger that connected to the test loop. The 3M NOVEC 7000 (shown in Figure 2.6 (left)) is used as the working fluid in this study

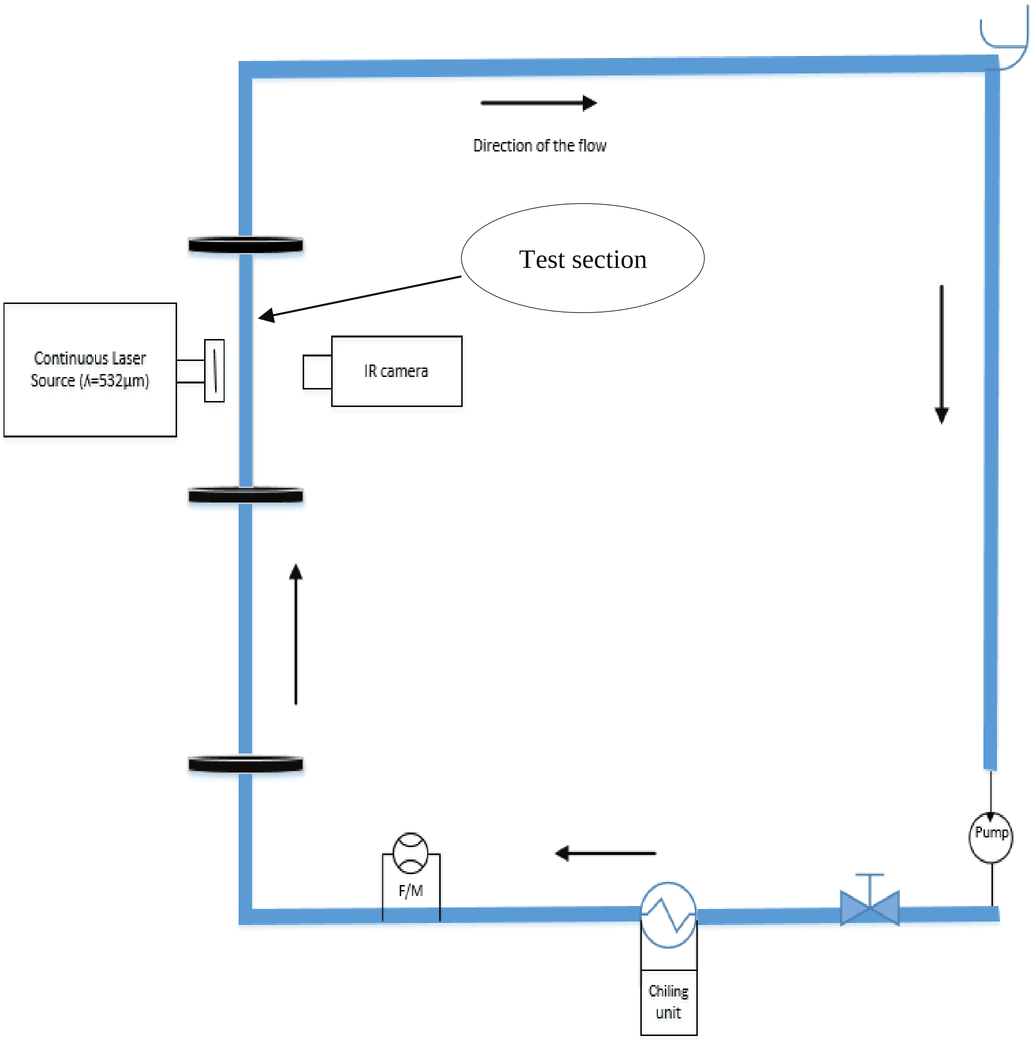

Figure 2.2: A schematic of the experimental facility.

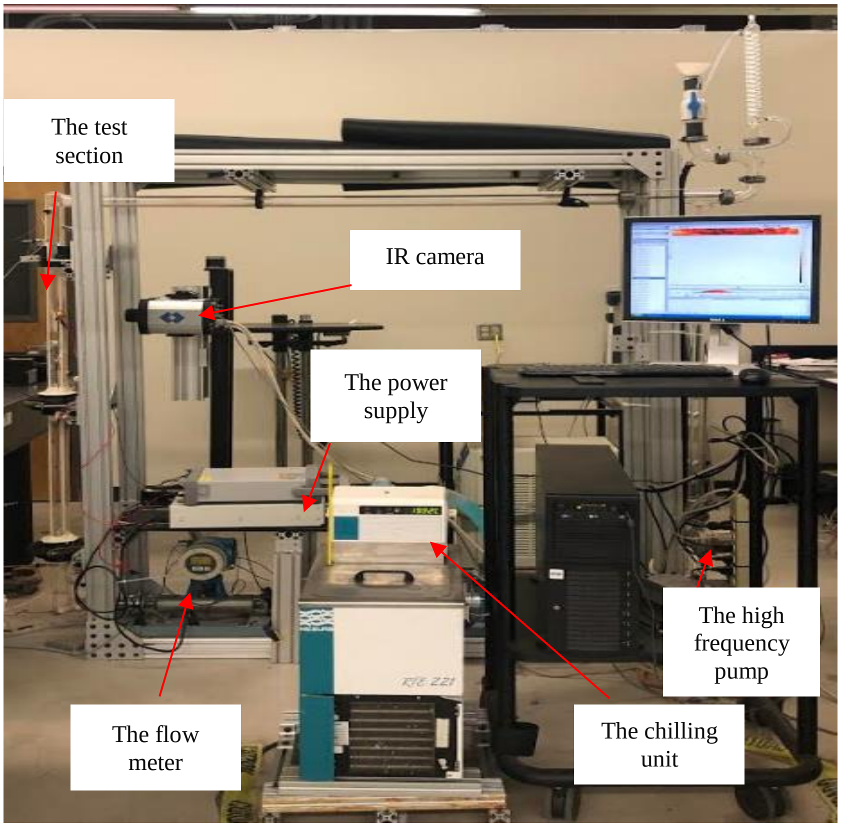

Figure 2.3: A photograph of the experimental facility.

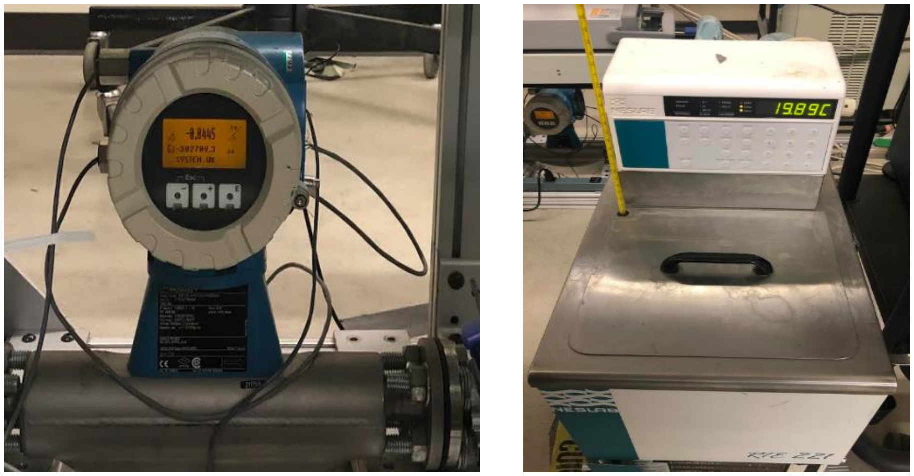

Figure 2.4: The flow-meter for flow monitoring (left) and the chilling unit for liquid temperature control (right).

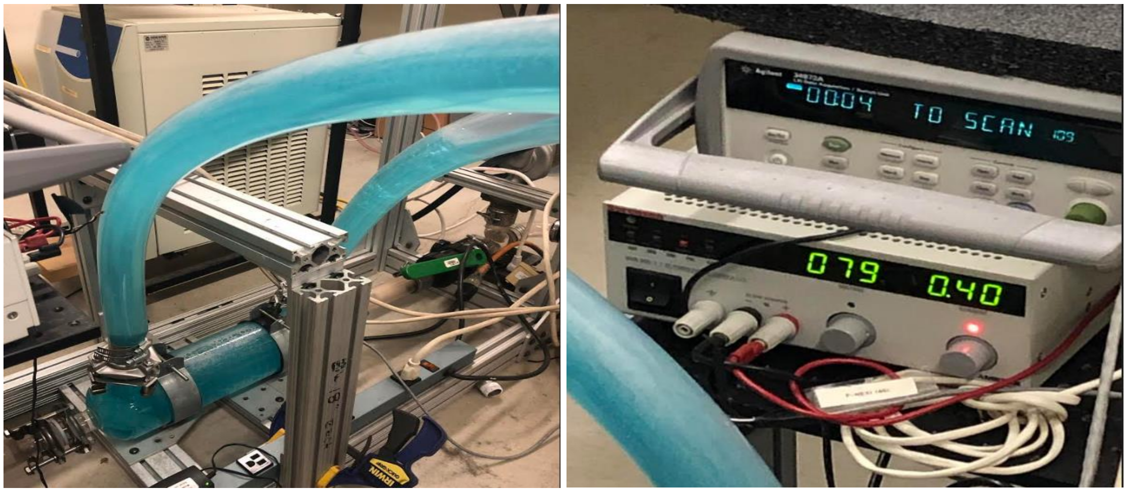

Figure 2.5: The connected heat exchanger (left) and power supply control (right).

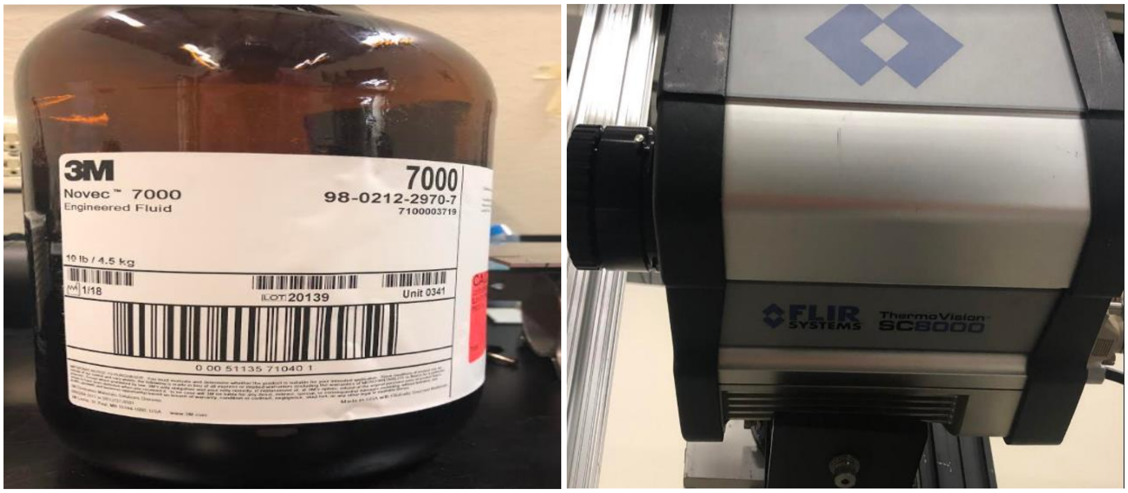

Figure 2.6: The working fluid (3M NOVEC 7000) (left) and the infrared camera (IR) (right).

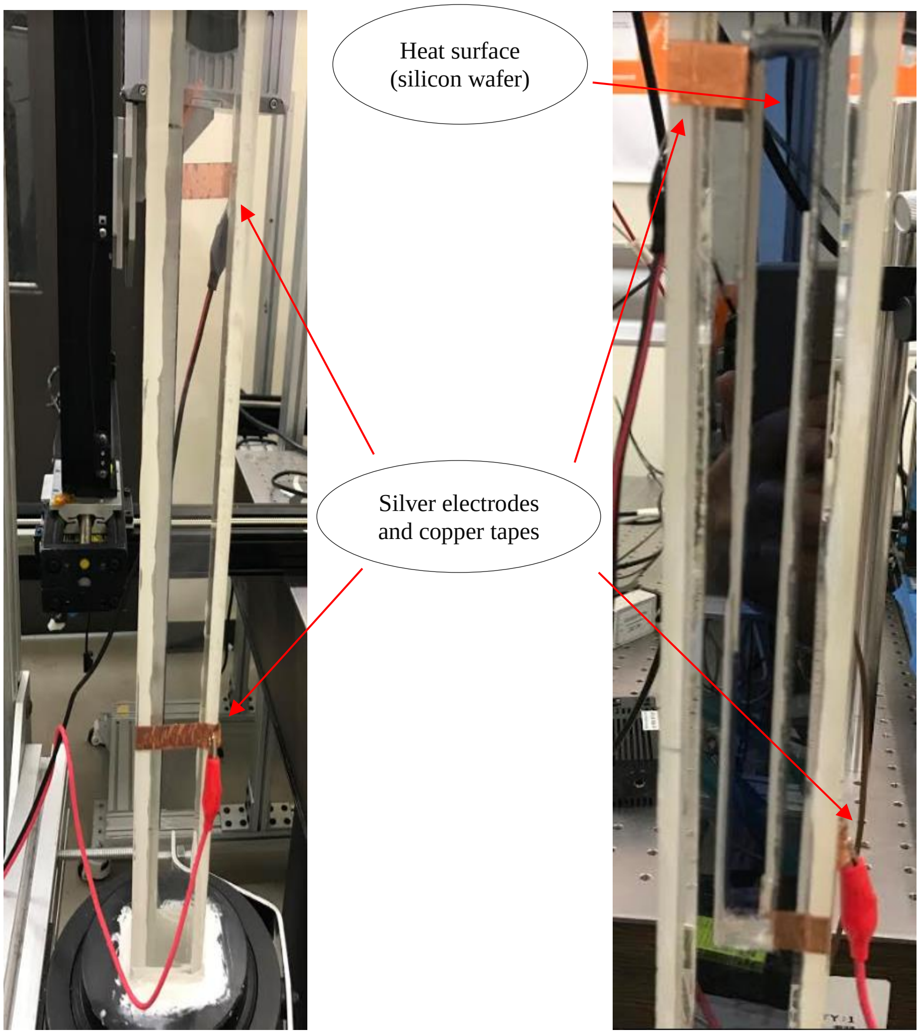

Figure 2.7: Side-view at the test section (left) and back-view at the test section (right).

2.4.2 Laser Induced Fluorescence (LIF) Experimental Facility

Figure 2.8 below shows a schematic of the LIF experimental facility. Rhodamine B, the fluorescent dye (shown in Figure 2.12), is first diluted in ethanol (as a solvent) and dissolved in the working fluid used in this experiment (3M 7000 NOVEC refrigerant). The total dye concertation dissolved in the working fluid is 0.25mg/L. The region of interest in the flow field is illuminated by a 10 W continuous laser source of 532 nm wave length (Figure 2.10 (right)). A laser optical lenses and a collimator (provided in Figure 2.10 (left)) are used to generate a thin vertical light sheet focused on the region of interest where the camera imaging takes place. The imaging system consists of a high-speed camera (Phantom V711) that is arranged at a 90º degree angle to the heater. The positioning of the camera is made in such a way to reduce optical distortion due to considerable variations in refractive index near liquid-vapor interface. The camera visualizes the desired field of view through a bandpass filter, which has 586 nm ± 20 nm (FWHM) range with 93% ± 5% transmission rate, so that the camera is primarily sensitive to the fluorescence intensity produced by Rhodamine B only. It's worth mentioning that Rhodamine B has a peak emission intensity with the wavelength of about 585 nm as shown in Figure 2.1. The high speed camera is a phantom V711 which employs 944 pixel by 200 pixel (1.9E5 pixel sensor). The viewing area at the field of measurement is approximately 120 mm x 22.5 mm. The conversion factor from pixel to mm is 5.8 pixel per mm. The camera is set to operate at 2000 frames/sec with an exposure time of 490 µm. This exposure time is selected to allow sufficient light to reach the camera sensor. The laser source and the camera are fixed independent to translation stages to allow positioning relative to the test section. The white LED backlight is placed at the back end of the test section facing the camera. The backlight is used to improve the low power noise of the camera sensor by enhancing light intensity as a DC bias, which is shown to enhance the raw image quality significantly. Figure 2.9 below displays a photograph of the LIF experimental facility described above.

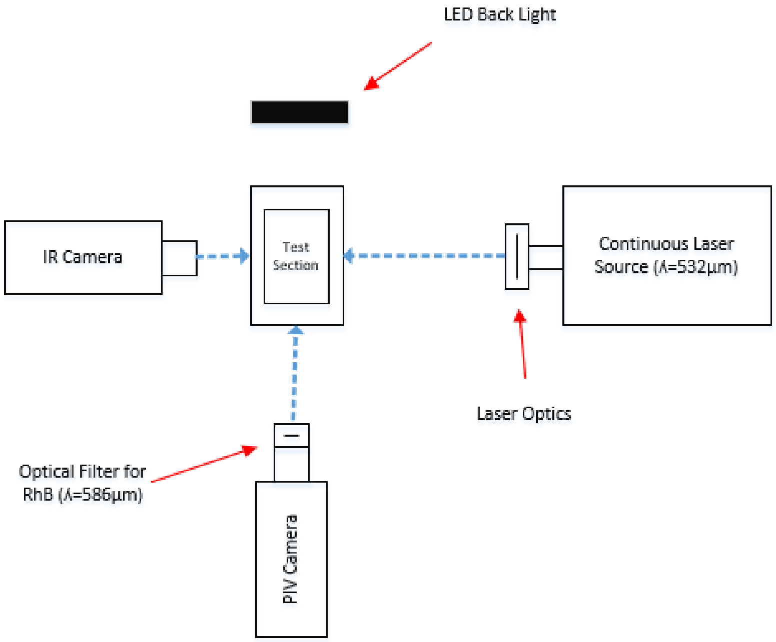

Figure 2.8: A schematic of LIF experimental facility setup.

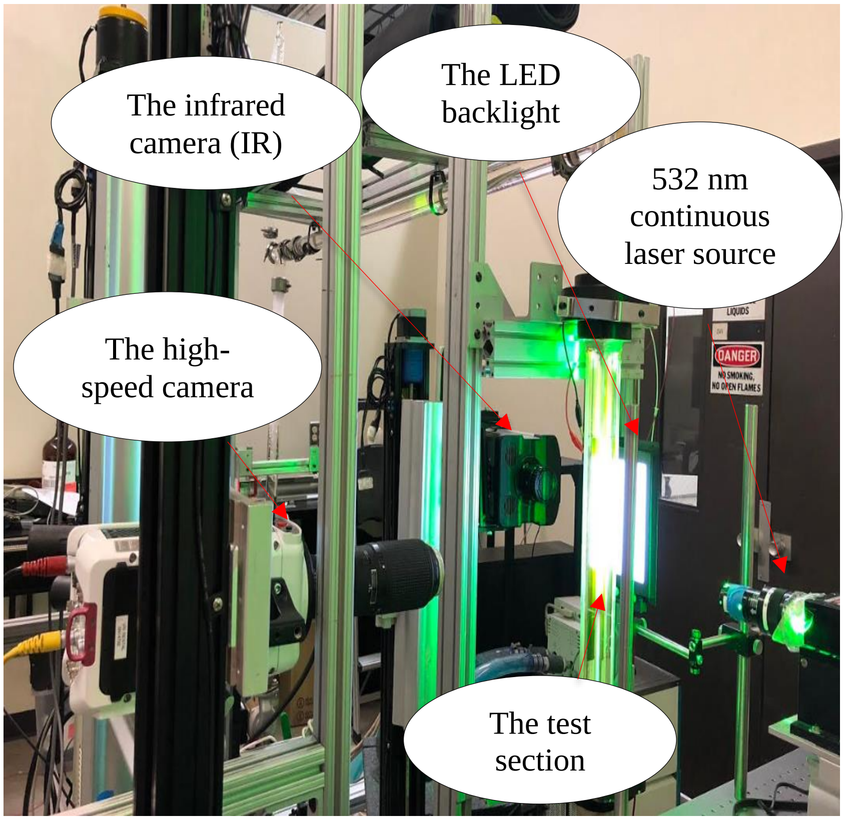

Figure 2.9: A photograph of LIF experimental facility setup.

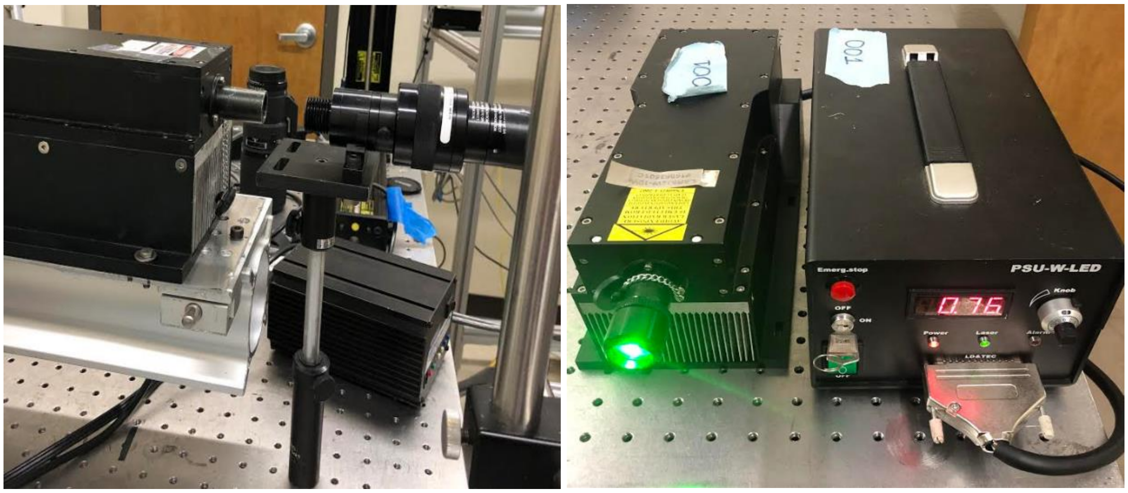

Figure 2.10: The Laser optics and the collimator (left) and the continuous laser source of 10 W (λ =532 nm) (right).

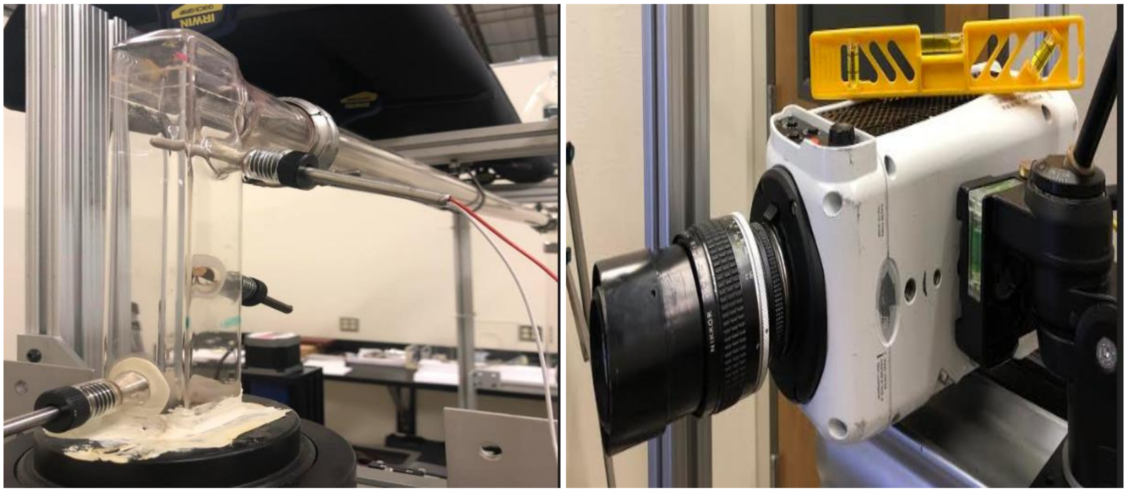

Figure 2.11: T-type thermocouples at the outlet (left) and the high speed camera Phantom V711 (left).

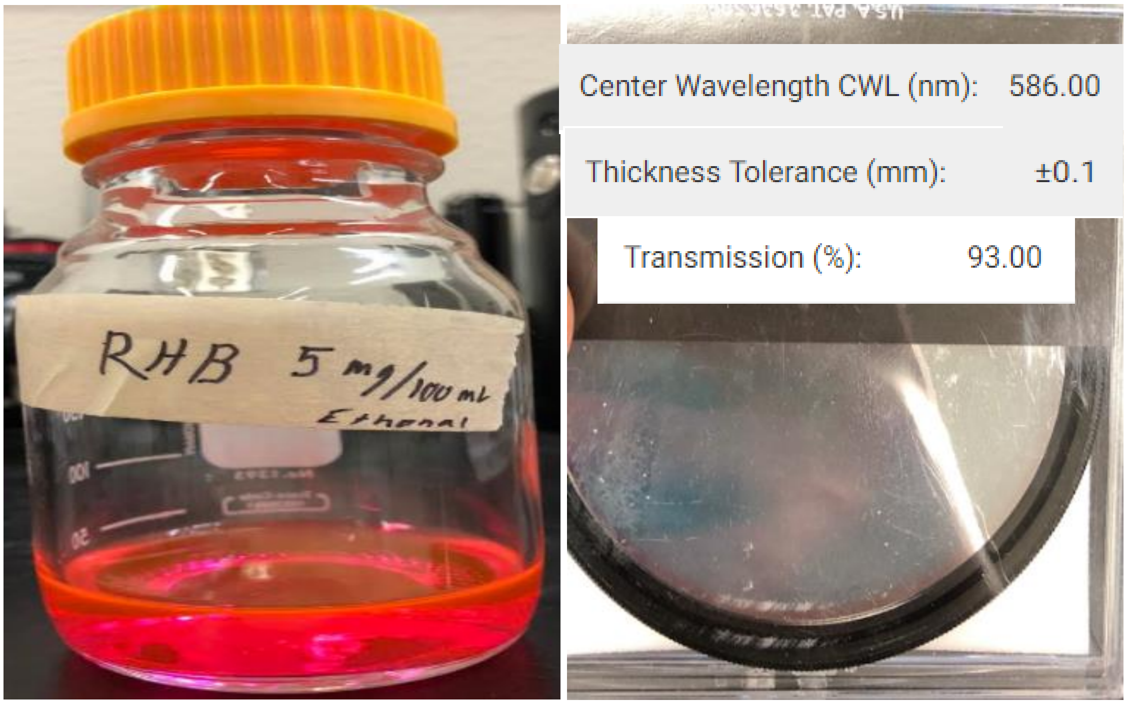

Figure 2.12: Rhodamine B fluorescent dye (left) and the bandpass filter (λ=586 nm) (right).

Table 2.1: Experimental Instrumentations.

Instrument	Parameter	Model	Range	Tolerance
Chilling Unit	Water bath temperature control	RTE-221	25 ºC to 150 ºC	± 0.01 ºC
Thermocouples	Liquid temperature measurement	T-type	-270 to 370 ºC	± 0.75%
Flow meter	Liquid flow rate reading	Promass 83F08	0 to 18000 kg/h	±0.10%
Liquid circulating pump	Run liquid within the loop	ASTRO 290ss	0 to 64 USgpm	N/A
Sorensen	Power supply to the heater	XHR 600-1.7	0 to 600 V 0 to 1.7 A	+0.35% +0.1%
High speed camera	High speed image recording	Phantom V711	1280 X 800 pixel (1,400,000 fps)	20 ns time resolution

2.4.3 LIF Calibration Procedure

In order to perform a successful LIF experiment, information about ε and Φ in equation (1) is not required. Instead, calibrations experiments can be performed to determine the relationship between the fluorescence intensity and the temperature. For the purpose of this study the following functional form used is,

$$I = I_o W(T) \tag{2.2}$$

Where $W(T)$ is a functional relationship that accounts for ε, Φ and C, and it can be determined by the calibration experiment. In general, the calibration experiments are performed by measuring the fluorescence intensity by the camera while maintaining the fluid at series of uniform temperatures (Jones, 2010).

Prior to measurements taking, the loop is normally run to achieve the temperature equilibrium at the desired level. In this experiment, the calibration procedure is performed by increasing the temperature from 10ºC to 30ºC in steps of 5.0ºC, resulting in five different calibration temperature points, namely, 10, 15, 20, 25, 30 ºC. As a temperature reference for the calibration, the two thermocouples at the inlet and the outlet of the test section are used for temperature readings at each calibration point. At each temperature point, the measurement field is illuminated by the continuous laser power for the dye to fluoresce and the fluorescence intensity is measured. And then, 12000 fluorescent images (6 sec recording time) are captured by the high-speed camera. The recoded images are segmented into 8 x 4 pixels averaging intensity region, in which the intensity is correlated to the corresponding temperature, and a calibration curve is obtained for each region. The obtained calibration curves are then applied to each pixel in the boiling and heated single-phase experimental images for temperature field computations.

2.4.4 LIF Heated Single-Phase and Boiling Experimental Procedure

The experimental approach to the study of the temperature distribution in sub-cooled boiling under different conditions is conducted by varying the controlling parameters, namely, the liquid flow rate and the heat flux level at a certain inlet temperature of the working fluid (20 ºC). The heat flux provided at the heated surface is set to a certain level to provide boiling at specific flow rates. Two Extra heated single-phase conditions are added to characterize the temperature distributions in single-phase flows. Various experimental conditions (three different heat fluxes and two different liquid flow rates) are performed resulting in six cases, given by the Reynold's number (Re), the liquid inlet temperature, and the heat flux as shown in table 2.2.

With experimental setup remains similar to the calibrations, the boiling conditions and heated single-phase are performed. Because the solubility of air on the refrigerant is about 30% by volume, a degassing procedure was required for each round. The degassing process is needed to remove the non-condensable gases diluted in the liquid. The flow inside loop is degassed by circulating the liquid through the flow loop while boiling the liquid. This procedure continues until all air bubbles within the flow are removed. The degassing process takes 2 to 3 hours, and it is performed by the controlling parameters that are being set. The considered controlling parameters are the flow rate, the inlet liquid temperature. A T-type thermocouples are used to monitor the inlet and outlet temperature. The flow rate is first adjusted using the pump frequency drive and flow control valves, and it is monitored with a flowmeter. Once the flow rate is set to a desired value, the liquid temperature is then adjusted using the chilling unit and the heat exchanger. When the system stabilizes to a steady state condition, the power supply to the heater (the silicon wafer) is adjusted to supply the power needed to induce boiling. The two heated single-phase conditions are performed with a heat flux just below the boiling threshold. For the boiling conditions, the power to heater is set to the minimum required to induce nucleation at a certain flow rate and a liquid temperature. Once the nucleation sites of interest are activated and the heater stabilizes in temperature, the laser light is turned on, and the laser power is adjusted to the desired value. Once the laser power stabilizes, the fluorescence images are taken by the high speed camera with 2000 fbs and an exposure time of 490 µs. The infrared images are captured by the infrared camera (IR), which reads at a frame rate of 1000 fbs.

Table 2.2 Experimental Conditions for LIF.

Set	T [ºC]	Heat Flux [kw/m2]	Re[-]
1	20.83	3.9 (heated single phase)	8121 (low Re)
2	20.65	3.9 (heated single phase)	20523 (high Re)
3	20.83	30.9 (low heat flux)	8121 (low Re)
4	20.65	30.9 (low heat flux)	20523 (high Re)
5	20.83	36.6 (high heat flux)	8121 (low Re)
6	20.65	36.6 (high heat flux)	20523 (high Re)

For the purpose of this experiment, the side view configuration is designed to provide detailed liquid temperature information near the bubble's nucleation sites and the heated wall and to obtain insights on the thermal boundary layer development along their sliding distance. The LED back light is arranged to directly illuminate the high speed camera's view and obtain clear bubble's dynamic images. The viewing area achieved by the camera is 120 mm x 22.5 mm^2.

An example of the fluorescent images acquired experimentally for the high boiling condition with high Re is provided below in Figure 2.13. This image is obtained with the laser light illumination, which is used to fluoresce the dye. As mentioned earlier in this section, this image is filtered with a bandpass filter, which preferentially allows photons with a wave length of 586 nm to be captured. Such filter helps reducing the laser reflections off the bubble interfaces and the heated surface as well as reducing any background noise. This allows to achieve more accurate liquid temperature measurements. The fluorescent images, as shown in Figure 2.13, capture the bubbles behavior along the entire sliding distance from inception (at the nucleation sites) to detachment toward the mid-section of the image. This allows to obtain a complete look at the bubbles' life span once sliding for a whole-field temperature measurements and a full thermal boundary layer mapping.

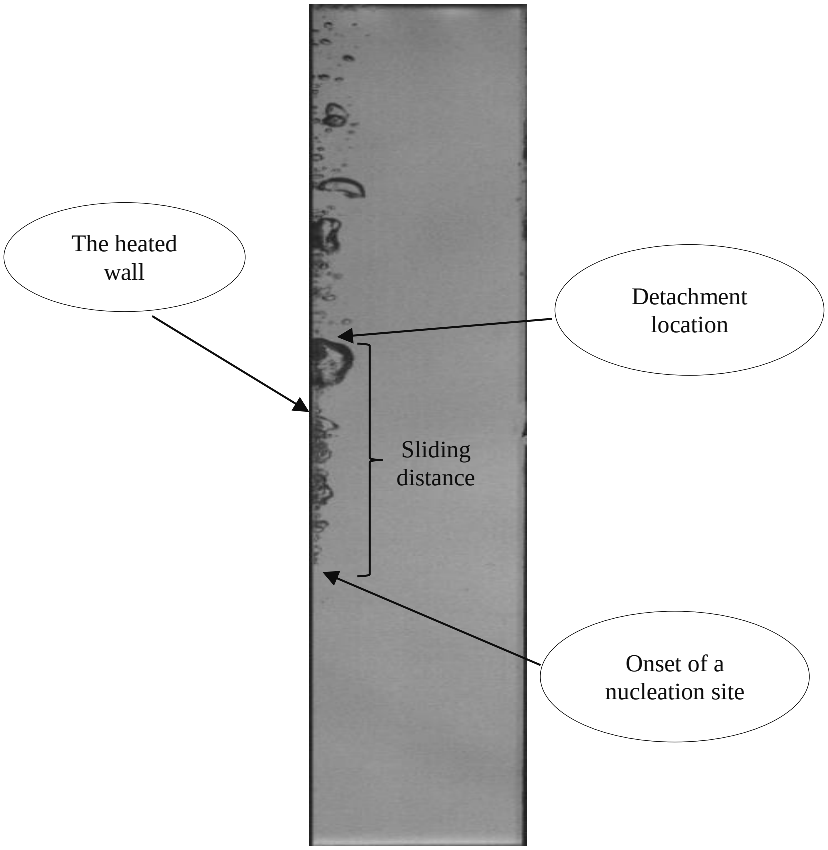

Figure 2.13: A fluorescent image for high boiling (36.6 kw/m^2) with high Re (20523) condition.

2.5 Experimental Results and Discussion

2.5.1 Experimental Calibration

The LIF temperature measurements allow experimental investigations on the influence of nucleate boiling on temperature fields near wall/liquid interface and around a growing bubble. The whole-field method of LIF is shown to be useful to measure the developing thermal boundary layer for nucleate boiling in contactless fashion. A high resolution imaging capability is required to resolve the temperature variations at the interfaces.

The calibration experiment is needed to establish the relationship between the fluorescence intensity and the temperature. Ideally, this relationship follows the mathematical formulation given in equation 2.1. However, experimentally, the intensity fields are measured with a high-speed camera employing a CMOS sensor. And so, the fluorescent intensity is determined by the camera’s sensor pixel values. Nonetheless, due to non-idealities in the camera’s sensor, the pixel value is not necessarily directly proportional to the fluorescent light incident on the sensor, and so in-situ calibration is preformed to determine the fluorescent intensity behavior with the temperature in this setup. The experimental intensity images, obtained for calibrations, are divided into intensity averaging regions of 8 x 4 pixels, and calibration curves are computed for every region. The averaged calibration curves are then applied to each pixel in the boiling images for temperature field calculations.

Figure 2.14 below shows the calibration curve obtained with five temperature points in the range of 10°C to 30°C. This temperature range represents the experimental conditions considered in this study. The fluorescence emission intensity, obtained at each temperature point, is normalized by a reference temperature value. This reference temperature is chosen to be 20 ºC. The normalized intensity is shown to be decreasing with the temperature; however, the curve is not behaving linearly. The non-linear relationship of the temperature and emission intensity can be resulting from different contributing factors. Among those factors are the degree of sensitivity of the camera sensor, the non-uniform illuminations of the laser sheet, and photon self-quenching effect. The non-uniformity in the laser illumination can be a subject to uncertainties in laser power and dye concentrations.

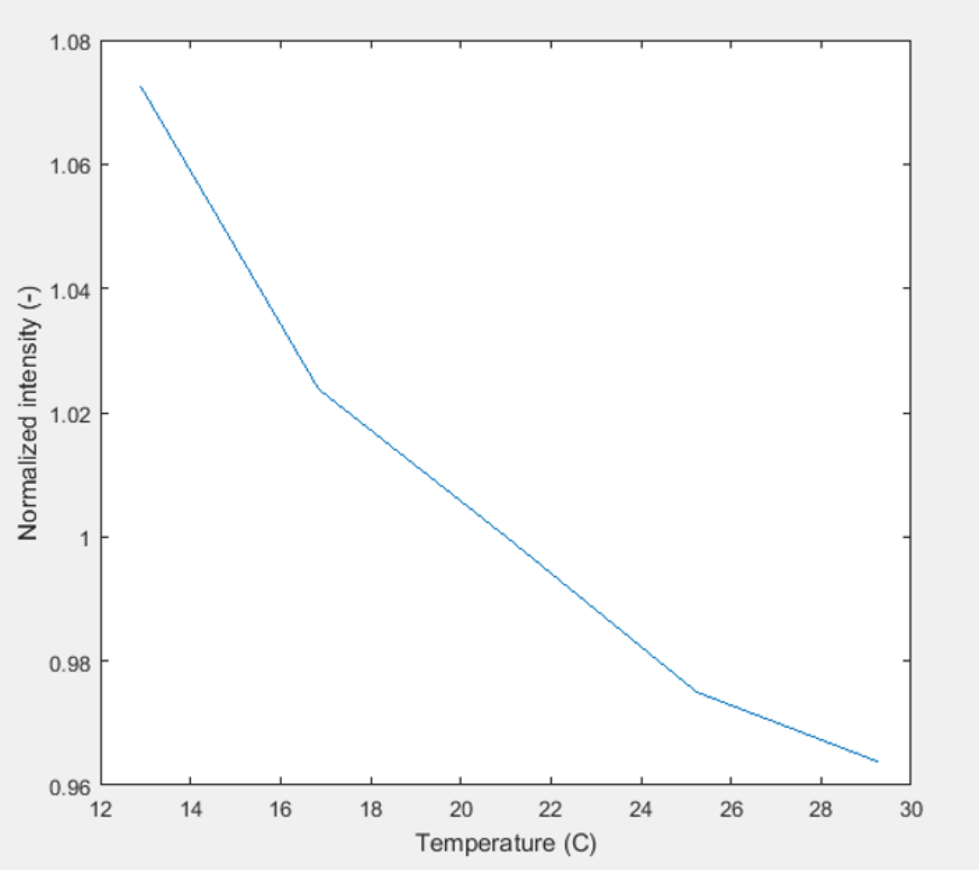

Figure 2.14: The experimental calibration curve.

The temperature points shown in the plot represent the equilibrium temperature of the working fluid, which are obtained to be slightly higher than water-chiller temperature. A noteworthy feature is that the fluorescent signal becomes weaker with increasing temperature, and so the difference in intensities between the last two points in the curve (at 25 ºC and 30 ºC) is fairly small.

2.5.2 Temperature Field Measurements

2.5.2.1 Single-Phase Conditions

The heated single-phase fluorescent images are processed and averaged to reveal the average liquid temperature fields. These average temperature fields provide information about the temperature distribution across the radial distance of the test channel and along the bubbles' sliding distance in the axial direction. In order to gain a visual insights into the temperature distributions at the regions of interest, horizontal line probes are marked at axial locations along the heated wall. Those locations represent the boiling spots. The temperature values along the lines are extracted and plotted against the radial distance, which demonstrates the temperature distribution in the radial direction. Those distributions are obtained at different axial locations in regions where boiling takes place in order to fully visualize the development of the thermal boundary layer and gain an understanding of temperature variations near the heated surface. Heated single-phases are preformed first to characterize the flow development and the temperature distributions in the near-wall regions. Figure 2.15 below shows the average temperature fields for the heated single-phases with two different flow rates, low Re (left) and high Re (left), obtained at an inlet temperature of approx. 20.4 ºC. These two conditions are obtained with the heat flux level of 3.9 kw/m^2, just under the boiling threshold. The color bar indicates the temperature value given in ºC. The heated wall is shown in left side of the test section. The measurement section dimensions are provided in millimeters (mm) with about 60 mm in length axially and 22.5 mm in width radially. The temperature measurements are taken just near the heated wall and across the entire radial distance of the test channel at three different axial locations, namely, 10, 15, 20mm, from bottom end the channel. Those locations are marked in Figure 2.15. The temperature values at those locations are plotted in Figure 2.16, low Re (left) and high Re (right). In the low Re condition, the plot shows that the temperature values, at the axial distance of 10 mm, fluctuate between 18 ºC and 19 ºC (far from the heated wall), but they increase sharply at around 0.15 mm radially to reach about 26.9 ºC as it approaches the heated wall. The temperature profile at the higher axial distance (15mm) is seen to fluctuate at slightly higher temperatures (between 19 and 19.5 ºC). The profile also increases largely at around the same radial distance to reach about 27 ºC. Similarly, at the highest axial location, the bulk temperature values far from the wall are shown to vary around 20 ºC. The temperature start to grow sharply at 0.13 mm to reach 29.2 ºC just near the heated wall. This discrepancy among the temperature values, especially near the wall, can be attributed to different factors. The first factor is a possible non-uniformity in the heat distribution at the surface of the heater in which some spots appear hotter than others across the surface. This can result from some noise and impurities on the heater's material. The other reason is the laser reflection on the heated surface. This refection can make some regions appear brighter than others, which may lead to measurement errors. It’s worth mentioning that, the band-pass filter applied to the camera helps reduce the effect of laser lights at the camera sensor.

The high Re condition is also provided in Figure 2.16. A similar trend can be observed here as well. The temperature distributions, far from the wall, appear to fluctuate between 18 and 20 ºC. A sharp increase in temperature for all axial profiles is also apparent at around 0.15 mm radially. However, the discrepancy in temperature values just near the wall region is shown to be less pronounced (than seen in the previous condition) as the temperature values appear to collapse together between 27 and 28 ºC. This is believed to be due to a higher mixing in liquid induced by the higher flow rate, which resulted in more homogenous temperature distribution. A noticeable feature in the average temperature field for this condition is that the temperature distributions near the bottom of the channel appear slightly higher. It’s worth noting that at higher Re, the flow pump runs at higher frequencies, and as a result, it generates some heat. This may lead to additional heating input from the pump and to the system, which can raise the liquid temperature value at the inlet. However, this heating input is believed to be negligible as no noticeable changes in inlet temperature are registered by the thermocouples during the experiment.

In both conditions, the thermal boundary layers are obtained to be within 0.15 mm in radial distance. And so, thermal boundary layer thickness in both conditions appear to be comparable with no noticeable difference. It’s worth mentioning that the thermal diffusivity ($\frac{k}{\rho\, c_p}$) of the working fluid (3M NOVEC 7000) is 0.04E-7 m^2 /s. Where k is the thermal conductivity, ρ is the density of fluid, and c_p is specific heat constant.

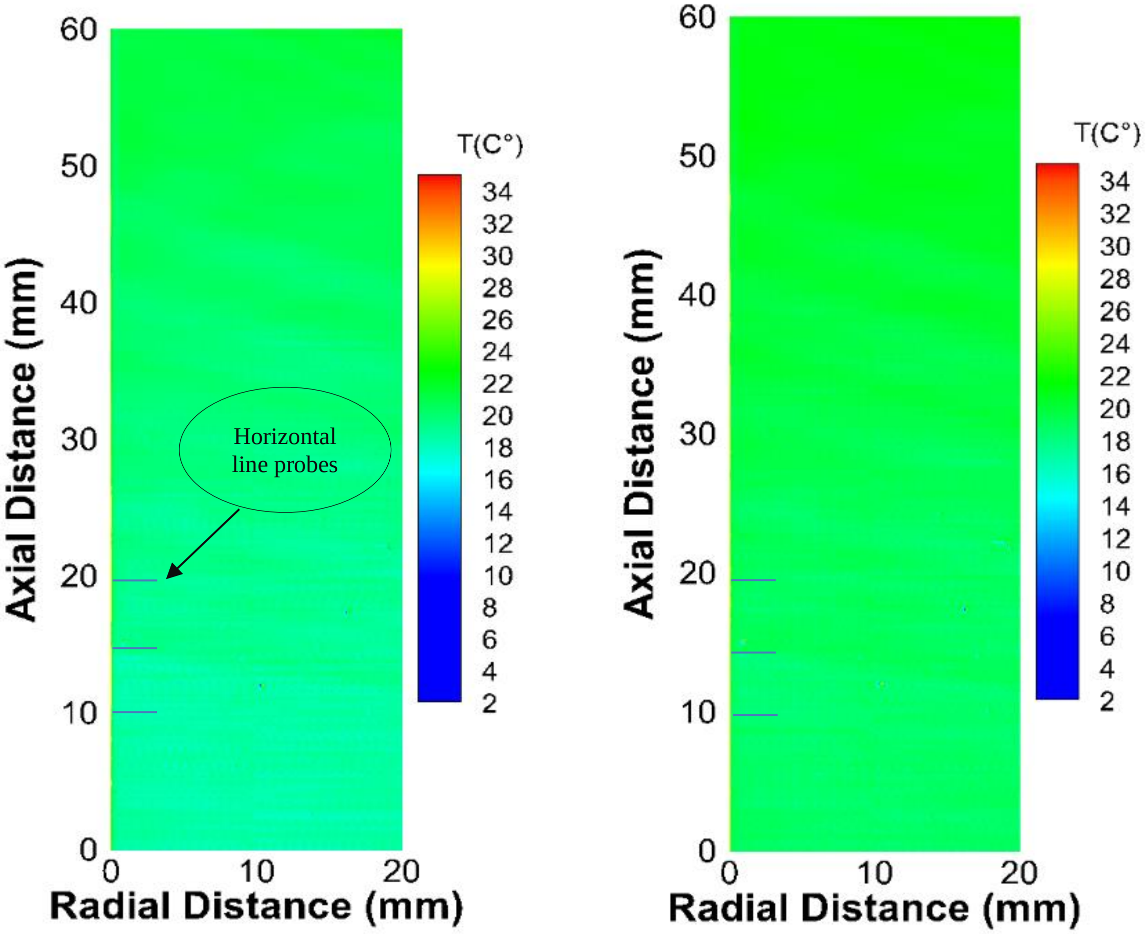

Figure 2.15: Temperature fields for heated single-phase (3.9 kw/m^2) conditions with low Re (left) and high Re (right).

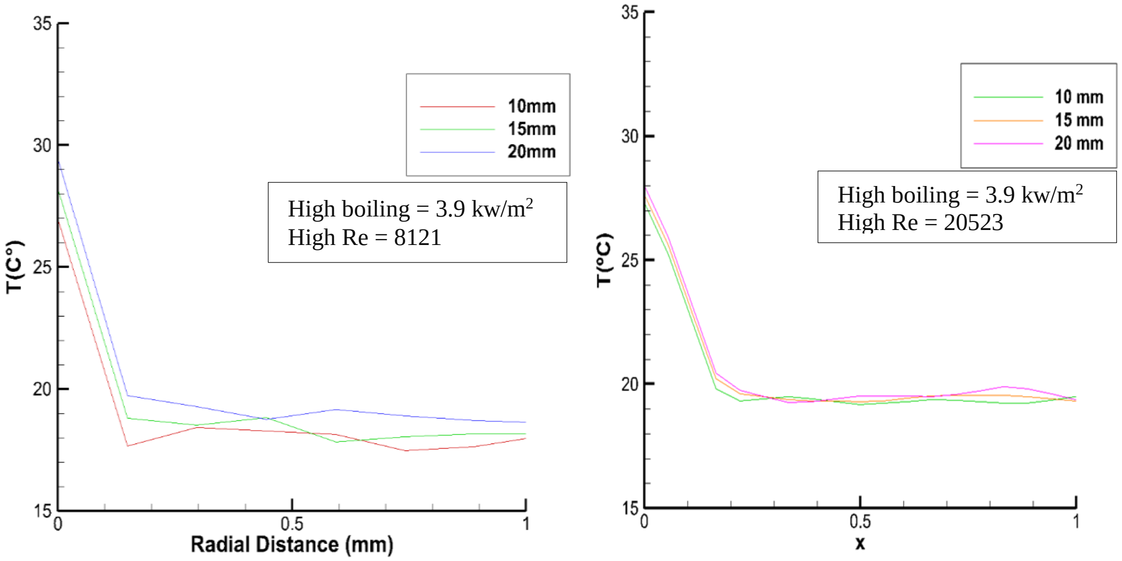

Figure 2.16: Temperature distributions for the heated single-phase conditions with low Re (left) and high Re (right).

2.5.2.2 Boling Conditions

2.5.2.2.1 Instantaneous Bubble's Behavior

In this section the boiling conditions are addressed. As mentioned earlier, four boiling conditions are performed with varying input heat flux and flow rates. The first condition to discuss is the one with high heat flux (36.6 kw/m^2) and high Re (20523). An instantaneous raw and a processed LIF fluorescence image of this case is provided in Figure 2.17. In this condition, the working fluid's inlet temperature is maintained at around 22.5°C as recorded by the thermocouples. The raw image provided is for a multi-nucleation site case, in which bubbles slide across the heated surface after they are born and merge together before detachment. The fluorescence intensity is shown to be non-uniform toward the mid-section and right end of the image due to some possible non-uniformity in excitation light intensity from the laser sheet. Laser reflections near the bubble interfaces may have contributed to the apparent non-uniformity as well.

However, the optical filter applied to the high speed camera is used to minimize such an effect. The bubble shadows and some possible optical distortions are also apparent near the bubble interfaces, which are believed to result in some optical effects.

The processed image shows the temperature field of the liquid surrounding the bubbles and at the bulk liquid region. The bulk liquid is shown to be in the range of 20°C to 21°C, which is expected based on the thermocouples data at the inlet and outlet temperatures. The average value obtained by the thermocouples is 20.66 ºC. Toward the end of the test section, a noisy spots are observed, which presumably signifies the non-uniformity in illuminations as shown in the raw image. As demonstrated in the processed images, the bubbles domain is made removed from the field by utilizing a threshold under which only liquid temperature information is present. The bubbles are shown to nucleate at around 60 mm and slide along the heater up until around 100 mm in which they start deforming and detaching at around 120 mm. After detachment, it is shown that they start to deform even further and collapse. At the bubble interface, a very thin thermal boundary can be observed where the temperature is seen to be increasing toward the bubble domain. A sharp temperature rise (close to the saturation temperature of 34°C) appears to happen in a very thin region near the bubble interfaces and near the heated surface, which is expected. A very thin hot region can also be seen under the growing bubble. This hot spot may highlight the high liquid temperature value at the heated surface just underneath the sliding bubble, which is shown to be between 30 and 32 ºC. This temperature range is just below the saturation level. It is also apparent that a bubble shadow is present in this spot. This bubble shadow can also be processed as a hot region due to the low intensity at the shadow spot, which can lead to some measurements errors. It is worth mentioning that the temperature near the heater may not be accurate in this LIF measurement as the silicon surface of the heater is partially obscured due to out-of-focus heater edge and bubbles self-mirroring. However, temperature information near and at the bubble regions can be inferred from the infrared camera (IR). And so, an IR image for the same condition is recorded and provided in Figure 2.18. The sliding bubble shown in LIF image is marked on the IR one and its temperature information is mapped out. Figure 2.18 displays the liquid temperature near the heater and just underneath the bubble. The temperature plot in this figure demonstrates the variations in temperature at the marked region. It is shown that the temperature fluctuates between 30.7°C to 31.8°C, which is an expected range for temperature values near a sliding bubble. The same range of values is also observed in the processed fluorescent image.

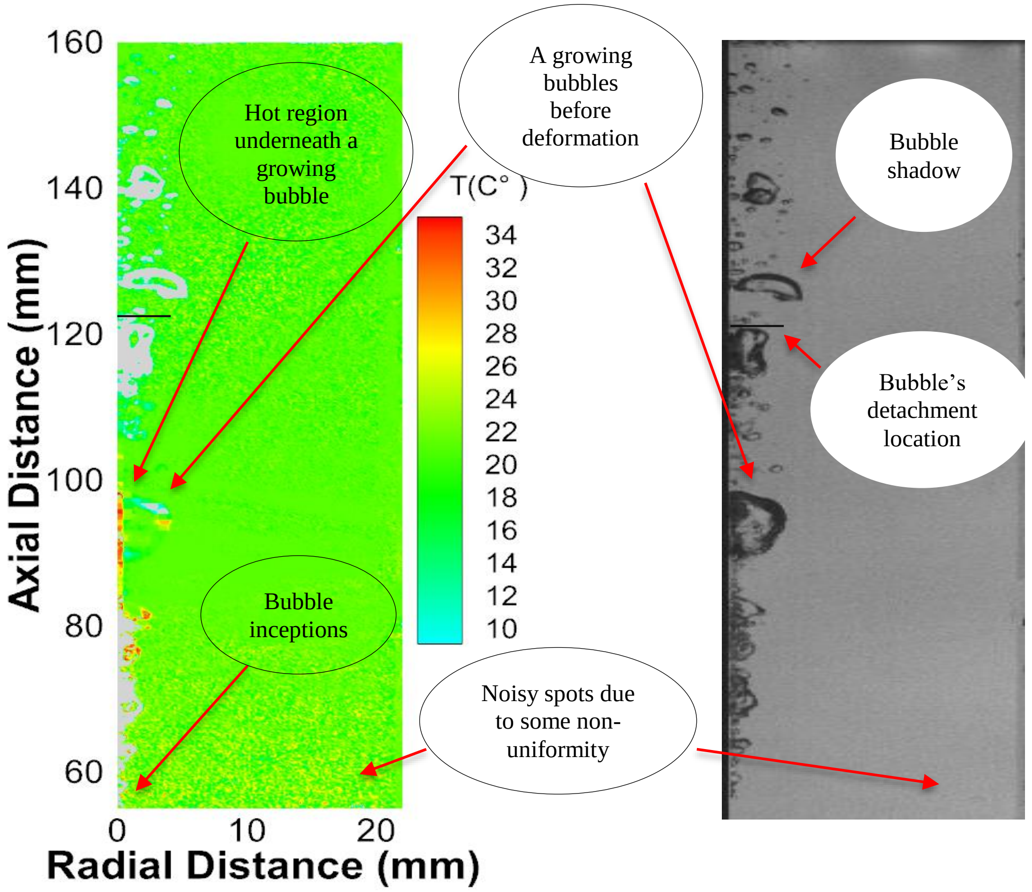

Figure 2.17: Instantaneous LIF image (left) processed image and (right) the instantaneous raw image for high boiling (36.6 kw/m^2) and high Re (20523).

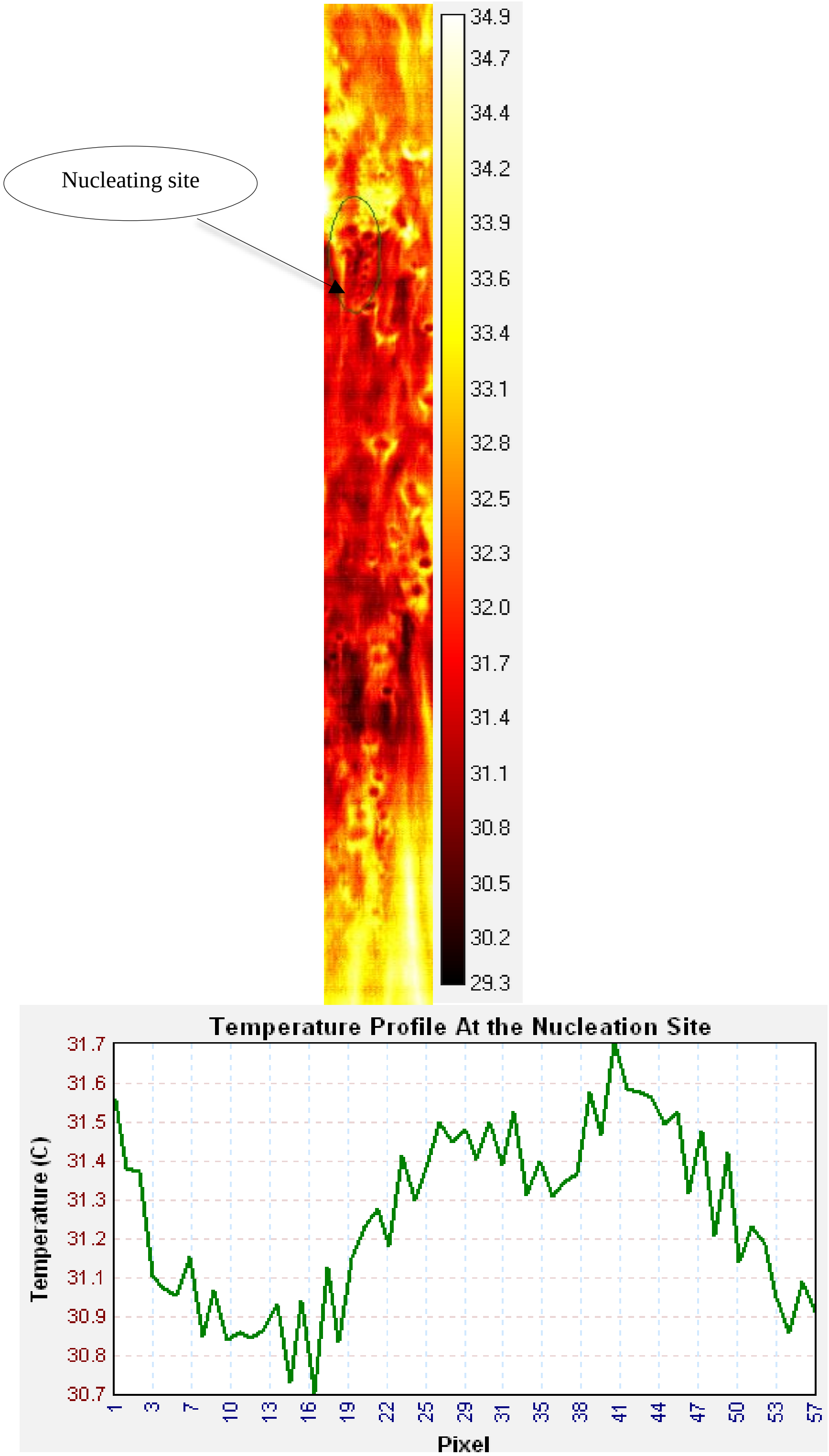

Figure 2.18: Information obtained from the IR camera (top) IR image and (bottom) liquid temperature profile near heated surface at the selected nucleation site.

2.5.2.2.2 Average Temperature Fields

The processed instantaneous fluorescent images are averaged to reveal the average liquid temperature fields (provided in Figure 2.19). This temperature field depicts the average temperature distributions obtained along the heated wall during the bubbles life span (from nucleation to detachment). The thermal boundary development, in regions where bubbles are sliding, is clearly evident along the wall. And as done in the heated single-phase conditions, short horizontal lines are marked along the sliding distance at 10, 15, 20, 25, and 28mm. Temperature values along the marked lines are extracted and plotted against the radial distance in Figure 2.20. Each temperature value obtained along the line represent the temperature value calculated at the corresponding pixel of that location. The temperature distribution at the lowest axial location appear to fluctuate between 21.5 and 22.5 ºC in areas far from the wall. These fluctuations seem to be more pronounced in the lowest temperature profile than those at the higher axial locations. This is because the lower axial regions in the test channel appear noisier than those at higher locations. The temperature profile grows largely near the wall (at around 1 mm radially) to reach a temperature value of 28 ºC just near the heater. The higher temperature profiles (at 15 and 20 mm) are shown to develop in between 21.5 and 22.5 ºC in areas far from the wall. The temperature profiles start to increase in values at further distance from the wall than the one seen in the lowest temperature profile. This trend signifies the developing thickness of the thermal boundary layer. In regions just near the wall, the temperature profiles (at 15 and 20 mm axially) finish at around 30 ºC. The highest profile (at 25 mm) is shown to develop at slightly higher values especially near the wall (below 2 mm radially), and it reaches about 30.5 ºC at the heater region (within similar range of values obtained by the IR camera). The radial gradual spread of profiles with axial distance is expected due to the increasing bubbles' layer thickness and bubbles' velocity as sliding upward. As the bubbles gain momentum once sliding along the heater, they appear to push the liquid outward, and with continuous mixing and stirring, the thermal boundary layer grows in thickness. The bubbles dynamics upon sliding, for similar flow rates with varying heat flux inputs, is explored thoroughly in a later chapter. Figure 2.21 shows the same temperature distributions for this condition addressed above but with an extra profile obtained at the detachment location (at around 28 mm axially). At this point, the bubbles start deforming which enhances the liquid mixing. This is seen as the temperature profile appear to drop from about 31.5 ºC (at the wall) to around 26 ºC (at approx. 0.4 mm radially) before it goes back up in value and continue to fluctuate, until it falls to the bulk temperature values at 3 mm radially. As mentioned earlier, this temperature variations is attributed to an enhanced liquid mixing induced by a detached and deforming bubble, in which a cold liquid is drawn from the top of the bubble to the underneath, and as a result, a hot liquid get replaced when leaving from bottom of bubble toward the colder regions.

Figure 2.22 shows the average temperature field for the high heat flux (36.9 kw/m^2) with low Re (8121). Figure 2.23 and 2.24 demonstrate the extracted radial temperature profiles at the axial locations of interest. Similar trends are observed in this conditions with some exceptions. The gradual growth in the thermal boundary layer thickness can be seen here as well exhibiting a similar behavior. However, the temperature values, for all axial profiles, just near the heater appear to be slightly lower than those shown in the previous case. Figure 2.25 shows the IR image obtained for this condition. The IR image also displays a lower liquid temperature value just near the wall ranging between 28.8 C and 30. 4 ºC, which is comparable to range of values obtained the fluorescent images. It is worth noting that at a higher flow rates, the bubbles can grow smaller in size, before detachment, but move at a higher velocity (than those in the lower flow rates). The bubble behaviors at the higher flow rates induce higher turbulence levels, which enhance the liquid mixing.

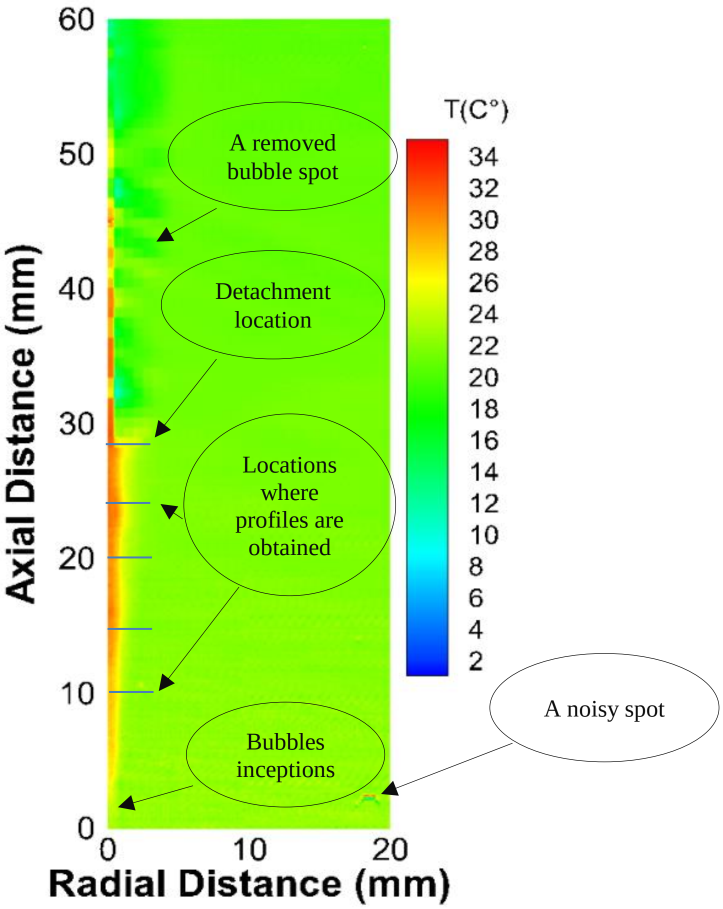

Figure 2.19: Average temperature field obtained for high boiling (36.6 kw/m^2) and high Re (20523).

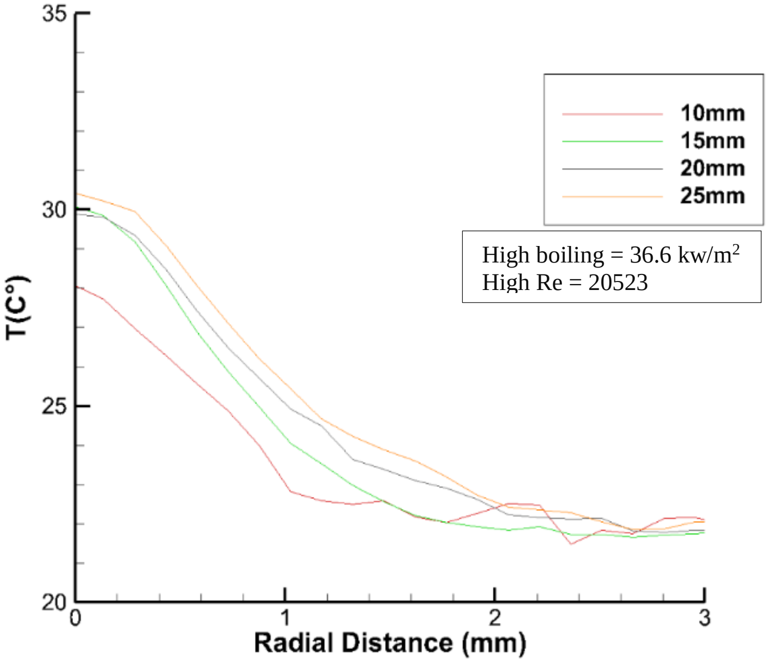

Figure 2.20: Radial temperature profiles of four axial locations with high boiling (36.6 kw/m^2) and high Re (20523).

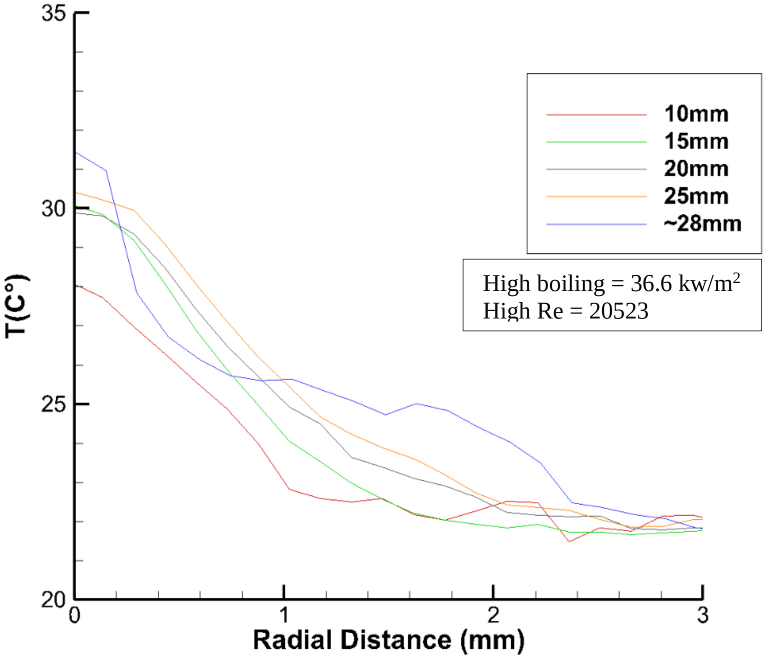

Figure 2.21: Radial temperature profiles for five axial locations with high boiling (36.6 kw/m^2) and high Re (20523).

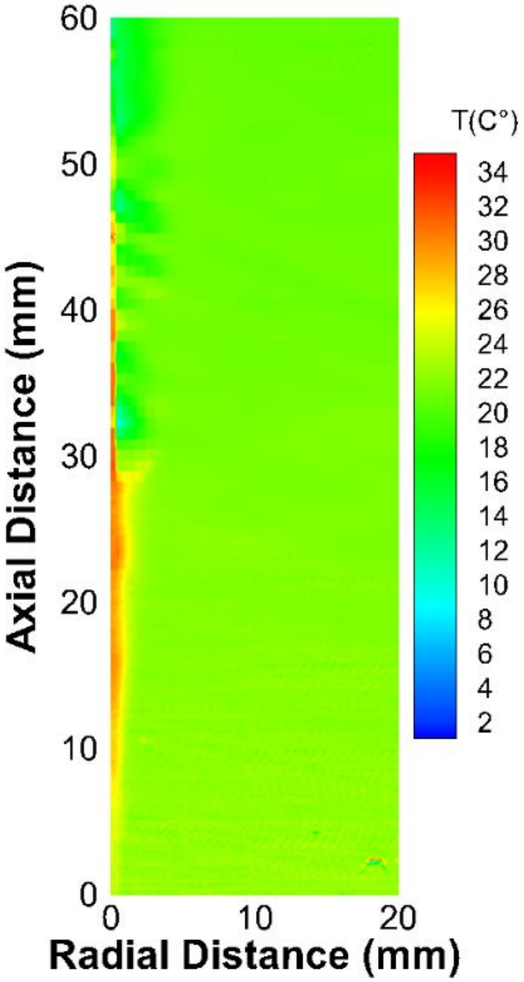

Figure 2.22: Average temperature field obtained for high boiling (36.6 kw/m^2) and low Re (8121).

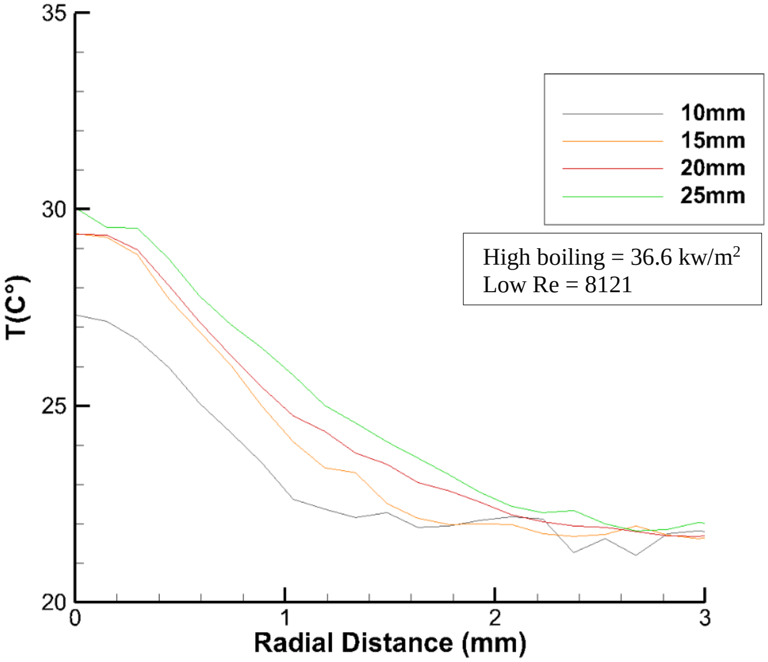

Figure 2.23: Radial temperature profiles for four axial locations with high boiling (36.6 kw/m^2) and low Re (8121).

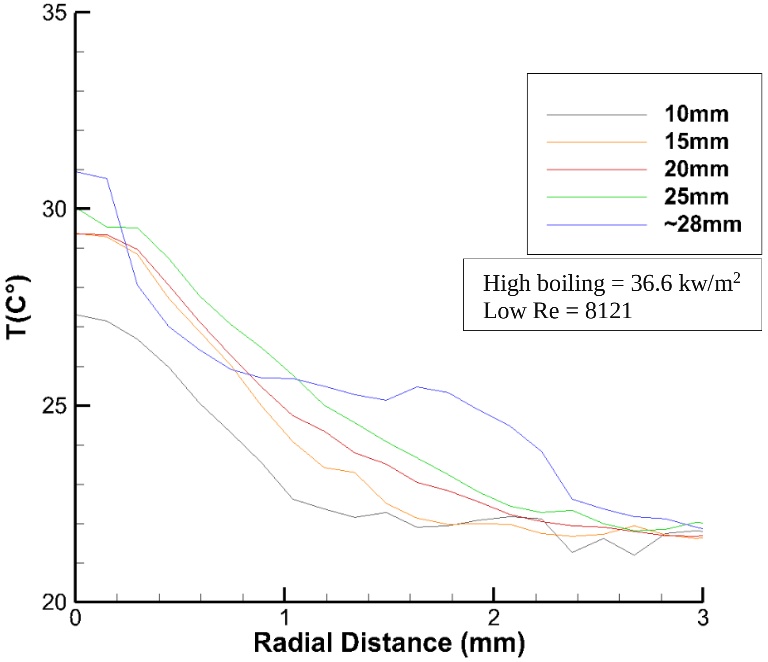

Figure 2.24: Radial temperature profiles for five axial locations with high boiling (36.6 kw/m^2) and low Re (8121).

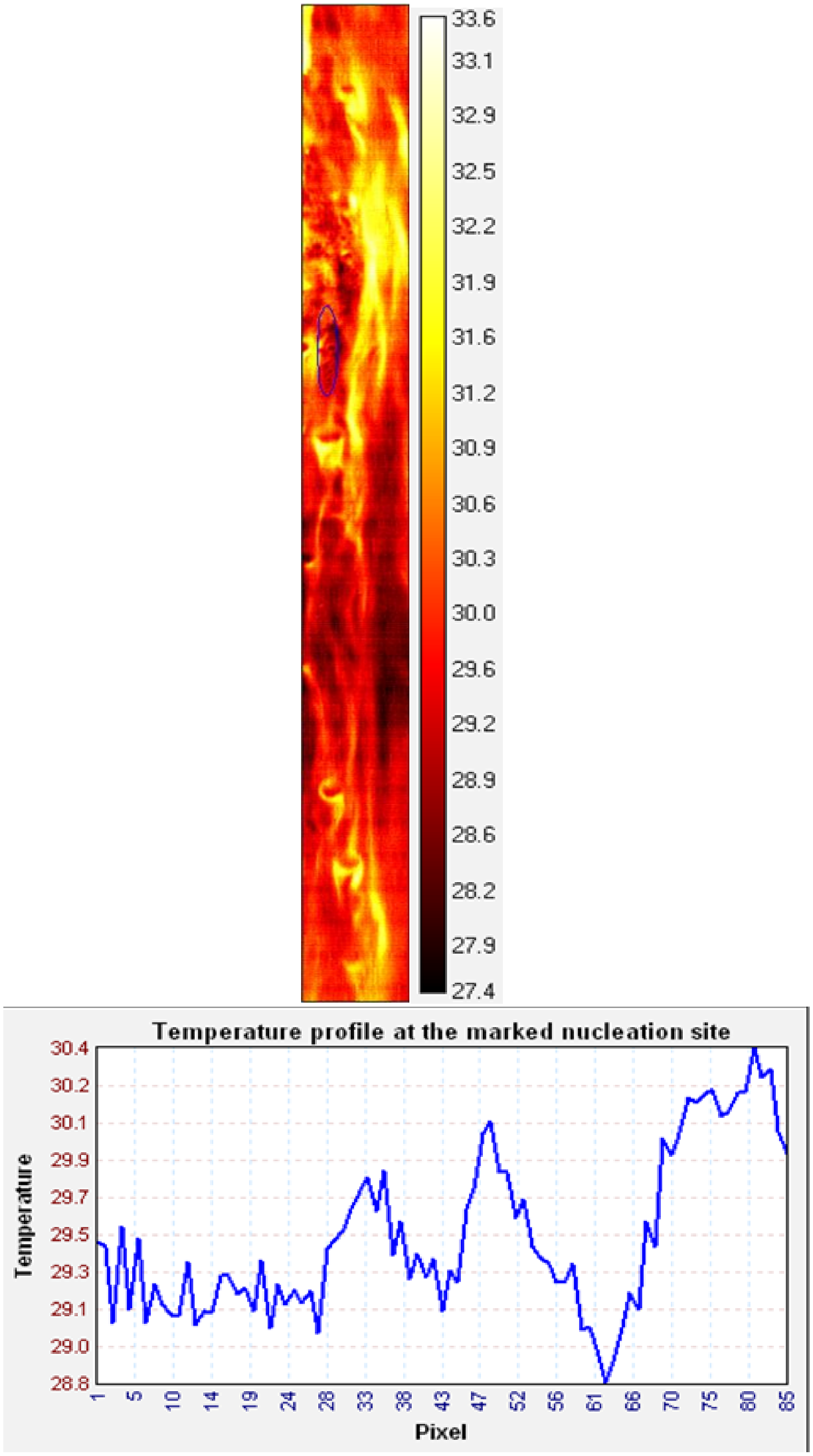

Figure 2.25: Readings by the IR camera (top) IR image and (bottom) temperature profile near the heated surface at the nucleation site (low Re and high boiling).

The low boiling conditions (30.9 kw/m^2) with the same flow rates presented above (of high and low Re) are shown below. Figure 2.26 depicts the average temperature obtained for the low boiling with high Re. It is clearly shown that the thermal boundary thickness is thinner than those in the high boiling cases. This is expected due to the lower heating input and as a result smaller bubble sizes with lower velocities. The temperature profiles obtained at the axial locations of interest (provided in Figure 2.27 and 2.28) show a similar trend seen in the previous conditions but with a less radial spread due to the thinner boiling layer. The temperature values at the wall are in range of 27.5 ºC to 30 ºC. This range of temperature is also obtained by IR camera images. IR images for the low boiling conditions are provided in appendix A for reference.

Figure 2.29 demonstrate the average temperature field for the low boiling case with the low flow rate. Figure 2.30 and 2.31 show the temperature distributions at the selected axial locations. The temperature profiles develop with same fashion seen previously. This condition represent the low heat flux with the low Re, and so the temperature profiles show the lowest values obtained at the heated wall. For IR images in this condition, please refer to appendix A.

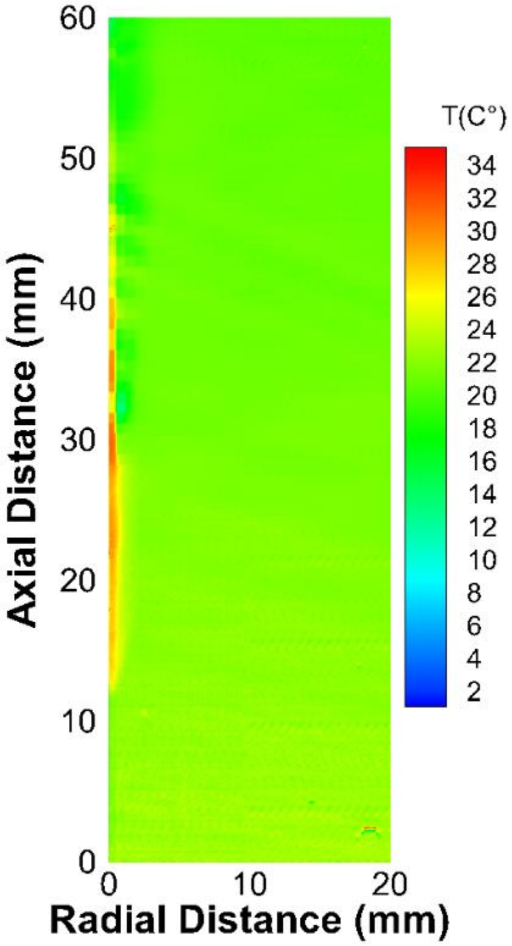

Figure 2.26: Average temperature field obtained for low boiling condition (30.9 kw/m^2) and high Re (20523).

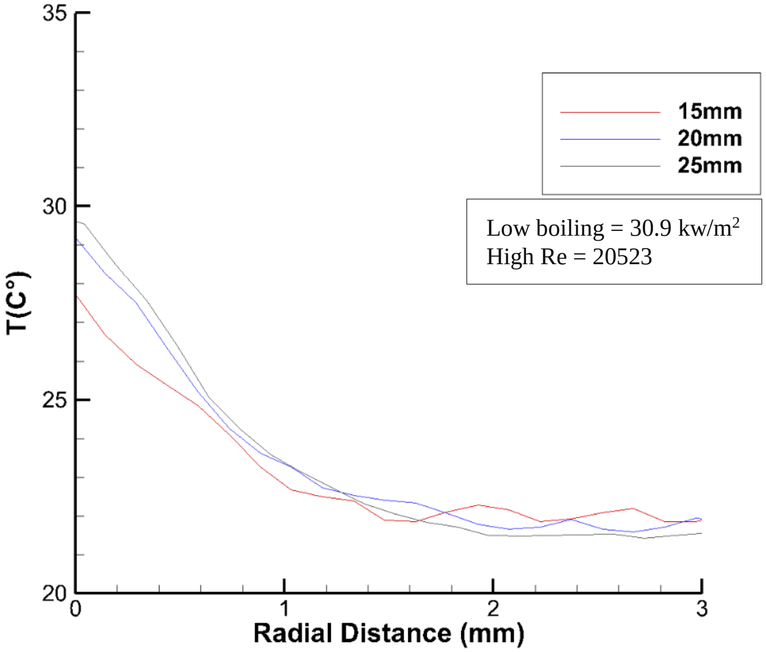

Figure 2.27: Radial temperature profiles for three axial locations with low boiling (30.9 kw/m^2) and high Re (20523).

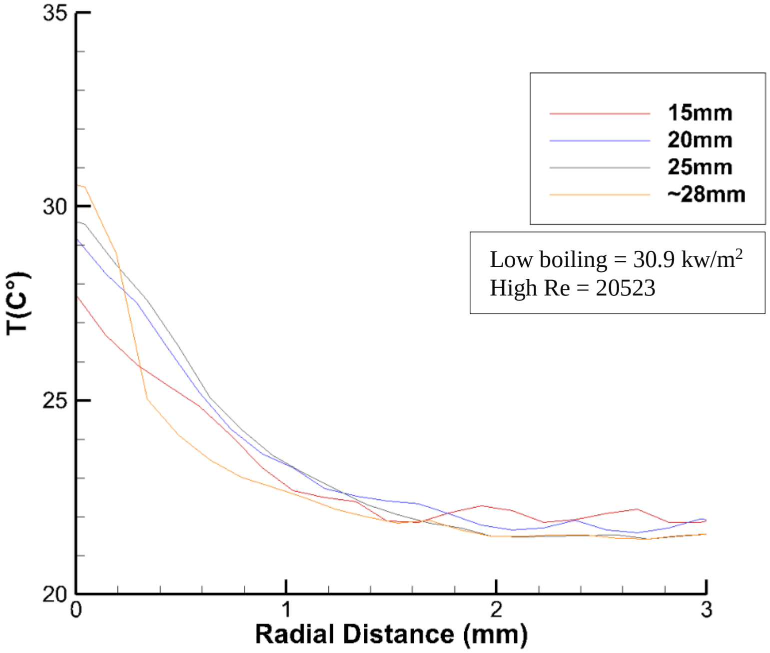

Figure 2.28: Radial temperature profiles for four axial locations with low heat flux (30.0 kw/m^2) and high Re (20523).

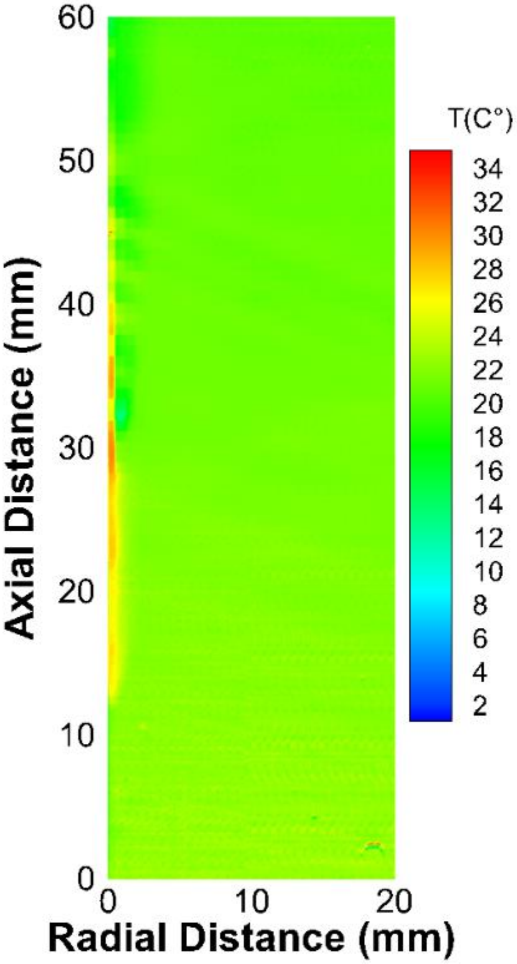

Figure 2.29: Average temperature field obtained for low boiling (30.9 kw/m^2) and low Re (8121).

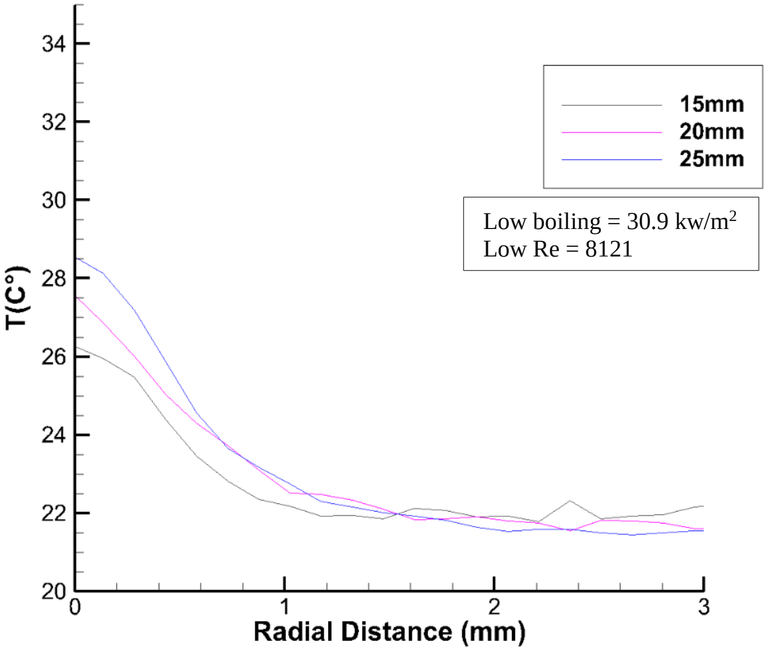

Figure 2.30: Radial temperature profiles for three axial locations with low boiling (30.9 kw/m^2) and low Re (8121).

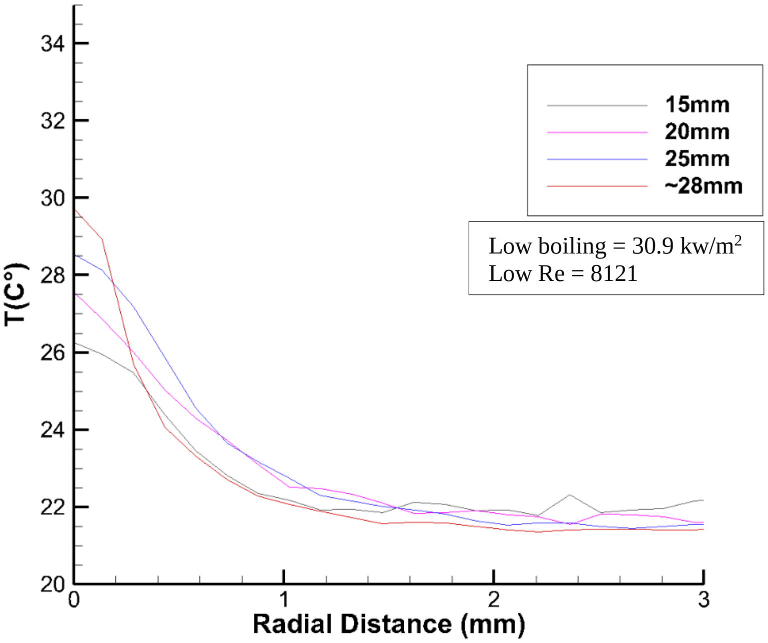

Figure 2.31: Radial temperature profiles for four axial locations with low heat flux (30.9 kw/m^2) and low Re (8121).

For all the six conditions presented above, the temperature distributions at the highest axial location (at 25 mm) are taken and plotted together in Figure 2.32 for comparison. In the single-phase cases, both of the given flow rates are of comparable values in regions far from the heated wall. As approaching the heater, there is no noticeable difference in their boundary layer thickness. The low flow rate profile shows a higher temperature value at the wall (around 28.5 ºC) in comparison to the higher flow one with about 27.3 ºC. In single-phase conditions, the lower flow rates are expected to reach higher temperature values near the heated wall, which is a trend seen in other studies. The thermal boundary layers in the both of single phase conditions are shown to be much smaller than those obtained with the two phase flow conditions, as expected.

In the low boiling conditions, the low Re case appear to spread further in radial direction than the case with high Re. As seen in the single-phase conditions, the lower flow rate reaches a higher value (~29.5 ºC) at the wall than the one in the high flow (~29 ºC). The bigger bubble sizes, induced in the low flow rates, appear to push the liquid further away from the heated surface causing a wider spread in the thermal boundary layer. At this boiling level, the spacing between the developing profiles appear to be bigger than those observed in other conditions, presumably due to higher bubble size variations with changing flow rate. Both of these profiles seem to drop, as moving away from the heater, to the bulk temperature range (between 21 and 22 ºC) at around 2 mm and merge together at approx. 2.1 mm. This bulk temperature range agrees with values registered by the thermocouples.

The highest heat flux conditions (high boiling cases) demonstrate the broadest thermal boundary layers due to a larger size of bubbles, which gives rise to a higher momentum. The lower flow condition shows a slightly wider radial spread than the one seen in the high flow case. Both of these flow rate profiles merge to reach about 31 ºC at the heated wall, which agrees with temperature readings obtained by IR camera. As moving away from the wall, the temperature distributions decrease in value and collapse together to reach the bulk liquid temperature of 21.9 º at approx. 2.4 mm radially. And then, it continues to fluctuate between 21 and 22 ºC. As mentioned above, this range of temperature is observed in the reference temperature readings by the thermocouples at the inlet and outlet. The influence of the varying heat flux level, with different flow rates, on the temperature distributions is clearly evident in the presented temperature profiles.

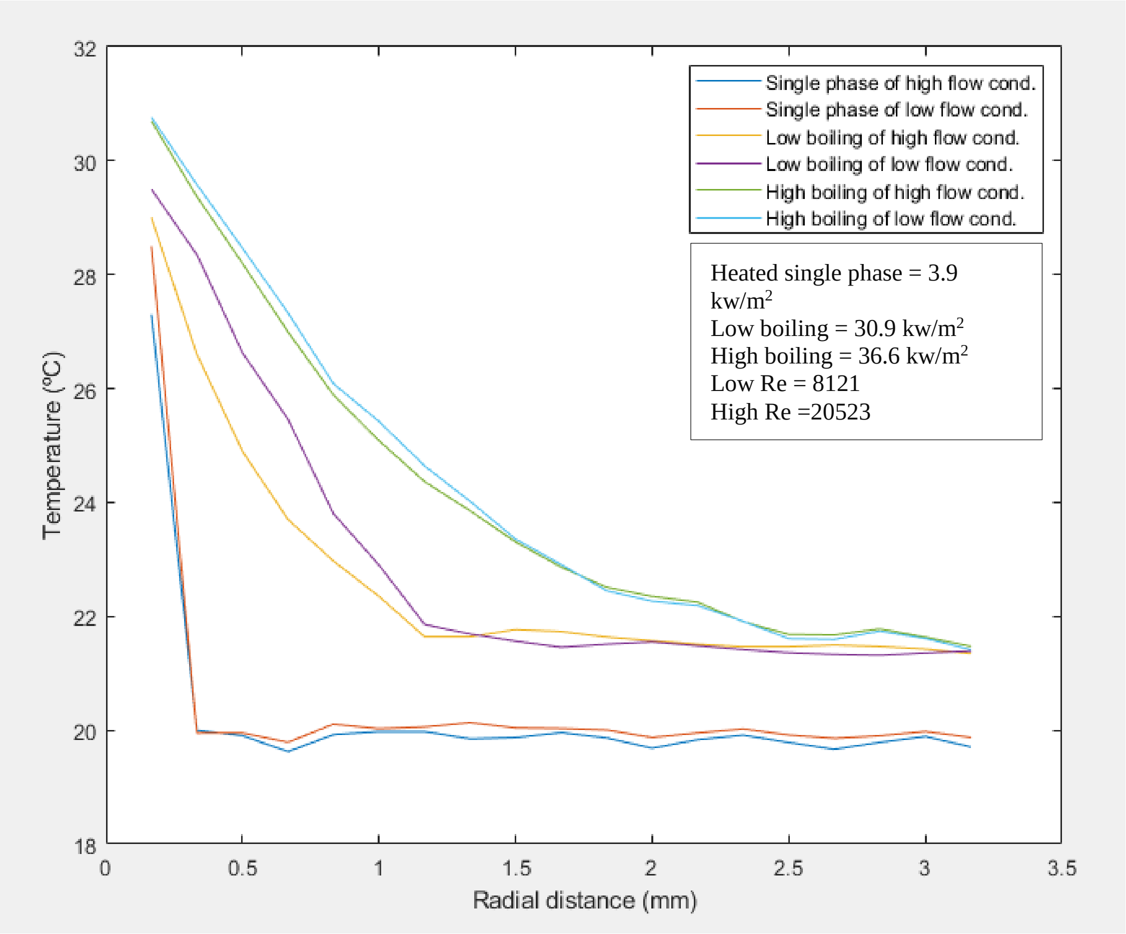

Figure 2.32: Liquid temperature distributions for all conditions obtained at the highest of four axial location (25 mm).

2.5.3 Liquid Temperature Fluctuation Intensity

The fluctuation in temperature values occurs naturally in turbulent flows. The liquid temperature fluctuation intensity is defined as the root-sum-square of a fluctuating component in an instantaneous temperature measurement. This fluctuating component can be obtained by the mathematical formulation of the Reynold’s decomposition given as the following,

$$T(t) = \bar{T} + T'(t) \tag{2.3}$$

$$T_{rms} = \sqrt{\overline{T'(t)^2}} \qquad (2.4)$$

Where $T(t)$ is the measured instantaneous temperature value, $\bar{T}$ the time-averaged temperature measurement, $T'(t)$ is the fluctuating component in the temperature measurement, T_{rms} is temperature fluctuating intensity. The computed temperature intensity is then divided by the time-average temperature to obtain a normalized version of its quantity ($\frac{T_{rms}}{\bar{T}}$). Figure 2.33 below displays the normalized temperature intensities plotted against the radial distance for all the six conditions for comparison.

It is clearly shown that the temperature intensities increase largely as moving toward a higher turbulent regions (near the heated wall). This increase in turbulent intensity is seen to grow with increasing heat flux. The lower flow rates appear to induce a higher level of intensity especially near the heated surface in both of the boiling conditions. This feature is seen to be more pronounced in the low boiling case. The impact of boiling bubbles on the intensity profiles is evident as significant increase in intensity values are obtained as approaching the heated wall.

The intensity profiles obtained for the heated single-phase are observed to be comparable but with a slight increase in the low flow condition toward the wall.
The intensity growths with wall heat flux is a known effect in single-phase flow (Roy et al. 1986; Hasan et al. 1990, Roy et al. 1991). It is well-known that in the single-phase liquid flow, temperature fluctuation intensity increases with a decrease in flow rates (Hasan et al. 1990, Roy et al. 1991).

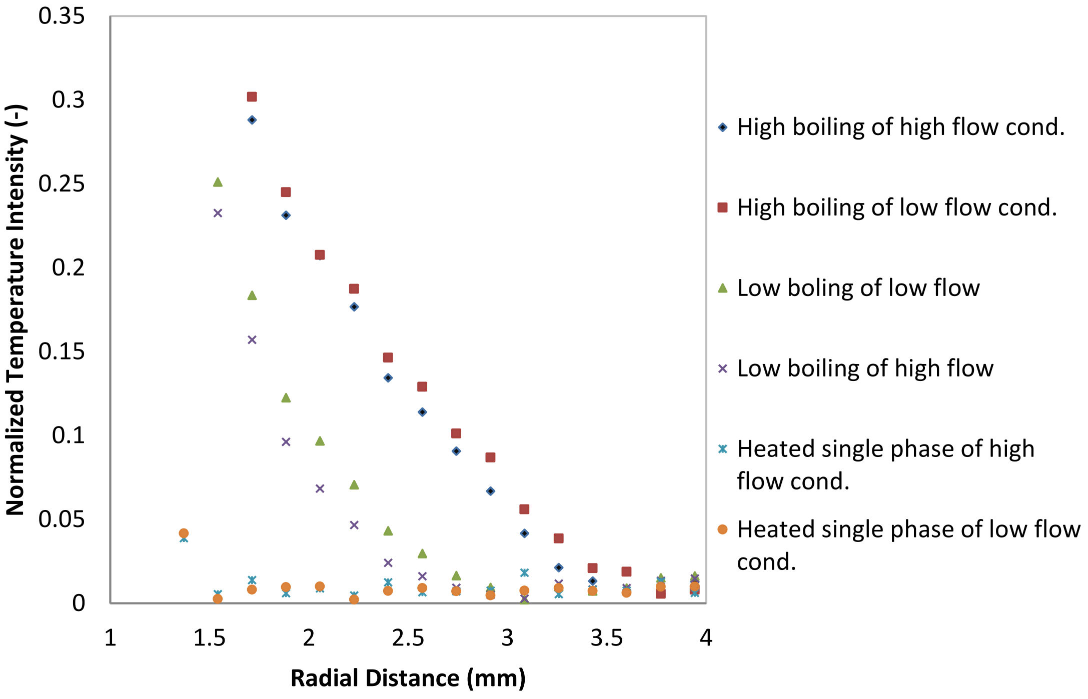

Figure 2.33: Normalized liquid temperature intensity profiles for all six conditions obtained at the highest of the four axial locations (25 mm from).

2.5.4 Temperature Distribution around a Growing Bubble

The temperature profile at the bubble-liquid interface is addressed in this section. Figure 2.34 (left) displays a sliding and growing bubble in a selected condition, namely, high boiling and low flow rate. The sliding bubbles in this condition are obtained to be the biggest in size in comparison to other conditions and so information near the interface are more apparent. The bubble in Figure 2.34 (left) appears masked and only liquid information around the bubbles are considered. The liquid information here is obtained around the bubble just before the bubble's detachment. A horizontal line is marked at the interface where the temperature profile is mapped out. The line probe marked at the interface spreads over only 6 pix (~1 mm) in the radial distance.

Figure 2.34 (right) shows the temperature distribution at the location of the line probe. The temperature profile through the interface appear to fluctuate between 22 and 23 ºC over a distance of about 5 pix (0.86 mm) radially. It then rises up largely just near the bubble's domain to about 35 ºC, which is a value very close the saturation temperature (34 ºC) as expected, over a radial distance of approx. 1 pixel (0.14 mm). This temperature rise happens over a thin region as shown. This is, in part, due to the working liquid's thin thermal boundary layer and also a low optical resolution by the imaging system at bubble-liquid interface. The information at the bubble's boundaries can also be lost by the presence of the bubble's shadow and/or the laser light reflections near the bubble and at the bubble's surface. However, the laser reflections in this study is minimized by the use of the optical filter at the high speed camera.

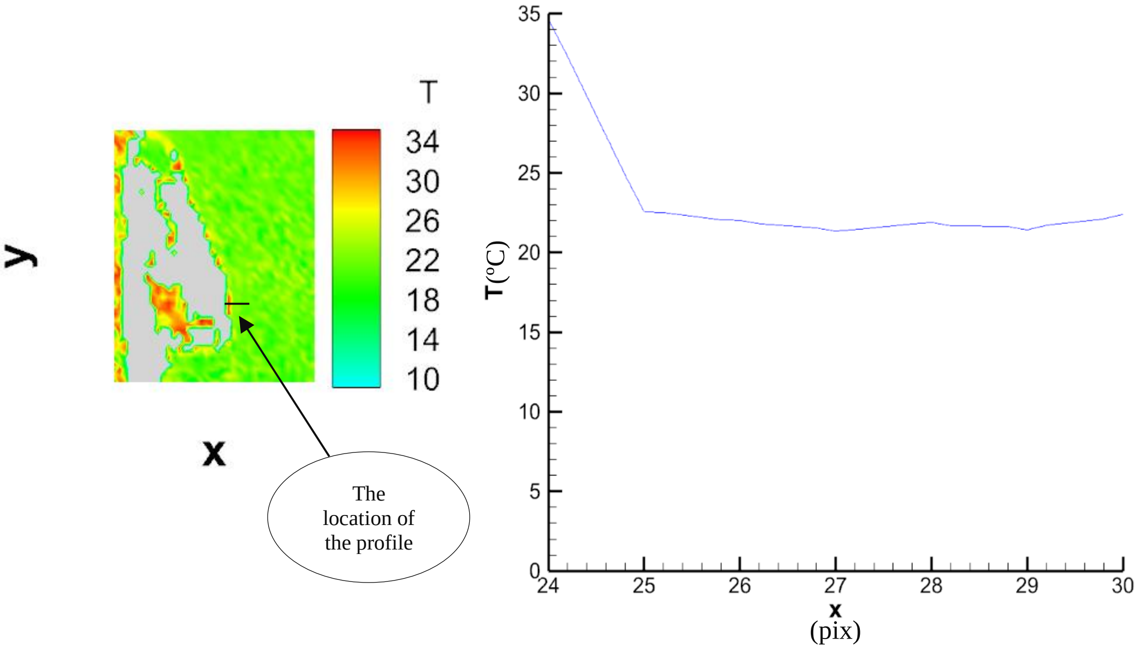

Figure 2.34: A closer look at a growing sliding bubble just before detachment (left) and the temperature distribution at liquid-bubble interface (at the marked line) (right).

2.5.5 Sliding Bubbles Velocity

The sliding bubbles velocity estimations are approached in a semi-automatic fashion, in which four different individual bubbles are tracked as they slide along the heater in each condition. The shadowgraph images are utilized for this purpose. First, a stack of shadowgraph images is adjusted in ImageJ (a Java based software designed to process images) to obtain sufficient contrast between the tracked bubble (dark) and the background (white). A single particle tracking (SPT) feature in ImageJ is then employed in such a way that information regarding the bubbles centroid coordinates in 2D is extracted over time. A point probe is used to locate the bubble’s centroid, and then it is tracked from the start of the sliding distance to the marked line probe. This line probe represents the axial distance of interest (where detachment occurs at around 28 mm axially) and where the tracked bubble velocity is measured. With each frame, the point probe is moved with the bubble’s centroid, and the location coordinates are recorded in X, Y. When the point probe reaches the horizontal line, the sliding time (in frames/sec) and distance (in pixel) are recorded to estimate the velocity at the line probe.

The average of the bubble velocities obtained for each condition is provided as 0.18, 0.20, 0.21, 0.28 m/s for low boiling and low Re, low boiling and high Re, high boiling and low Re, and high boiling and high Re, respectively. As expected, the higher boiling conditions show higher velocity values than those obtained in the low boiling cases. This is due to the higher heating input goes into the system inducing bigger bubble sizes sliding with higher momentums. And, at higher flow rates, the bubble velocities are also seen to increase in both of the boiling levels. The condition of the high heat flux (36.6 kw/m^2) with high Re (20523) is shown to record the highest bubble velocity (0.28 m/s), whereas the condition with low boiling (30.9 kw/m^2) and low Re (8121) shows the lowest velocity value (0.18 m/s).

2.6 Experimental Uncertainties in LIF Measurements

As shown in equation 1, the LIF thermography assumes a linear relationship between the fluorescence signal and the incident laser light. However, this assumption is valid up to a certain limit in the laser power depending on the type of dye and the solvent used. And so, a deviation from the linearity assumption, due to high laser power, has been reported in the literature. In general, the relationship between the incident laser light and fluorescence signal can be described as linear at low laser power systems. The same linearity assumption goes for the dye concertation. For increasing dye concertation, the fluorescence signal can develop in non-linear fashion. Typically, LIF thermography studies are performed under 1 mg/L with water as a solvent. For the purpose of this study, the RhB concertation used here is approx. 0.25mg/L.

Additionally, the spatial resolution of the recorded images can be limited by the optical setup and the uniformity in illumination (obtained by a laser sheet). The temporal resolution can also be limited by the sensitivity of the high speed camera used and the temporal averaging required to obtain a high signal-noise ratio. In this context, the signal-noise (SNR) ratio is defined as a given signal at some location in heated single-phase or boiling images divided by the corresponding signal obtained from the time-averaged calibration image. In order to estimate the uncertainty in the measurement due to a non-uniformity in the laser illumination and the camera sensitivity, signal-noise ratio is determined over temporal averaged images. To this end, the heated single-phase images (in low flow rate condition) are time-averaged. The region of interest in the averaged image is then segmented radially into 4 x 8 pixels, and illumination intensity is measured at each segmented area. The intensity given by a grayscale is plotted against the radial distance in Figure 2.35. Similarly, the illumination intensities in the calibration images are obtained for the background removal. The segmented signal determined from the heated case is then normalized by the corresponding signal from the temporal-averaged calibration image to obtain the signal-noise ratio. Figure 2.36 shows the single-noise ratio (SNR) versus the radial distance of the measurement section. The single appears to be relatively flat across the radial distance, but it starts decreasing as approaching the heated wall (below 1 mm radially). This area associated with a drop in the signal contains the developing thermal boundary layer for the heated case. Clearly, the temperature variations are higher in this region. This suggests that the fluorescent signal becomes weaker in regions with higher temperature (near the heater), and so the single-noise ration goes lower (to below 1). This trend highlights the increase of the measurement uncertainty in the near-wall areas. In general, a high signal noise-ratio is desirable in LIF work for more accurate temperature measurements.

Similarly, the signal-noise ratio is provided along the sliding distance in the axial direction and shown in Figure 2.37. The obtained plot illustrates the decrease in the ratio with the axial distance, a similar behavior seen in the previous plot. The drop in signal is shown to grow with the increasing temperature in the direction of the sliding bubbles. Therefore, the uncertainty is believed to be the highest in the near heated surface region and especially where temperature reaches its highest value toward the end of the sliding distance. The plot also demonstrates some fluctuations in in the signal near the bottom of the channel. These fluctuations highlight the non-uniformity in some noisy spots shown in the lower end of the test section.

The signal-noise ratio around the growing bubble is obtained from the instantaneous temperature field in locations where the temperature profile are mapped out in Figure 2.34. The ratio is shown to fluctuate between 1 and 0.99 in regions far from the bubble's domain. The fluctuating ratio signifies a nosier temperature field calculated from the instantaneous processed image. The ratio is also shown to decrease sharply to below 0.93 in regions where temperature rises just near the liquid/bubble interface.

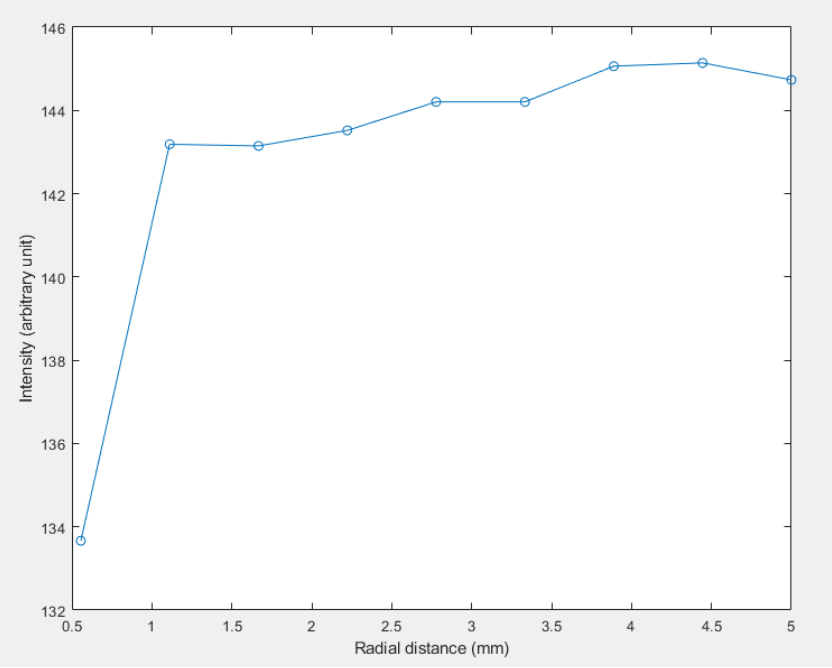

Figure 2.35: The fluorescent signal intensity obtained across the radial distance of the test section for nine segmented areas (8 x 4 pixel).

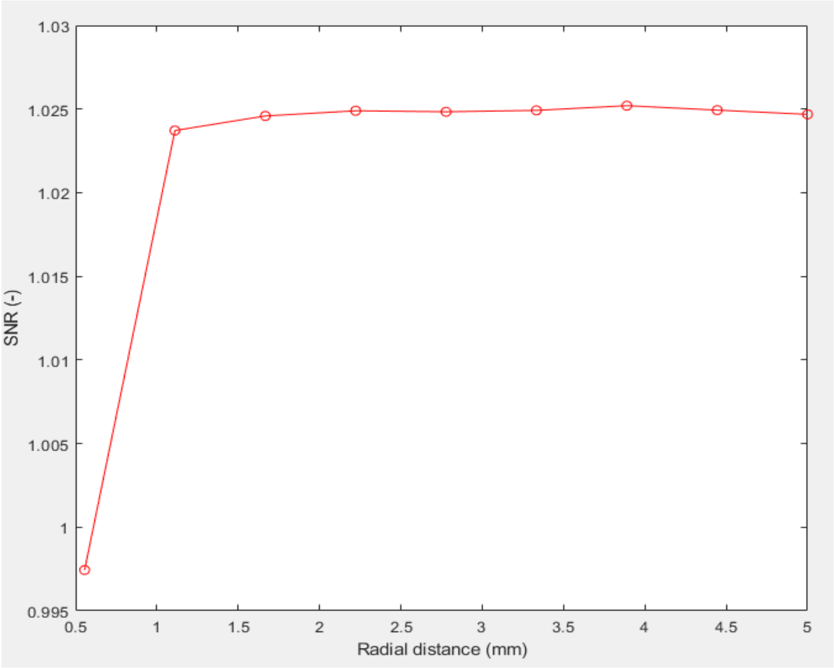

Figure 2.36: Signal-noise ratio obtained across the radial distance of the test section for nine segmented area (8 x 4 pixel).

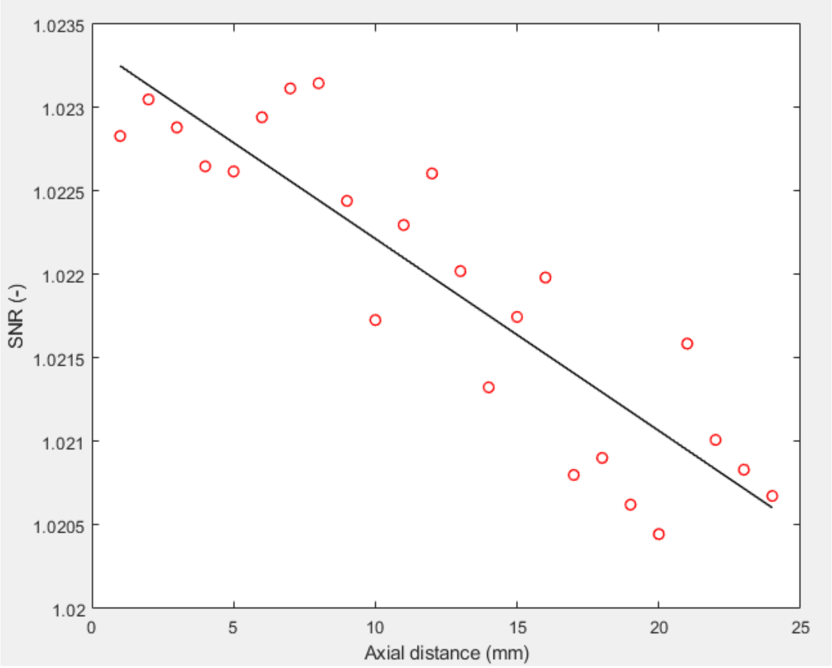

Figure 2.37: Signal-noise ratio obtained along the axial sliding distance for 24 segmented areas (8 x 4 pixel).

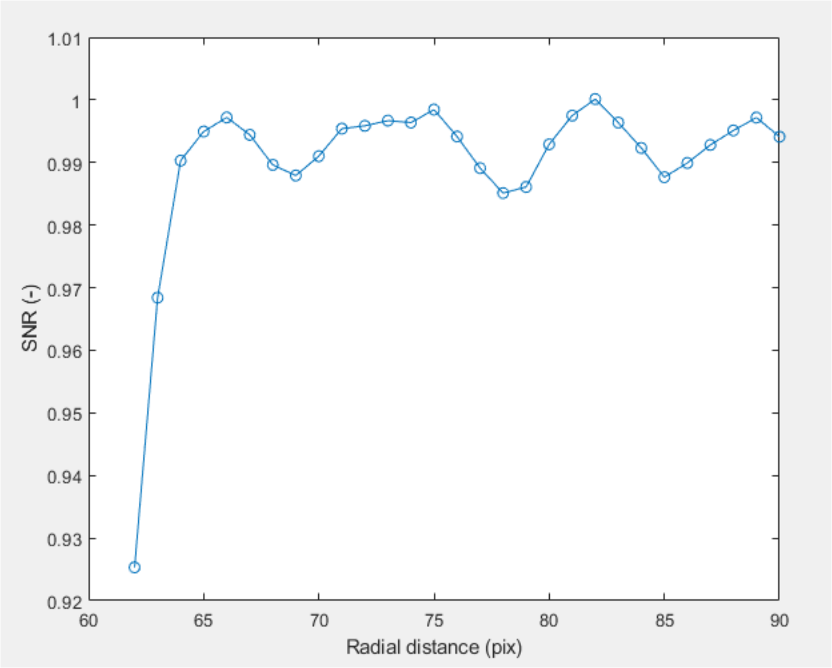

Figure 2.38: The signal-noise ratio obtained around the growing bubble across the horizontal line probe location given for the temperature profile.

The radial temperature profiles obtained for all the conditions are shown to vary around 22 ºC ± 1ºC, in regions far from the heated wall. The average reference temperature value obtained by the thermocouples, at the inlet and the outlet, is 21.62 ºC ± 0.16 ºC. The reference temperature appears to be in a good agreement with the temperature range provided by the LIF measurements. It is worth-noting that the temperature uncertainty in the thermocouples is 0.75%. However, in the near-wall regions, the uncertainty is expected to go higher due to a weaker fluorescent signal reaching the camera sensor, as shown in Figure 2.36. The discrepancy among temperature profiles is observed to grow as moving radially toward the heated wall. For example, the liquid temperature values just near the heated wall, as shown in the profiles in Figure 2.10, tend to vary between 28 and 30.5 ºC in the high boiling and low Re condition. On the other hand, the temperature profile obtained by IR camera, along the axial distance of the sliding bubble, displays a temperature variation between 30.7 and 31.7 ºC. This shows a clear wider variation in the temperature range measured by the fluorescent images. Such discrepancy in temperature measurements, in higher uncertainty area, can be minimized by improving the fluorescent signals. Modifications and improvements to the measurements are suggested in the future work section.

The absorption and emission spectral conflict is another source of error that can occur in LIF work. For a fluorescent dye, a certain range of overlap between absorption and emission spectrum is standard. In this overlapping region, processes known as "self-absorption and "remission", in which an emitted photon is reabsorbed and then remitted at a different wavelength, can be experienced. The interference between spectra can lead to a dependence of the fluorescence signal on the amount of absorption in the overlapping region. The overlapping region is minimized in this study with the use of the bandpass filter of a narrow band-width. Such filter can transmit only photons with wavelengths of interest.

2.7 Conclusion

The LIF temperature measurements study presents experimental investigation of the influence of nucleate boiling on temperature fields near wall/liquid interface and around a growing bubble. The whole-field method of LIF is shown to be useful to measure the developing thermal boundary layer, due to nucleate boiling, in contactless fashion using a fluorescent dye with a high speed camera. A high resolution imaging capability is required to resolve the temperature variations at the interfaces. In this work, six experimental conditions with varying flow rates and heat fluxes (two heated single-phase and four boiling cases) are investigated. The development of the thermal boundary layer is mapped out for each condition and the temperature profiles are provided in the radial direction. Four axial horizontal line probes are used to extract the temperature profiles near the heated wall region and a little further from the wall (within about 4 mm radially). The concomitant increase in the thermal boundary layer's thickness with axial distance is evident for all conditions. As expected, the boiling bubbles have brought significant changes to the temperature distributions near the heated wall region, as the thermal boundary layers are shown to spread over a wider radial distance (in boiling cases) than those obtained for the heated single-phase conditions. In boiling conditions, the higher heat flux (36.6 kw/m^2) induces bigger bubble sizes, and so thermal boundary layers are seen to grow bigger with the bubble sizes. The layer thickness is shown to slightly increase with the lower flow rates in the boiling cases. A similar behavior is expected (although not very noticeable due to the thin boundary layer with no enough resolution) in the heated single-phase. The local thermal response of liquid just near the heated wall, for all conditions, is measured with the IR camera. The temperature profiles obtained by the fluorescent images just near the wall region are shown to be within ± 2 ºC of the temperature values obtained IR camera (between 30.9 and 31.9 ºC). The temperature fluctuations in profiles far from the wall are shown to be with ± 1 ºC of the average reference temperature for the bulk fluid registered by the thermocouples (21.6 ºC).

CHAPTER III

PARTICLE IMAGING VELOCIMTRY (PIV) FOR VELOCITY MEASUREMENTS

3.1 Introduction

On subcooled boiling studies, the analysis of near-wall turbulent region requires methods that are efficient on tracking the tracer particles suspended in the flow because in the near-wall region, the image noise along with the high velocity gradients can decrease the accuracy of particle tracking (Estrada-Perez, 2014). Nowadays, the study of turbulent flow has developed enormously with the availability of high laser power devices and fast digital processors. This has led to quit sophisticated techniques in whole field velocimetry such as Particle Image Velocimetry (PIV). This method is non-intrusive and is considered a full-field flow visualization technique, which provides quantitative and qualitative information of flow under study with high accuracy and spatial resolution. The underlying principal behind this method is that an instantaneous velocity field can be measured by recording a position of images generated by tracer particles suspended in a fluid at successive time instants. The assumption embedded in this method is that the flow tracers follow closely the fluid motion with minimal lag. This assumption is seen to be valid for a wide variety of flows provided that the tracers are small enough and of comparable density to fluid’s density. In PIV methods, the correlation-based algorithms are widely used. Some algorithms use the Fast Fourier Transform (FFT), which expedites the processing speed (Willert and Gharib, 1991). The results from the cross-correlation operations represents the mean displacement of all particles with the sub-image. The limitation in the PIV cross-correlation technique can be seen in the spatial resolution in which, for example, the flow scales smaller than the sub-image dimensions. And so, choosing smaller sub-image dimensions, to enhance the spatial resolution, can sometimes lead to measurement errors because fast moving particles leave the sub-image regions faster than the slower moving ones. This can lead to a bias in the measurements toward slower velocity values, which affects the overall capability of characterizing high turbulent regions with high velocity gradients such as areas nearby vortices or close to boundaries.

Unlike PIV, shadowgraph is a visualization method that does not require particle seeding and a laser light for illumination. Typically, an LED light or halogen lamb are sufficient for illumination purposes. Shadowgraph technique is a non-intrusive method that is usually used to obtain bubble dynamics' information such as bubble velocity, size, and void fraction. This technique is widely used in research due to its simplicity with low cost, and it can be applied with high frequency measurements.

3.2 Literature Review

The combined PIV and shadowgraph technique was used by Lindken and Merzkirch (2002). They performed an experiment in which they injected bubbles at a Reynold's number of 1,400 into a square tank filled with stagnant liquid and measured the bubble and liquid velocity with a camera. They were able to measure the velocity of the two phases simultaneously. Zaruba et al. (2005) estimated the velocity and the size of bubbles in a rectangular column with 10 cm in width and 2 cm in depth. The bubbles were inserted through an aquarium porous stone with a range of gas velocity of 1-

6mm/s. The bubbles velocity was measured by tracking the centroid of each bubble. No liquid velocities were reported. They concluded that their method had some limitations and improvements would have to be made.

A number of studies have been conducted to measure the liquid turbulence modifications due to boiling process (Lee et al., 2002; Roy et al., 1997; Yun et al., 2010, 2008). Roy et al. (1993) performed one of the early studies on measuring local fields of subcooled boiling parameters. They measured turbulent velocity and temperature field in all-liquid regions adjacent to a subcooled flow boiling layer. They reported significant changes in turbulence structures in the all-liquid regions due boiling. In another study, Roy et al. (1997) used a two-component Laser Doppler Velocimetry (LDV) system to estimate the liquid (refrigerant R-113) and the boiling bubble velocities. The study also included the use of a dual-sensor fiber optical probe (FOP) and a Constant Temperature hot film Anemometer (CTA) to measure the vapor bubble-related parameters and liquid temperature. They were able to measure the liquid turbulence statistics within the boiling layer adjoining to the heated wall. Their findings showed major changes near the heated wall brought by boiling. Situ et al. (2004) were able to measure the flow structure of subcooled boiling flow in an annuals. This study included the use of a double-sensor conductivity probe approach to measure the local void fraction. Yun et al. (2008) conducted subcooled boiling experiments in a 3 x 3 rod bundle. They used a double sensor conductivity probe for the vapor phase measurements and a pitot tube for the local liquid velocity. Yun et al. (2010) measured the local velocity and temperature in a subcooled boiling experiment through a concentric annulus. In their experiments, they used a double sensor optical fiber probe for the local void fraction measurements and bubbles velocity. They also used Pitot probe and a K-type thermocouple for temperature measurements. Lee et al. (2002) measured a local void fraction and velocity profile of void and liquid. These measurements were done using two-conductivity probe for the local void fraction and the velocity and a Pitot tube method for the local liquid velocity. These studies share the characteristics of being limited to a point measurement method. Therefore, a whole-field measurement approaches are needed to provide thorough spatial and temporal information.

The full-field visualization techniques have been used widely in two phase flow studies in order to overcome the limitations that come with point measurement methods (Dominguez-Ontiveros et al., 2006; Hassan et al., 2005; Koyasu et al., 2009; Ortiz-Villaferte and Hassan, 2006). However, there seem to be a shortage of subcooled boiling experimental studies that can employ instantaneous full-field measurement techniques and measure parameters in relevance to two phase flows (Estrada-Perez, 2014). Most of the existing studies focus on measuring parameters of one phase only, probably due to experimental and technical difficulties associated with measuring two phase parameters. In one of full-field measurements studies, Estrada-Perez and Hassan (2010) performed whole-field particle tracking velocimetry experiments in a rectangular vertical channel with a single heated wall. Their focus was on the liquid turbulence modifications due to the wall heating. Their findings were in agreement with the behavior found in previous studies. They were able to provide new insights due to their whole-field measurement method, which have been used in the development of near-wall liquid velocity modeling and in CFD simulation validations (Koncar and Matkovic, 2012).

This work is a continuation of the experimental investigations started by Estrada-Perez and Hassan (2010) and Estrada-Perez et al. (2012), which has the objective to conduct simultaneous Particle Image Velocimetry (PIV), high speed shadowgraph, and infrared thermometry (IR camera) for the subcooled boiling studies. Although these tools have been used in previous works, they have not been attempted to provide simultaneous measurements in subcooled boiling experiments.

3.3 Background

The PIV imaging technique employed here has been used successfully in previous studies to analyze the subcooled boiling flow patterns and turbulence structures. The PIV is a full-field velocity measurement approach used to overcome limitations often come with point measurements methods and provide high fidelity experimental information for model validations.

The velocity vectors (V) , in PIV, are calculated from sub-sections of particle seeded flow by measuring the displacement of particles ($\varDelta X$) between two PIV images($\varDelta t$):

$$V = \frac{\varDelta X}{\varDelta t} \tag{3.1}$$

When the seeded flow field is illuminated with a laser light, a high speed camera, depending on the camera speed, can capture a number of separate frames per second. The images are then divided into sub-section known “interrogation regions”. These interrogation regions are masked with an image masking filter which designed to eliminate the edge effect that may lead to aliased signals (PRANA user manual, 2011). The interrogation regions are then converted to spectral domain to process the cross-correlated between the images by convolving the two Fourier transformed images. The correlation is inversely transformed and the location of a maximum correlation, which signifies the image displacement, is identified. The accuracy of and consistency of the technique can be increased by fitting curves of sub-pixel resolution schemes to the correlation peak.

3.4 Materials and Methods

3.4.1 PIV Experimental Setup, Procedure, and Conditions

The same experimental facility described in previous sections is used here for the PIV experiment with some modifications that are relevant to this study (see Figure 3.1). For each of the boiling condition, given below in table 3.1, simultaneous PIV images and shadowgraph measurements are performed using two high-speed cameras (Phantom R311), a beam splitter, a continuous laser source, a LED backlight illumination system, filter optics, and sliver coated flow tracers (with an average diameter of 13 μm and a density of 1.6 g/cc). The two high speed cameras and the beam splitter (the visualization system shown in Figure 3.3) are mounted on 2D transitional stages to have the capability of adjusting the measuring region along the test section. The laser light sheet is positioned on the measurement region and parallel to the cameras focal area. The visualization system are made to work together in such a way to be able to obtain simultaneous PIV and shadowgraph images. This is done with the use of an external pulse generator which triggers both camera to record simultaneously. A high pass filter is applied to PIV camera to reduce the background noise and obtain a cleaner version of PIV images. The shadowgraph camera is equipped with the optical filter (used previously in LIF experiment) to avoid the laser reflection from reaching the camera sensor. Both high speed cameras are configured to operate at a frame rate of 5000 fps with a resolution of 800 x 320 pixels with an exposure time of 490 µm. The exposure time is selected to allow enough light to reach the camera sensor and obtain satisfactory shadowgraph of bubbles. Figure 3.2-4 provide a photograph of the experimental facility described above.

The experimental conditions considered in this study are given in table 3.1. Four boiling conditions are performed with heat flux values of 16.4 and 42.8 kW/m^2 and Reynold’s number (Re) of 8021 and 20523. Two extra heated single-phase cases are conducted as well to characterize the flow. Prior to taking measurements, the flow tracers are injected into the system and made run throughout the loop to achieve uniformity with a constant inlet temperature of 20 $^{\circ}$C. The Inlet and outlet liquid temperature is measured by the means of thermocouples (type-T). The working fluid is then brought to boiling to induce bubbles at the measurement region. For each condition, a total of 33,324 images are acquired by each camera. The acquired experimental images are then processed and analyzed. In addition to the PIV and shadowgraph data, the infrared thermometry is also employed by the use of the Infrared camera (IR) to obtain measurements of liquid temperature near the heated surface at the nucleation sites.

Table 3.1 Experimental Conditions for PIV.

Set	ΔT [°C]	Heat Flux [kw/m^2]	Re[-]
1	20.83	2.7 (heated single phase)	8121 (low Re)
2	20.65	2.7 (heated single phase)	20523 (high Re)
3	20.83	16.4 (low heat flux)	8121 (low Re)
4	20.65	16.4 (low heat flux)	20523 (high Re)
5	20.83	42.8 (high heat flux)	8121 (low Re)
6	20.65	42.8 (high heat flux)	20523 (high Re)

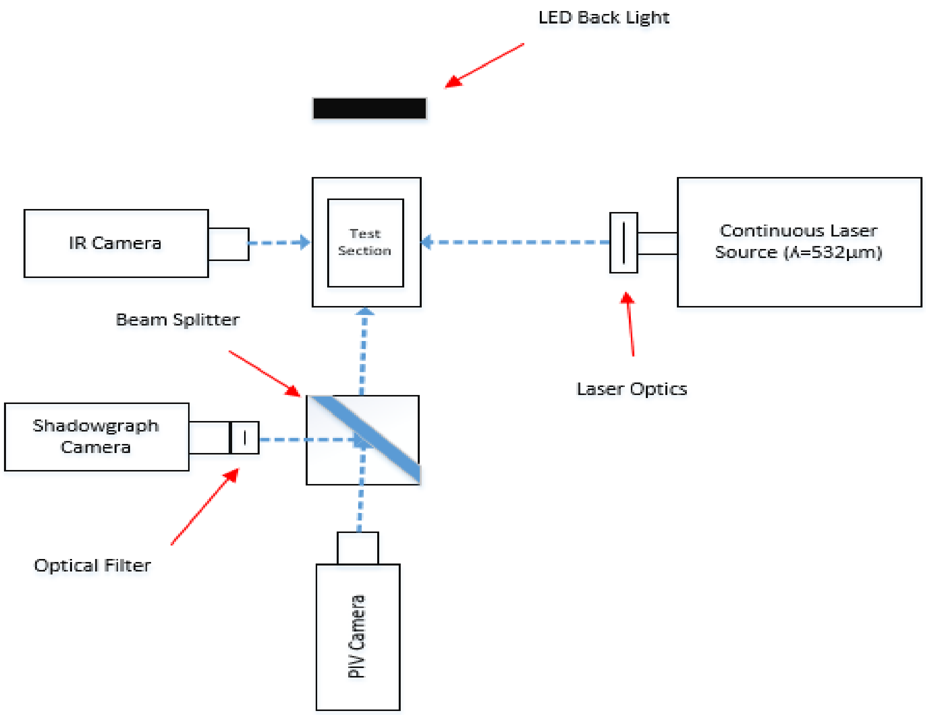

Figure 3.1: A schematic of the PIV experimental arrangement.

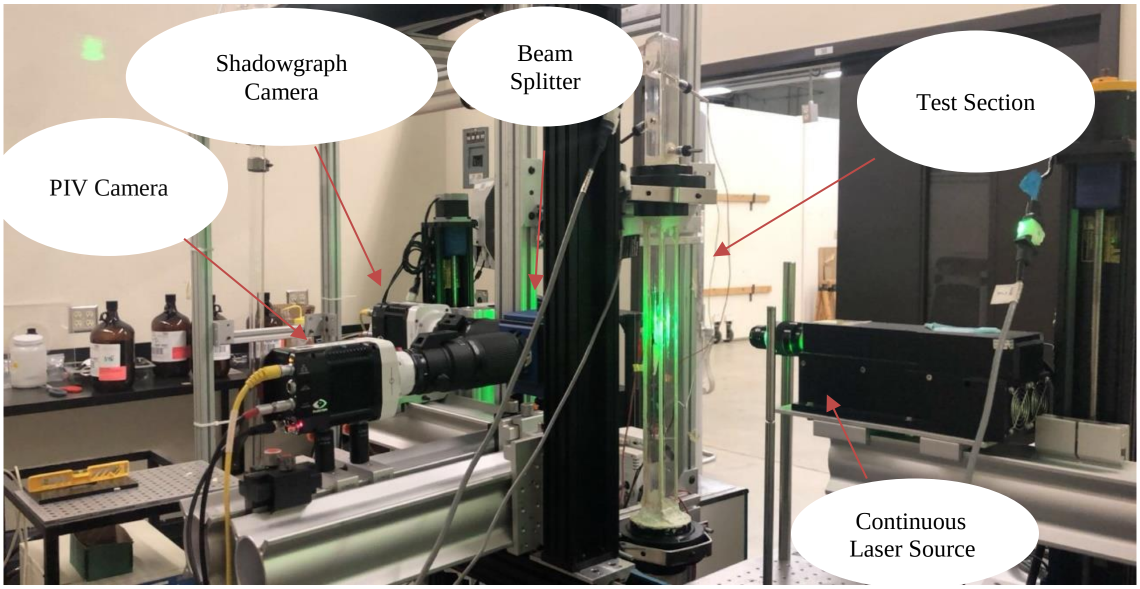

Figure 3.2: The PIV experimental setup without LED Back light.

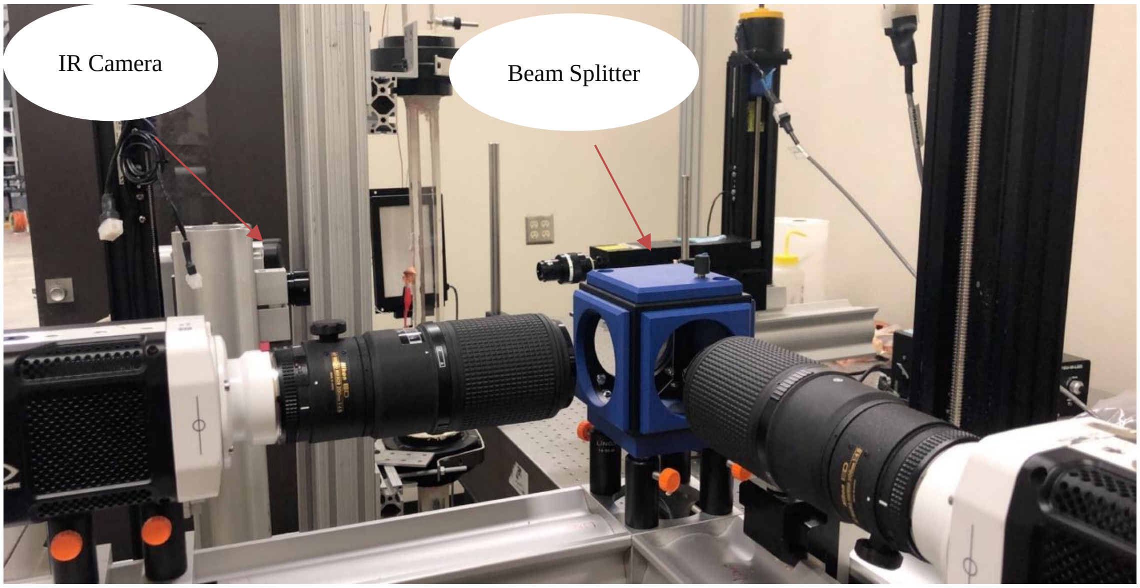

Figure 3.3: A closer look at the high speed cameras and the beam splitter on a 2D traverse.

Figure 3.4: The PIV facility with LED back light on (left) and a back-view of the test section (right).

Figure 3.5: The external pulse generator (left) and the continuous laser (λ= 532 nm, 10W).

Table 3.2: Experimental Instruments.

Instrument	Parameter	Model	Range	Tolerance
Chilling Unit	Water bath temperature control	RTE-221	25 ºC to 150 ºC	± 0.01 ºC
Thermocouples	Liquid temperature measurement	T-type	-270 to 370 ºC	± 0.75%
Flow meter	Liquid flow rate reading	Promass 83F08	0 to 18000 kg/h	±0.10%
Liquid circulating pump	Run liquid within the loop	ASTRO 290ss	0 to 64 USgpm	N/A
Sorensen	Power supply to the heater	XHR 600-1.7	0 to 600 V 0 to 1.7 A	+0.35% +0.1%
High speed camera	High speed image recording	Phantom R311	1280 X 800 pixel (3200 fps)	20 ns time resolution

3.4.2 Experimental Images

The experimentally acquired images can depend on the camera configurations and the setup. The side view configuration, in this work, is designed to provide detailed liquid velocity information near the bubble's nucleation sites and to obtain insights on the liquid velocity development along the bubbles' sliding distance. The PIV images are captured using the high speed camera with a straight view at the measurements section. The shadowgraph images are obtained from the other camera looking at a 90º angle from the measurement section and through the beam splitter. The LED back light is arranged to directly illuminate the shadowgraph camera and obtain a clear bubble's dynamics images. The viewing area (20.1 x 8 mm^2) of both cameras are adjusted and made similar to achieve the same view, which allows obtaining simultaneous image recording.

An example of the simultaneous PIV (left) and shadowgraph (right) measurements are provided below in Figure 3.6. The PIV image is obtained with the laser light illumination, which is used to provide information about the liquid velocity only. It’s worth mentioning that this image is filtered with a high pass filter, which helps reduce the background noise and allows a more accurate liquid velocity measurements. The shadowgraph image is obtained with LED illumination, which is used to provide the bubble’s dynamics. As shown in the shadowgraph image, the bubble’s dynamics are captured along the entire sliding distance from inception (at the nucleation sites) to detachment at top end of the image.

By combining the information from the PIV and shadowgraph images, a more faithful liquid velocity measurements are achieved.

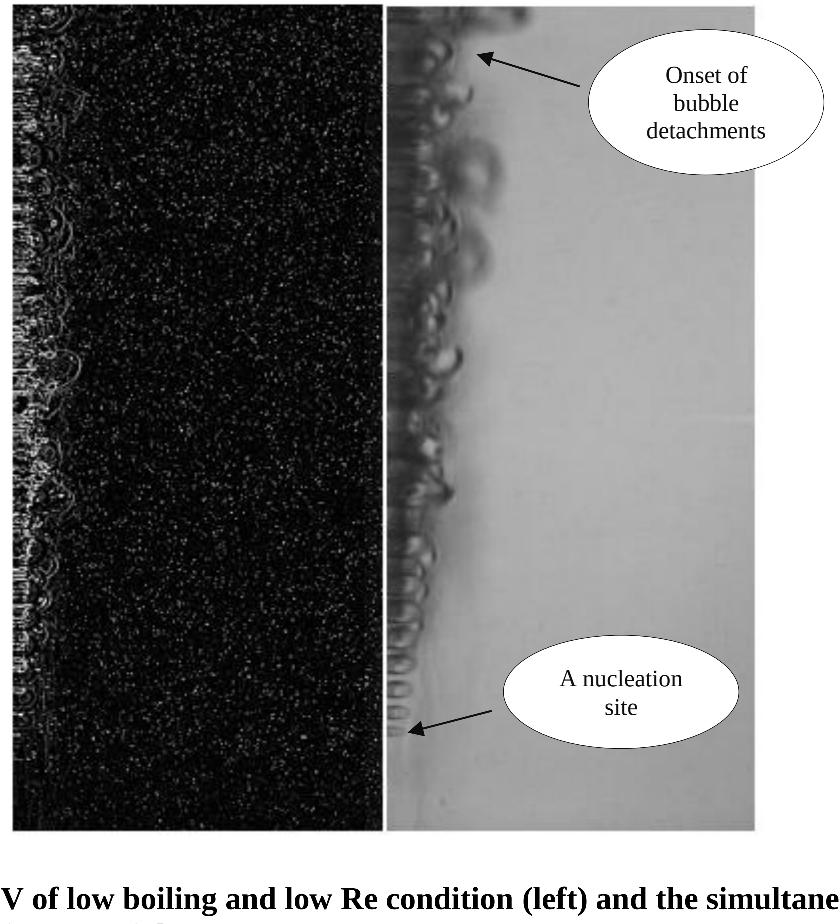

Figure 3.6: PIV of low boiling and low Re condition (left) and the simultaneous shadowgraph images (right).

The bubble’s dynamic images from the shadowgraph are essentially used to remove the bubbles and their laser reflections from the PIV images. In order to achieve this job, dynamic bubble binary masks are created using a “convert to mask” feature in ImageJ (which is a Java based image processing and analysis software). This feature allows to convert the shadowgraph images to binary images (black and white). A stack of shadowgraph images are first loaded into ImageJ. The images’ brightness is then adjusted properly to create enough contrast between bubbles (black) and the background (white) for a two phase discrimination. When a proper discrimination is created between the bubbles and liquid regions, the dynamic mask is applied to all images in the stack. The dynamic bubble mask images are utilized to obtain a cleaner version of the PIV images in which the bubbles and their laser reflections are sufficiently removed. An example of the bubbles mask (right) and a masked PIV (left) images are provided in Figure 3.7.

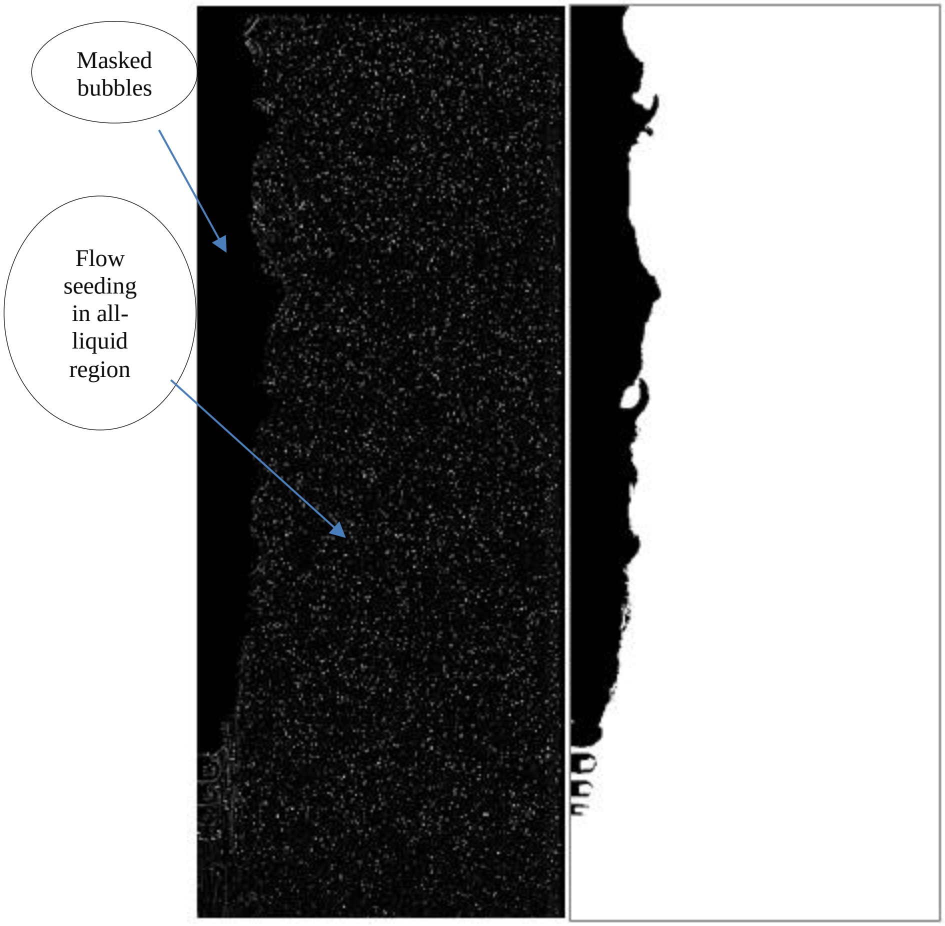

Figure 3.7: Masked PIV (left) and binary mask images (right).

A similar procedure can be done to obtain only bubbles information from the PIV images. Using the binary bubble images, the all-liquid region is removed from the PIV images in which only signals from the bubble regions are present. These images are used later to track the bubble motions and estimate their velocities. An example of the PIV images with only-bubble regions is provided in Figure 3.8. In this image, it is shown that the flow seeding particles in all-liquid region are completely removed, and only the signals from sliding bubbles are present.

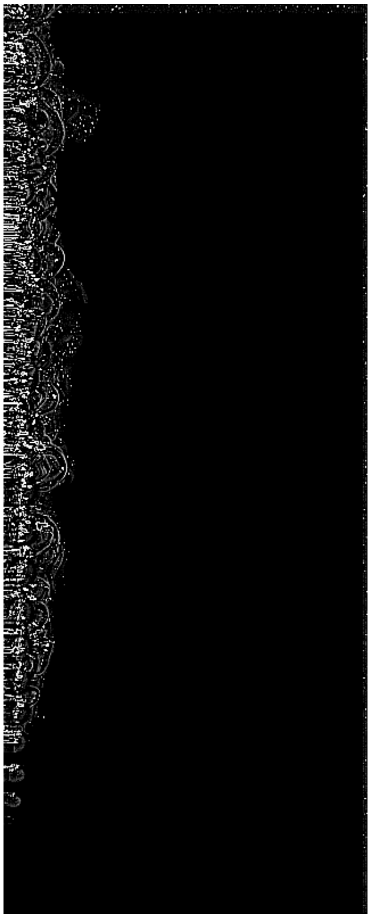

Figure 3.8: Masked background for bubbles tracking.

IR camera images obtained for this condition (low boiling and low Re) are provided in Figure 3.9. The liquid temperature distribution at nucleation sites and along the heated wall can be observed in the figure below. An ellipsoidal probe is marked at a nucleation site located near the right end of the test section and the closet possible to the side-view visualization system where PIV and shadowgraph images are taken. The liquid temperature profile is obtained at the probe area in which the liquid temperature at the nucleation site and around it appear to be fluctuating between 30.1 and 31.4 ^{o}C. This temperature trend is expected due to the fact that the saturation temperature of the working fluid is between 32 and 34 ºC. However, at the nucleation site, the liquid temperature values are expected to be lower due to a heat removal occurs in the boiling process. Except in some hot spots, the temperature distribution near the heated surface appear to be in between 29.1 and 31.9 ºC. Those hot spots pertain to the silver electrode (anode and cathode) which are connected to the heated surface through a copper sheet responsible for power supply. Other bright spots are believed to be due to some noisy locations caused by impurities on the surface of the heater.

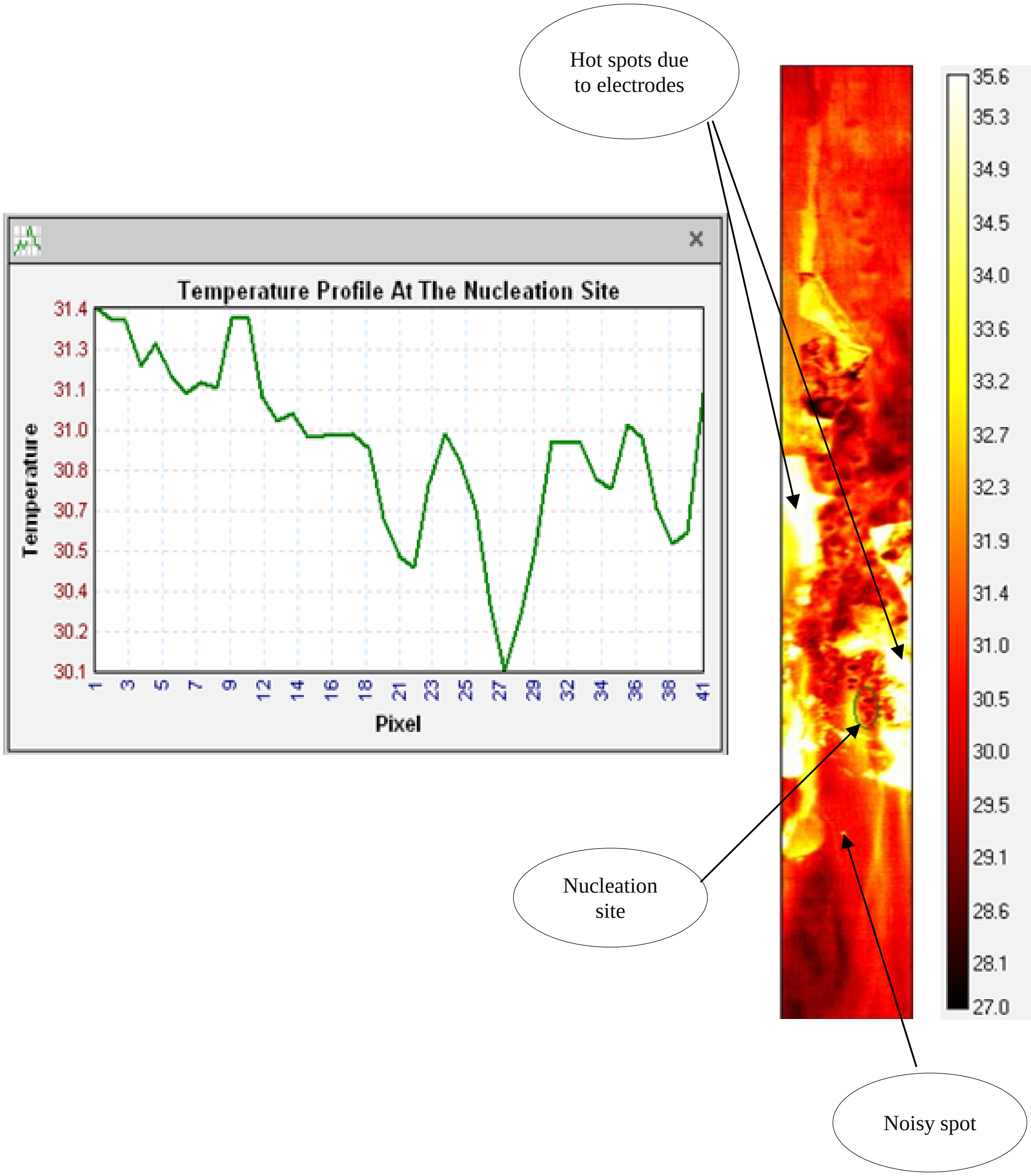

Figure 3.9: IR image for low boiling and low Re condition (left) and the liquid temperature profile at the nucleation site (right).

3.4.3 Experimental Image Processing

The PIV and binary dynamic mask images are loaded into PRANA for processing (PRANA PIV Manual, 2011). PRANA is an open-source GUI-driven program for calculating velocity fields using PIV. This software employs the robust phase correlation (RPC) processor which reduces bias error and peak locking in the presence of high shear and rotational motion (Nguyen et al. 2018). The technique used here allows to reduce the dominance of the noise fluctuating peaks over the displacement peak. This can be accomplished by employing multiple passes that are used in an interactive manner to increase the accuracy of the displacement peak estimation. On each PIV image, the integration window size, the resolution, and the application of validation technique can be altered for each pass. The validation technique is used here to check each velocity vector individually by comparing its magnitude with that of the neighboring vector.
For the purpose of this study, 3 passes are employed with varying window sizes being 32 x 16 pix for the first pass, and 16 x 8 pix for the second and third passes. The binary dynamic mask is applied to the software to remove the bubbles' information from the processed liquid velocity fields and reduce undesired noise that may lead to velocity estimation errors. Figure 3.10 below shows a snapshot at the user friendly PRANA's interface for visual demonstration.

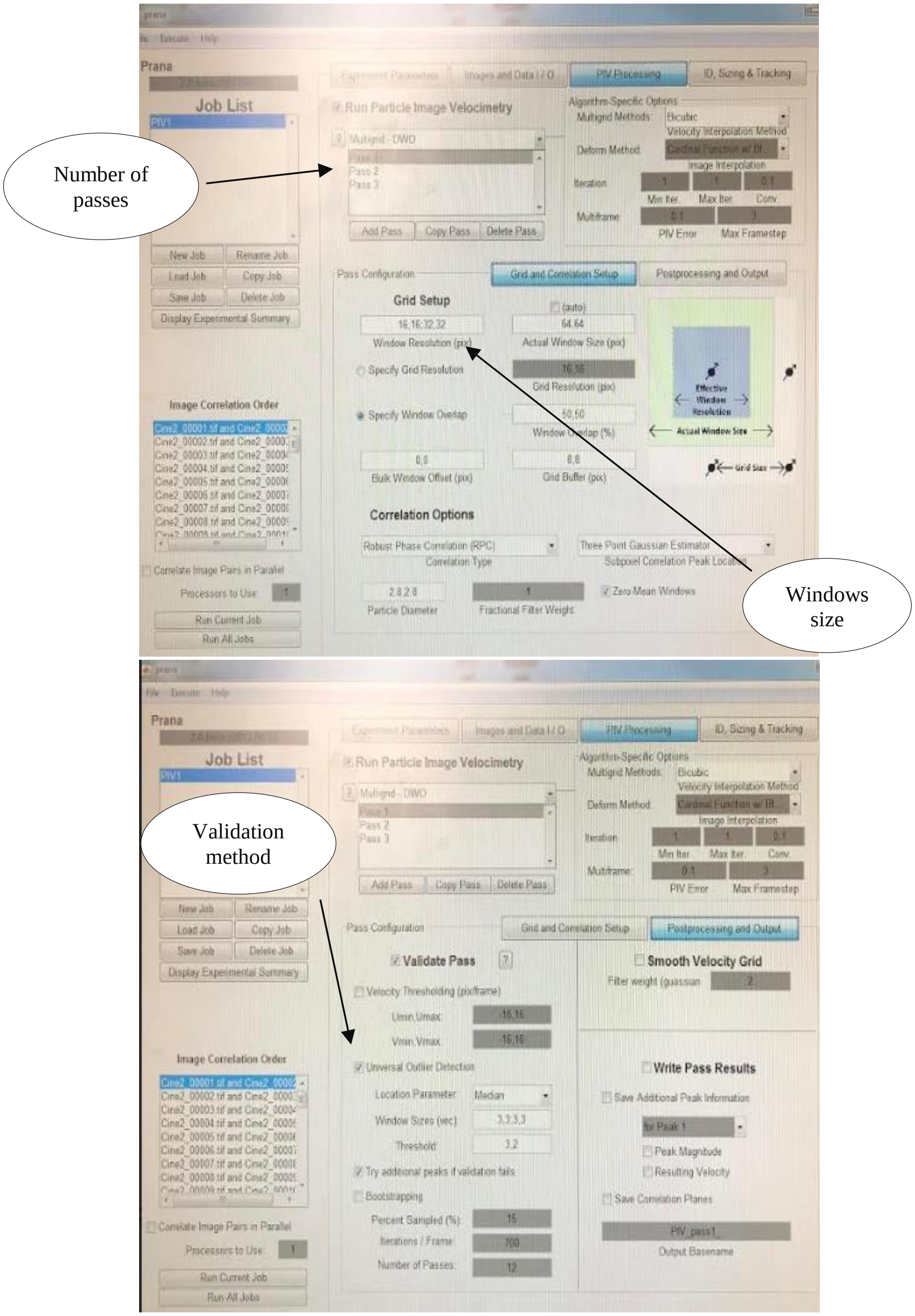

Multigrid Methods: Bicubic

Velocity Interpolation Method

Deform Method: Cardinal Function w/ Bl...

Image Interpolation

Iteration: 1 (Min Iter.), 1 (Max Iter.), 0.1 (Conv.)

Multiframe: 0.1 (PIV Error), 3 (Max Framestep)

☐ (auto)

Window Resolution (pix): 16,16;32,32

Actual Window Size (pix): 64,64

○ Specify Grid Resolution

Grid Resolution (pix): 16,16

● Specify Window Overlap

Window Overlap (%): 50,50

Bulk Window Offset (pix): 0,0

Grid Buffer (pix): 8,8

Correlation Type: Robust Phase Correlation (RPC)

Subpixel Correlation Peak Location: Three Point Gaussian Estimator

Particle Diameter: 2.8,2.8

Fractional Filter Weight: 1

☑ Zero-Mean Windows

☐ Correlate Image Pairs in Parallel

Processors to Use: 1

☑ Validate Pass

☐ Velocity Thresholding (pix/frame)

Umin,Umax: -16,16

Vmin,Vmax: -16,16

☑ Universal Outlier Detection

Location Parameter: Median

Window Sizes (vec): 3,3;3,3

Threshold: 3,2

☑ Try additional peaks if validation fails

☐ Bootstrapping

Percent Sampled (%): 15

Iterations / Frame: 700

Number of Passes: 12

☐ Smooth Velocity Grid

Filter weight (guassian: 2

☐ Write Pass Results

☐ Save Additional Peak Information

for Peak 1

☐ Peak Magnitude

☐ Resulting Velocity

☐ Save Correlation Planes

Output Basename: PIV_pass1_

Figure 3.10: PRANA user-interface.

3.5 Experimental Results And Discussion

3.5.1 Bubbles Layer Dynamics

3.5.1.1 Bubbles Layer Thickness

In this experiment, the bubbles are born at multiple nucleation sites before then slide upward along the heater merging together and gaining size and momentum. It is assumed that this behavior allows the bubbles to form a layer acts as a solid wall moving with a speed that is proportional to the average terminal velocity of bubbles contained within that layer.

The bubbles layer thickness as a function of the wall heat flux with two different flow rates is primarily estimated from the time-averaged binary dynamic mask images (obtained from the high speed shadowgraph experimental images) and the time-averaged liquid velocity fields. In this context, the masked zero velocity regions in the time-averaged liquid velocity fields are essentially considered the areas occupied with bubbles only. Information on those regions are defined and plotted against the test channel dimensions. This allows to measure the spatial thickness of the solid moving wall (the assumed bubbles layer) in axial and redial direction.

Figure 3.11 below shows the bubbles layer thickness for the low and high boiling conditions with low Re. It is important to note that the outer edge of bubbles layer is defined here at the radial location in the fluid where the vapor residence time fraction becomes essentially zero. It is apparent that the boiling layer of the high heat flux is longer and thicker as the bubbles in this condition start nucleating and forming their moving layer at a lower axial distance. The most probable boiling layer thickness in the low heat flux conditions ranges between 0.21 and 1.03 mm, whereas in the high heat flux conditions it ranges between 0.41 and 1.4 mm.

Similar trend can be observed in Figure 3.12 with the high Re. However, the bubbles layer formation, especially in the high boiling case, appear to start at a higher axial location than in the low Re. This observation is expected as the higher flow rate, usually, tend to suppress some of the nucleation sites at the bottom end of the test channel.

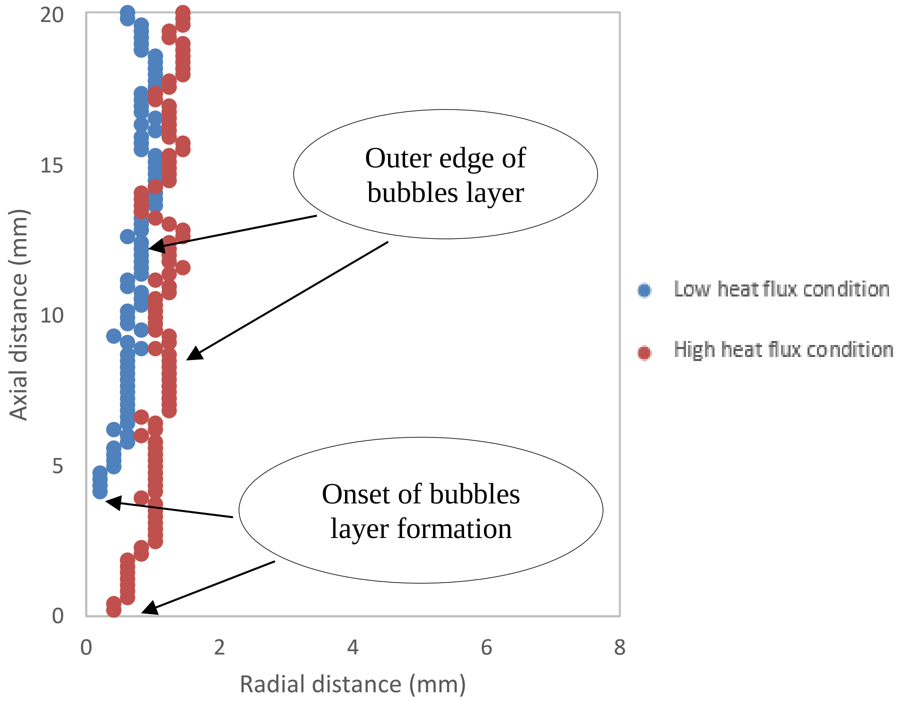

Figure 3.11: Bubble layer thickness as a function of the wall heat flux for low Re (8121).

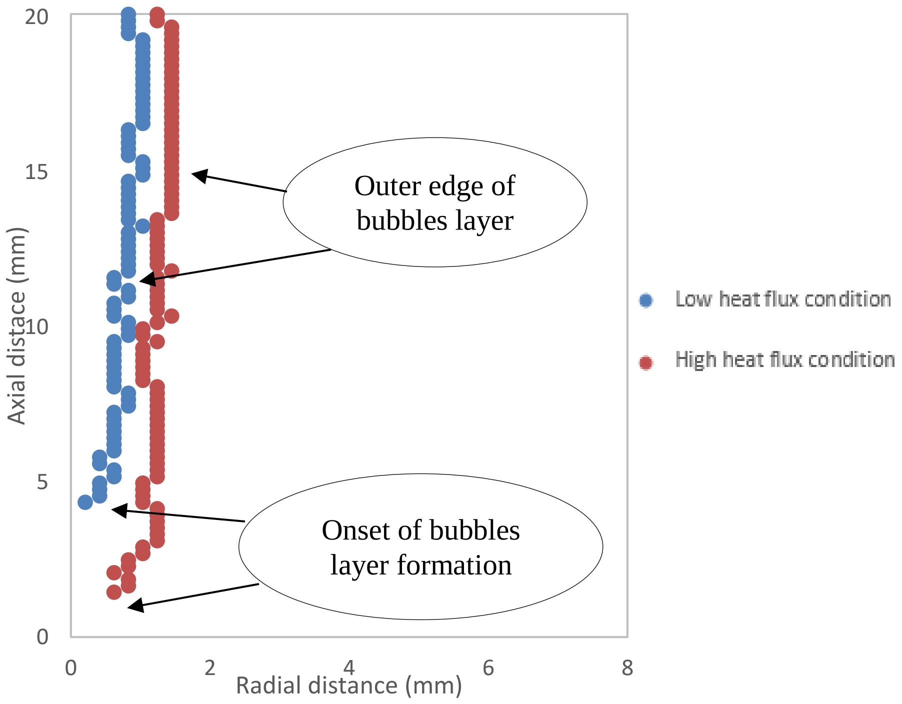

Figure 3.12: Bubble layer thickness as a function of the wall heat flux for high Re (20523).

The bubble layer thickness of the same boiling level at different flow rates are given below in Figures 3.13 and 14 for comparison. In low boiling conditions, the thickness of two layers appear comparable and no much difference in thickness. However, the low flow rate conditions appear to slightly spread more uniformly covering wider axial distance. The possible reason for that is at lower flow rates, more bubbles can form and develop in bigger sizes covering wider radial region. This, as a result, give rise to the bubbles layer being thicker in size.

In the high boiling conditions, however, the low flow rate condition appear to start at lower axial distance, for the same reason mentioned above, and also the spread looks more uniform while developing axially.

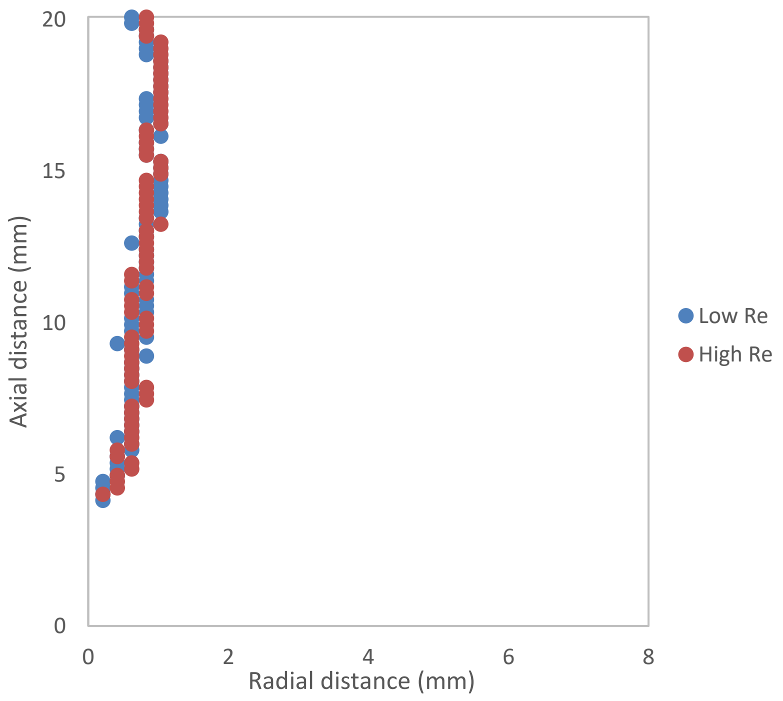

Figure 3.13: Bubble layer thickness in the low boiling conditions (16.4 kw/m^2) for low and high Re.

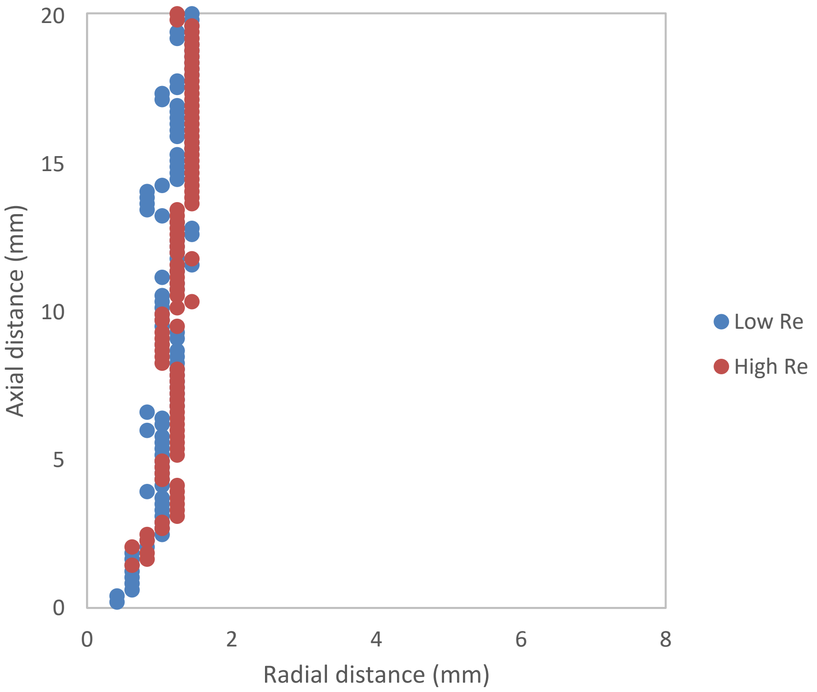

Figure 3.14: Bubble layer thickness in high boiling conditions (42.8 kw/m^2) for low and high Re.

The time-averaged masking information are also utilized to estimate the bubbles' time residence, which is defined here as the length of time the bubbles reside in the assumed boiling layer. The estimated boiling thickness, at each axial location, is divided by the entire thickness of test channel (8 mm) to obtained the thickness fraction occupied by the bubbles layer only (bubbles layer fraction). The bubbles layer fraction as a function of the wall heat flux for the low and high Re are provided in Figure 3.15 and 16, respectively. The obtained trends shows clearly a higher bubble layer fraction with higher heat flux. This behavior, of course, is expected as the bubbles layer fraction here is proportional to the bubbles layer thickness proposed in this study.

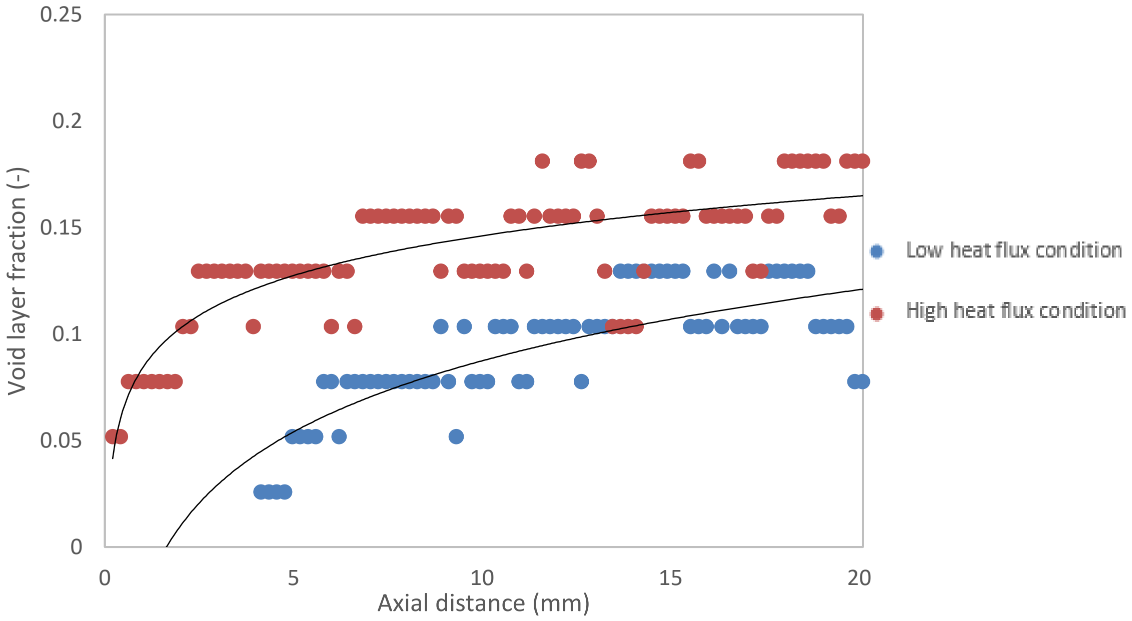

Figure 3.15: Void layer fraction as a function of wall heat flux for low Re (8121).

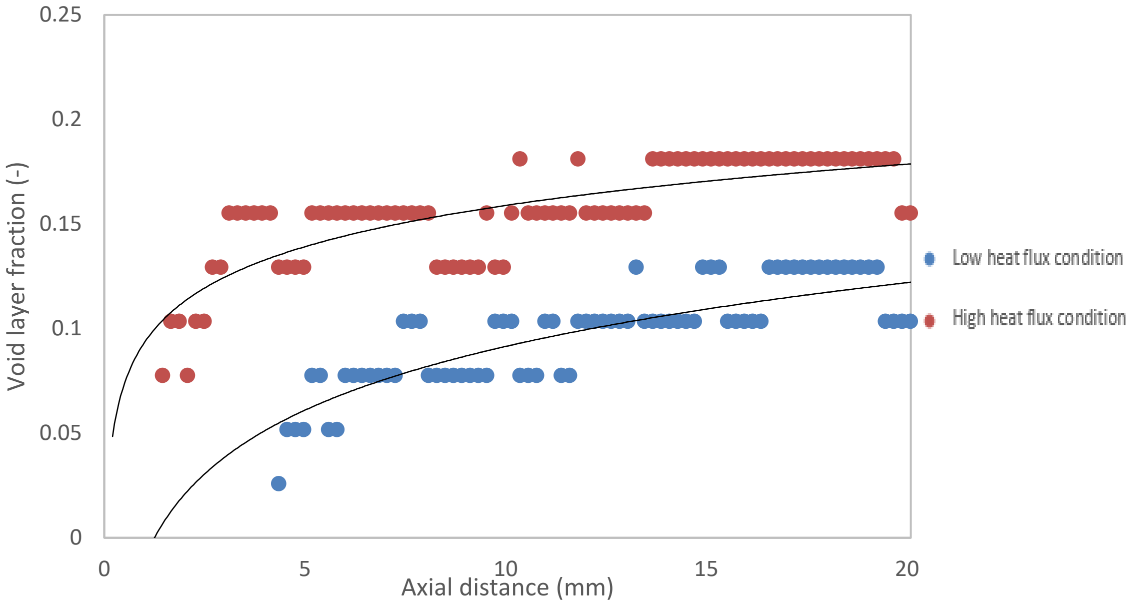

Figure 3.16: Void layer fraction as a function of wall heat flux for high Re (20523)

3.5.1.2 Bubbles Layer Velocity

Since the bubbles layer moves along the heater as a solid wall with the speed that is proportional to the average terminal velocity of the bubbles forming this wall, estimation of the bubbles layer at different axial locations may be done in two different approaches. The first approach is to use the PIV images to track the laser illuminated objects within the bubbles forming the layer at each axial location. These tracked objects are assumed to shape the bubbles domain and move at the bubbles velocities. The average bubbles velocities measured across the bubbles layer thickness are assumed to provide a good approximation to the bubbles layer velocity along the heater. Figure 3.8, provided in previous section, shows an example of the laser illumined PIV image obtained experimentally and used here to approximate the average bubbles velocity within the solid moving bubbles layer. The liquid flow region in the PIV image is masked and only the bubbles information (given small illuminated objects) are tracked within the given layer.

The processed PIV images for the bubbles layer velocities are given below in Figures 3.17-20. Figure 3.17 (right) shows the approximated time-averaged bubbles layer velocity distribution for low heat flux and low Re condition. Figure 3.17 (left) provides the average bubbles layer velocity obtained and marked with a short horizontal line at selected axial locations (6, 10, 14, 18mm). The velocity values at those axial locations are shown to vary considerably. It is apparent that the bubbles layer accelerates with the axial distance. This acceleration, as expected, signifies the gain of momentum while sliding upward. The rate of acceleration is, however, dependent on the controlling parameters considered here; namely, the wall heat flux and the flow rate. It is shown in Figure 3.17 (left) that bubbles layer velocity increases from about 0.09 m/s to approximately 0.19 m/s between 6 and 10mm. This rate of increase is seen to decrease as the bubbles layer apparently reaches its highest thickness in between 10 and 14mm gaining a velocity of 0.22 m/s (at 14 mm) on average. The bubbles velocity is obtained to reach its highest value of 0.24 m/s at 18mm axially.

The same trend of velocity increase is seen in Figure 3.18 but at slightly different rates. The bubbles layer is obtained to start at a slower velocities (about 0.07 m/s at 6 mm) than those obtained in previous condition. It is suggested that, at higher flow rates, nucleation site suppressions occur at lower axial locations, and so bubbles are born at less number of locations and develop in size at smaller rates. Due to possibly higher flow rate, the bubbles layer seem to gain slightly higher velocities at higher locations. The velocity is seen to increase to about 0.22 m/s at 10 mm and to 0.236 and 0.24 m/s at 14 and 18 mm, respectively.

Figure 3.19 and 3.20 exhibit the bubbles layer velocity for high boiling conditions, low and high Re, respectively. Due to the bigger bubble sizes and thicker bubbles layers induced by the higher heating levels, the bubbles layers are seen to slide at higher velocity values. In the low flow case (Figure 3.19), bubbles layer shows a velocity value of about 0.21 m/s at 6 mm. It continues to increase with varying rates to reach 0.27, 0.31, and 3.4 m/s at 10, 14, and 18mm, respectively. With due cation, in the view of the uncertainties involved in this approach, it is suggested that the rate of increase in velocity start to slow down when the bubbles layer appear to reach its highest thickness and then begin to deform. This may be seen between 10 around 14 mm. The velocity, then, appears to continue growing but at a lower rate.

Figure 3.20 shows the case for high flow rate. The bubbles layer velocity here appears to be higher everywhere along the heater. The bubbles inception and growth rates appear to be high enough that the impact of nucleation site suppression on the lower axial bubble velocity profiles is not noticeable. The bubbles layer is shown to increase with the same trend as seen in the previous case but with higher velocity values. The rate of increase between 6 and 10 mm is seen to be higher than the one between 10 and 14mm and between 14 and 18mm.

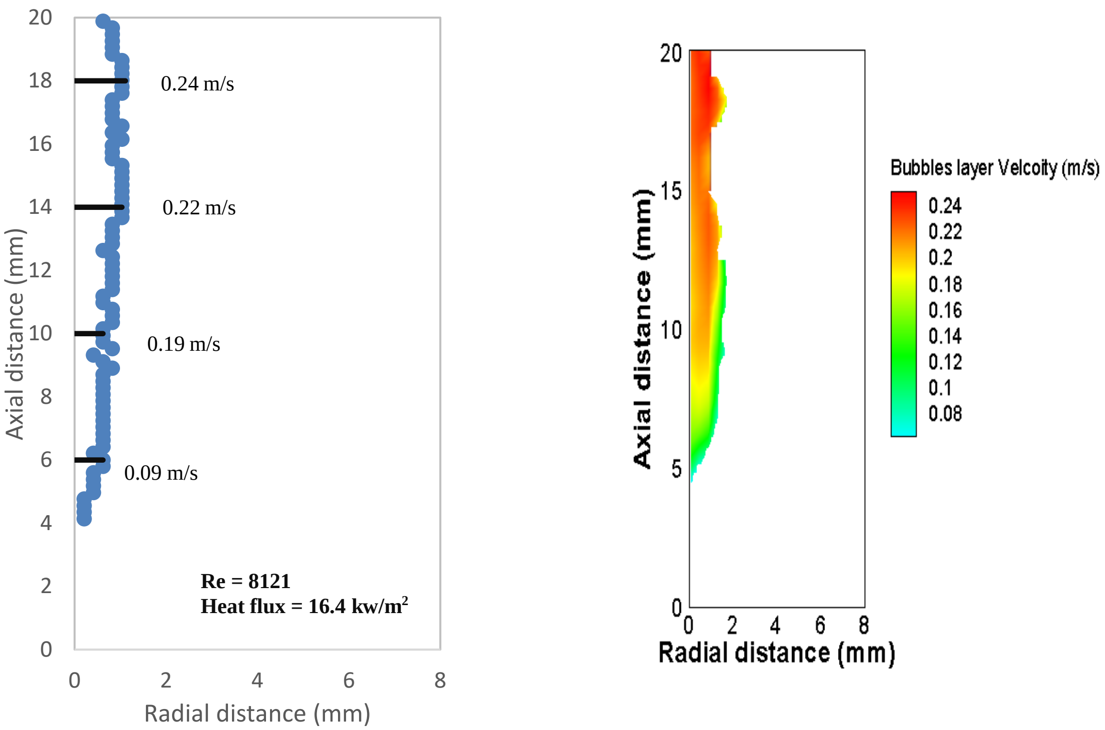

Figure 3.17: Average of bubbles' layer velocity at certain axial locations (left) processed time-average velocity image for low boiling (right) and low Re.

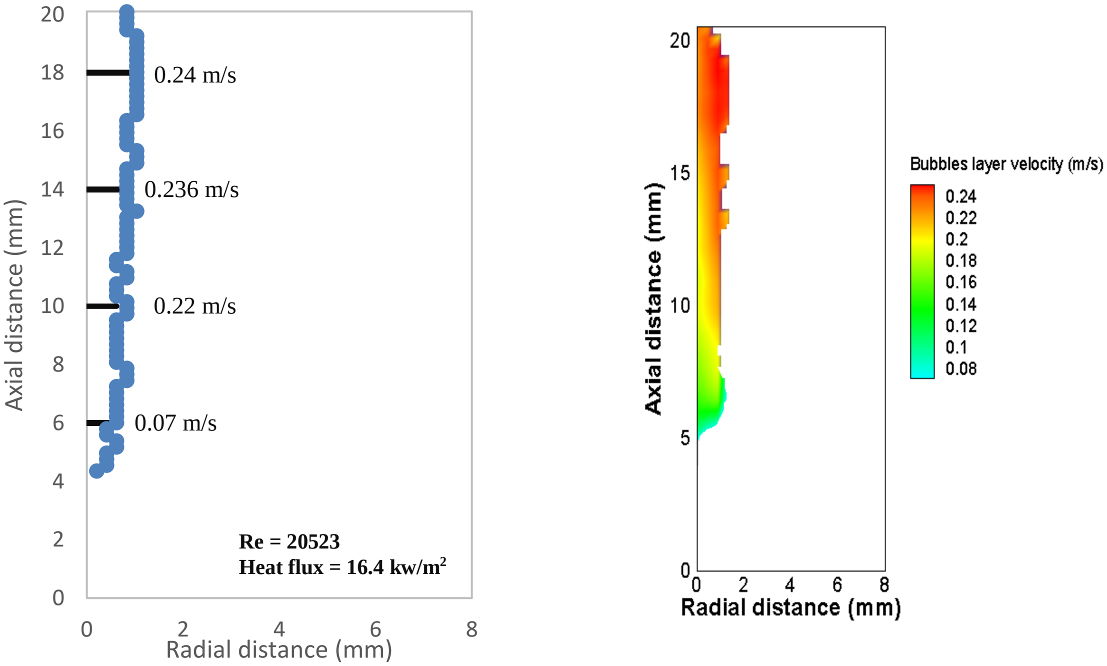

Figure 3.18: : Average of bubbles' layer velocity at certain axial locations (left) processed time-average velocity image for low boiling (right) and high Re.

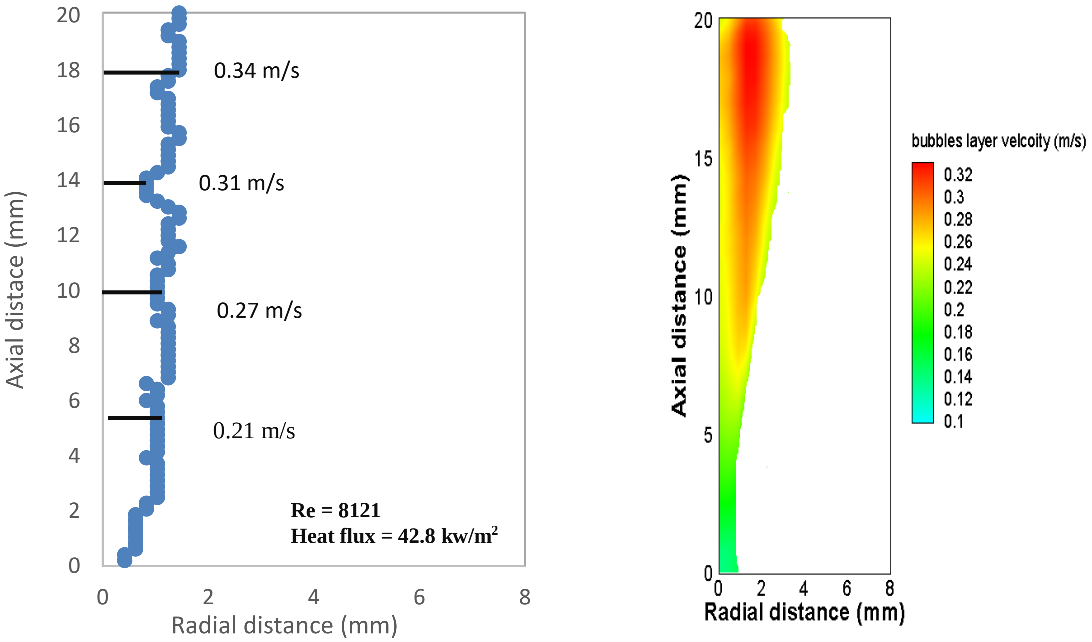

Figure 3.19: Average of bubbles' layer velocity at certain axial locations (left) processed time-average velocity image for high boiling (right) and low Re.

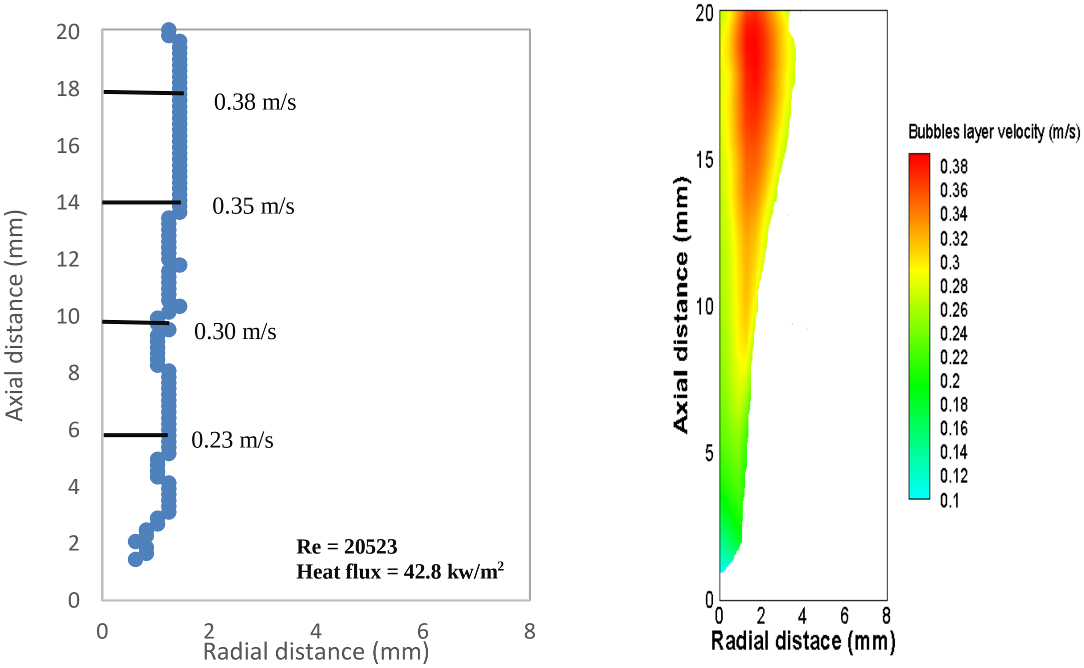

Figure 3.20: Average of bubbles' layer velocity at certain axial locations (left) processed time-average velocity image for high boiling (right) and high Re.

The second approach to measure the bubbles layer velocity is done semi-automatically in which five different individual bubbles were tracked as they slide along the heater in each condition. The shadowgraph images are adjusted in ImageJ to obtain sufficient contrast between the tracked bubble (dark) and the background (white).

A single particle tracking (SPT) feature in ImageJ is utilized in which information regarding the bubbles centroid coordinates in 2D is extracted over time. A point probe is used to locate the bubble's centroid, and then it is tracked from the start of the sliding distance to the marked line probes. Those line probes represent the axial distance where bubbles layer velocity is measured. With each frame, the point probe is moved with the bubble's centroid and the location coordinates are recorded in X, Y. When the point probe reaches the horizontal line, the sliding time (in frames/sec) and distance (in pixel) are calculated to estimate the velocity at each probe. Figure 3.21 shows an example of the adjusted shadowgraph image for low boiling condition and low Re. The average velocity of five bubbles passing through the line probes of each condition is obtained and provided below in table 3.3. The estimated velocities here are shown to be within the range of ± 0.05 m/s of the values obtained in the previous method. The discrepancy in the velocity values in these two approaches is attributed to the bubble tracking mechanisms in each method. The first method tracks the signal emerging from one bubble or more bubbles merging together and contained in a one integration window. This probably appear to provide lower velocities (in average) as it takes into account the average values of one or more bubbles deforming, coalescing and sliding together. The second method, however, is implemented by tracking consecutive individual bubbles sliding. And so, the velocity estimation using this method considers only information from one bubble at a time, which appear to provide higher values in velocity especially at highest axial locations.

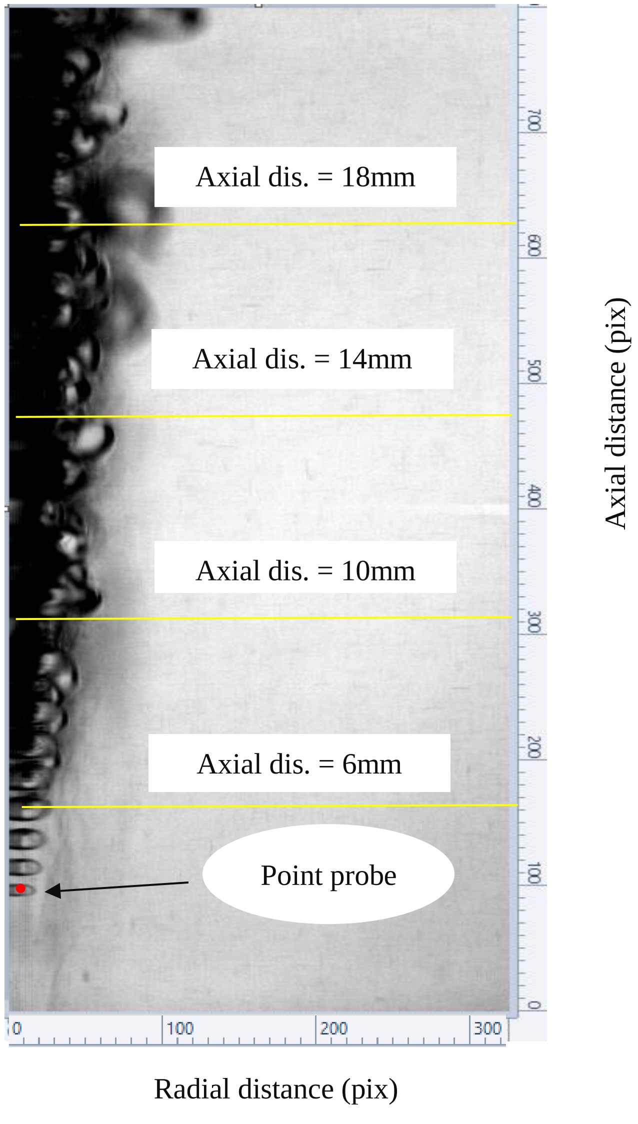

Figure 3.21: A raw image of low boiling and low Re condition used for velocity estimation.

TABLE 3.3: Estimated bubble layer velocity of the considered conditions.

Axial location	Low Boiling Low Re	Low Boiling High Re	High Boiling Low Re	High Boiling High Re
6mm	0.12 m/s	0.05 m/s	0.17 m/s	0.26 m/s
10mm	0.15 m/s	0.26 m/s	0.27 m/s	0.32 m/s
14mm	0.18 m/s	0.28 m/s	0.33 m/s	0.34 m/s
18mm	0.21 m/s	0.3 m/s	0.38 m/s	0.42 m/s

3.5.2 Liquid Turbulence Statistics

3.5.2.1 Average Liquid Velocity for All Conditions

The analysis of PIV measurements provided information on the liquid velocity profiles near the heated surfaces. The time-resolved instantaneous velocity fields for the conditions of interest show the development of the velocity boundary layer along the bubbles sliding distance. As expected, wall heating has brought significant changes to the distribution of velocity fields especially at near-wall regions. Some of these changes are general trends and observed in previous studies (Estrada-Perez et al., 2010; Hassan et al., 2012; Roy et al., 1993; Zarate et al., 2000). All results presented in this section are shown in actual radial distances and non-dimensional ones. First, the non-dimensional distance is obtained as the following. In the wall coordinate system, a characteristic velocity is required to obtain non-dimensional variables. The characteristic velocity used here is the friction velocity ($u^* = \sqrt{\tau_w/\rho}$). The friction velocity can be estimated from total stress profiles obtained in near-wall regions, at heated single phase conditions, to determine τ_w. The non-dimensional radial distance ($x^+ = xu^*/\nu$) is then computed and plotted versus the liquid velocities for all conditions.

Figure 3.22 shows the time-averaged velocity fields for the heated single phase conditions with low Re (left) and high Re (right). These conditions were obtained with the heat flux level just below the boiling threshold. The heated wall here is shown to be on the left side of the measurement section. The color bar indicates the velocity magnitude given in m/s. Velocity vectors are displayed to indicate the upward direction of the flow. The test section dimensions are given by millimeters (mm), with about 20 mm in length axially and 8 mm in width radially. The axial liquid velocity measurements in the radial direction are taken just near the heated wall and across toward the center of the test section at four different locations along the axial direction, namely, 6 mm, 10 mm, 14mm, 18mm, from the inlet (marked in Figure 3.22).

Velocity values at those location were extracted and plotted in Figure 3.23. The axial velocity plot in Figure 3.23 demonstrates the velocity boundary layers as they develop in the radial direction. The given velocity profiles appear to increase as moving away from the heated wall toward the center of channel (at around 8 mm). Measurements at those locations presents fully developed flow statistical characteristics. Therefore, they were selected as suitable measurement areas for boiling experimental investigations.

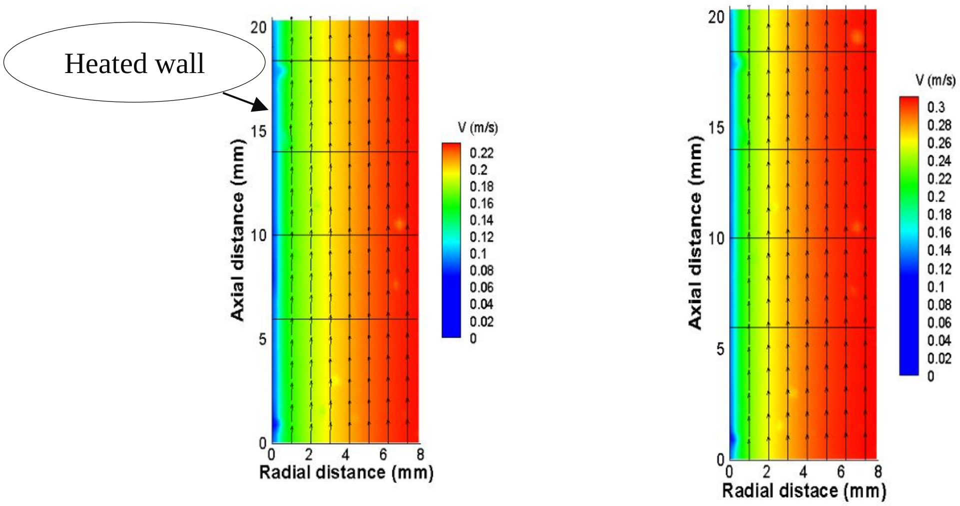

Figure 3.22: Time-averaged liquid velocity fields for the heated single phase conditions with low Re (left) and high Re (right).

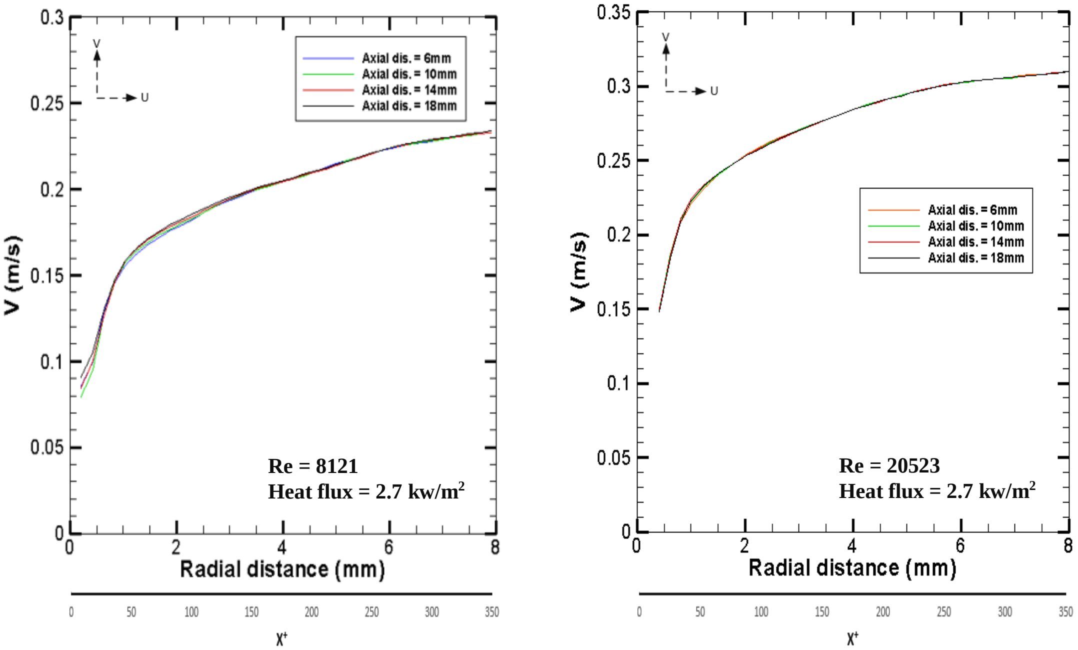

Figure 3.23: Average liquid velocity profiles for four different axial probes in the heated single phase conditions with low Re (left) and high Re (right).

Figure 3.24 shows the time-averaged velocity field for the low Re and low boiling case. In this condition, the onset of bubbles layer is shown to happen at approximately 4.1 mm in the axial direction, whereas detachment takes place at about 20.1 mm axially. The bubbles sliding distance is shown to be in the range of 15.1 mm. The bubbles layer thickness is seen also to be increasing as the bubbles continue to grow while sliding until they reach their maximum size at around 15 mm axially, where bubble layer starts to level off. The axial liquid velocity measurements in the radial direction are taken just near the bubble region and across toward the center of the test section at four axial location mentioned above. Velocity values at those location are extracted and plotted in Figure 3.25. The axial velocity plot below shows the velocity boundary layers as they develop in the radial direction. For each of the axial location, the velocity profiles are shown to be increasing toward the center of the test section, where the flow velocity reaches the free stream values (just below 2.5 m/s) at around 8 mm. The velocity values are obtained to be growing sharply in high turbulent regions (between 1 and 1.5 mm radially) until around 2 mm, where it starts showing a slower rate of increase.

The axial shift in the velocity profiles signifies the growth in the bubble layer thickness from bubbles inception to detachment. The slight concomitant increase in the liquid velocity gradient with the distance from the onset of the bubbles layer is believed to be due to the increasing bubbles layer velocity along the sliding distance. The four profiles appear to intersect at a common location around 2.25 mm radially.

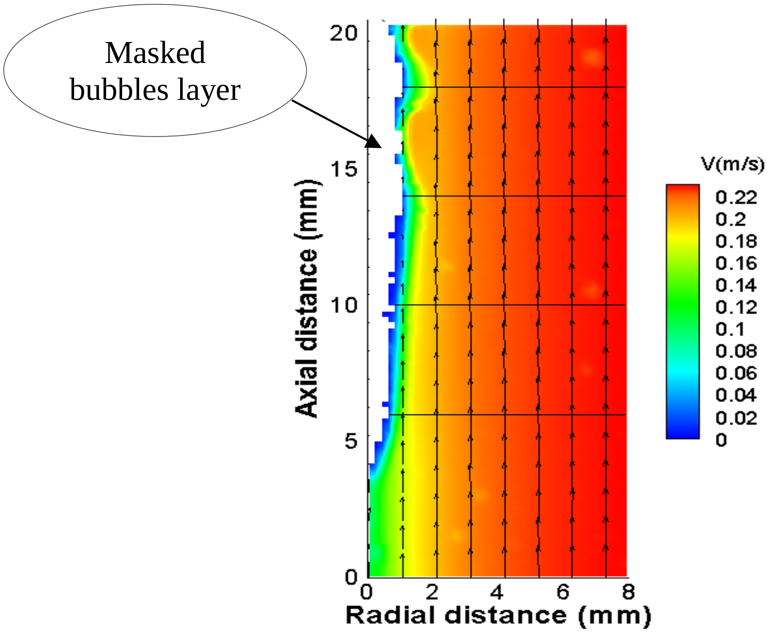

Figure 3.24: Time-averaged liquid velocity field for low boiling and low Re condition.

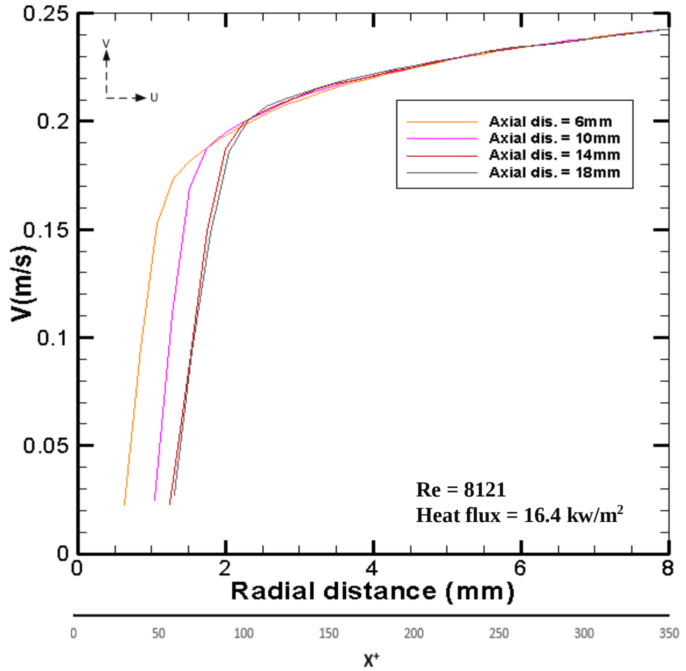

Figure 3.25: Average liquid velocity profiles for four different axial probes in low boiling and low Re condition.

Figure 3.26 shows the time-averaged velocity field for the low heat flux with higher flow rate (high Re). In this condition, the onset of the bubbles layer is seen to happen at slightly higher axial position (at approx. 4.2 mm) than that in the low Re case. The nucleation sites at lower locations appear to be suppressed by the higher flow rate. The bubbles sliding distance is, therefore, shown to be shorter (just below 15 mm). Similar to the previous case, velocity measurements are taken at the four probes given above and plotted in Figure 3.27.

In Figure 3.27, the velocity profiles are shown also to be increasing toward the center of the measurement section. Similarly, the velocity values are obtained to be growing largely in mixed liquid/bubbles region below 2 mm radially. The velocity, then, show a slower trend as it reaches the bulk liquid velocity value of approx. 0.32 (m/s). The axial shift in profiles here shows a less axial spread than those obtained in the lower flow rate condition. The possible reason for this trend is the style of development in bubble layers at different flow rates, which is discussed in the bubbles layer development section.

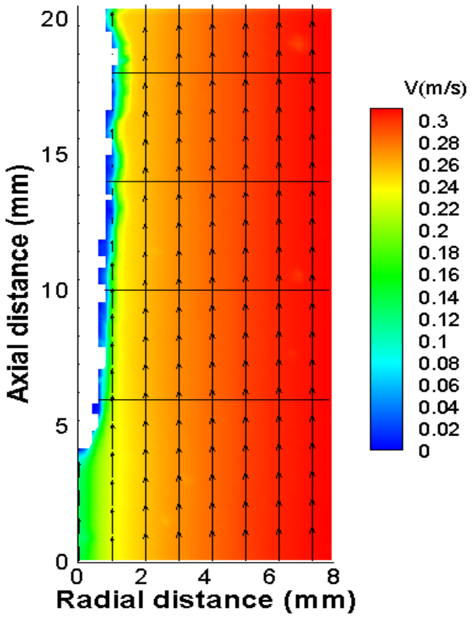

Figure 3.26: Time-averaged liquid velocity field for low boiling condition and high Re.

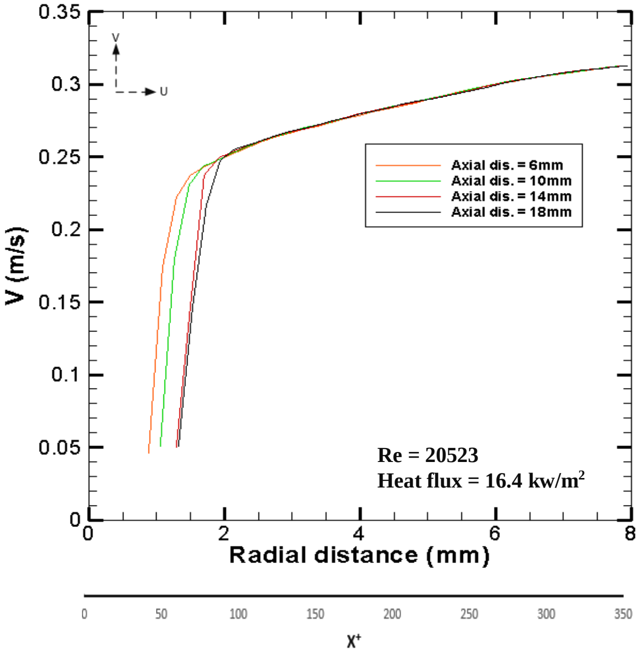

Figure 3.27: Average liquid velocity profiles for four different axial probes in low boiling case and high Re condition.

Figure 3.28 displays the time-averaged velocity field for higher boiling case with low Re case. The bubbles layer length and thickness, in this condition, are clearly larger than those in the lower heat flux conditions. The bubbles inception appear to happen just at the lowest bottom end of the heated surface. The bubbles layer grows in thickness as the bubbles from multi-nucleation sites continue to merge together and slide along the heater until they reach a detachment location at around 20.1 mm in the axial direction. The velocity measurements at locations of interest are taken here as well and plotted in Figure 3.29. Clearly, the higher heating into the liquid generates thicker bubbles layer moving at a higher velocity. This bubbles layer dynamic causes the velocity values to increase largely in high turbulent regions between 1.5 mm and 3 mm in the radial distance. The gradual concomitant increase in velocity profiles with the axial distance in regions close to heated wall is evidently shown at axial locations of 10mm, 14mm, and 18mm, where the highest peak of about 0.24 m/s is reached. The plot shows a clear shift in maximum velocity locations near the heated wall toward the center of channel. This shift in peaks locations is accompanied by a growth in peak sizes. The reason for this trend is believed to be due to the increasing bubbles layer thickness and velocity with upward axial distance. Moving away from the high turbulent region, velocity values starts dropping off at around 3 mm and merging together at around 5 mm, radially, to reach free stream velocity value of approx. 0.24 m/s.

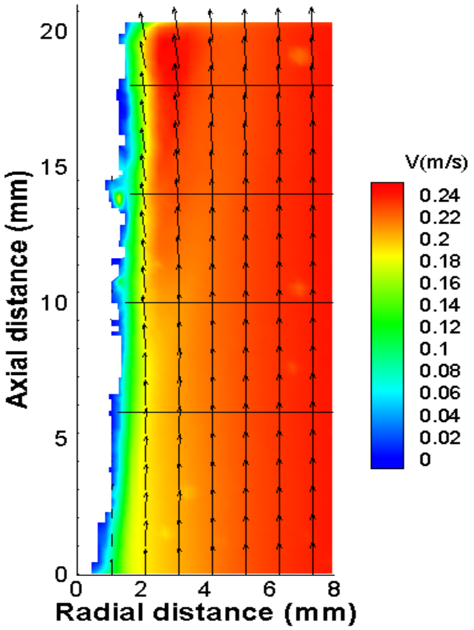

Figure 3.28: Time-averaged liquid velocity field for high boiling case and low Re condition.

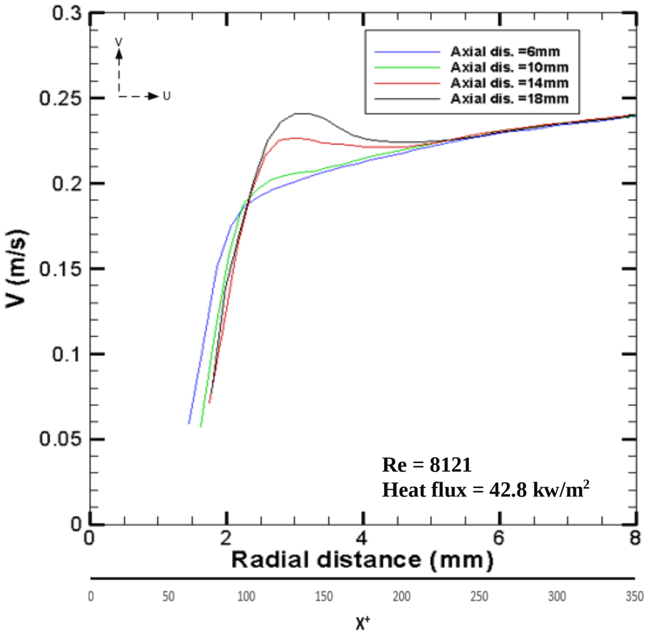

Figure 3.29: Average liquid velocity profiles for four different axial probes in high boiling case and low Re condition.

The time-averaged velocity field for the high boiling condition with higher Re is given below in Figure 3.30. The boiling layer is observed to start forming at a higher axial location (around 4.1 mm) as the higher flow rate appear to suppress the nucleation sites at lower locations. Similar trend can also be observed in the previous higher flow condition with lower heat flux. The formation of the bubbles layer is shown to follow a similar fashion seen in the previous high boiling case but with a slightly thinner boiling layer. The velocity profiles are obtained as well for this case and shown in Figure 3.31.

In Figure 3.31, it is clearly shown that the velocity profiles, with this Re, in regions near the wall as a function of heated surface show a less impact by the heating input. This can be observed with slower growing peaks (in regions between 1.5 mm and 2.9 mm) than those seen in the previous case. The maximum velocity magnitude near the wall is obtained to be around 0.29 m/s. Also, the shift is in velocity peaks toward the center of the channel is less noticeable here, especially at higher axial locations.

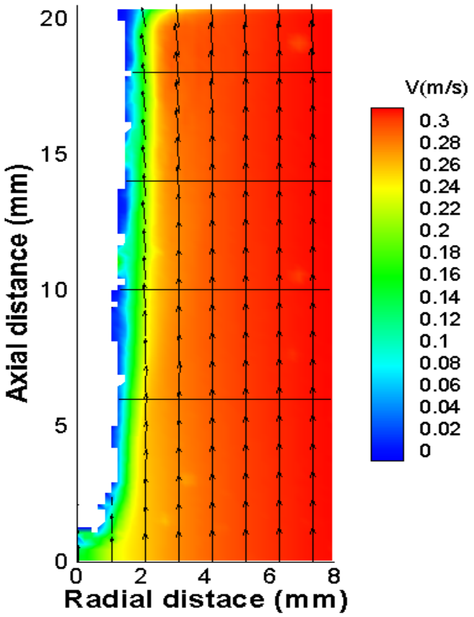

Figure 3.30: Time-averaged liquid velocity field for high boiling case and high Re condition.

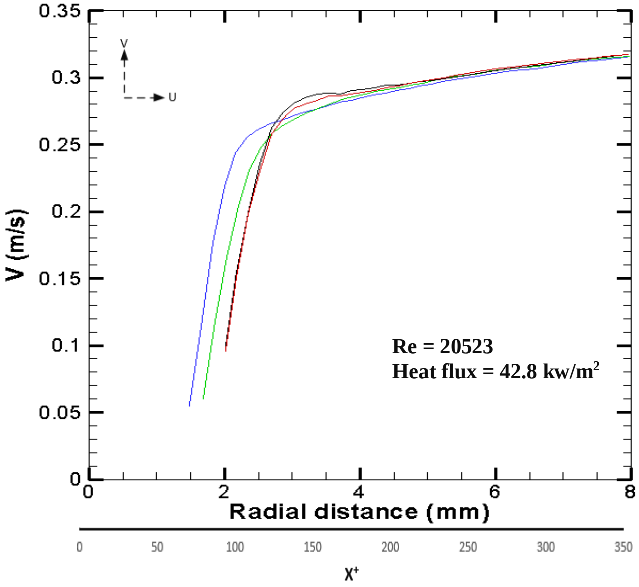

Figure 3.31: Average liquid velocity profiles for four different axial probes in high boiling case and high Re condition.

To better visualize the influence of the heat flux on the liquid phase behavior, conditions of the same flow rate with different heating level are plotted and shown below in Figures 3.32 and 3.33 for comparison. Figure 3.32 shows the mean axial velocity profiles for Re= 8121 with the wall heat flux of the heated single phase ($q'' = 2.7$ kW/m^2), low boiling ($q'' = 16.4$ kW/m^2), and high boiling condition ($q'' = 42.8$ kW/m^2). It appears that for the single-phase case that the velocity profile develops in parabolic fashion exhibiting the well-known feature of having a maximum toward the center with the value of about 0.235 m/s at 8mm radially. Further increase in the heat flux generates boiling, which resulted in a higher velocity profile with a peak of about 0.2 m/s at around 1.75 mm radially. This increase in velocity gradient near the wall is attributed to the inhomogeneous distribution of the mean liquid density (caused by boiling), which in this case has become significant. The velocity profile continues to develop reaching the value of 0.241 m/s at 8mm. It is obvious that the influence of the boiling layer on velocity values extends over to almost the center of test section making the velocity profile higher across much of the liquid region. Upon increasing the heat flux even further, a higher boiling conditioned is reached producing thicker boiling layer. This forced the maximum velocity magnitude to increase and shift to the right with a peak of about 0.25 m/s at around 3.6 mm. However, a decrease in the velocity profile is seen as moving away from the wall to reach the values of 0.239 m/s at 8mm.

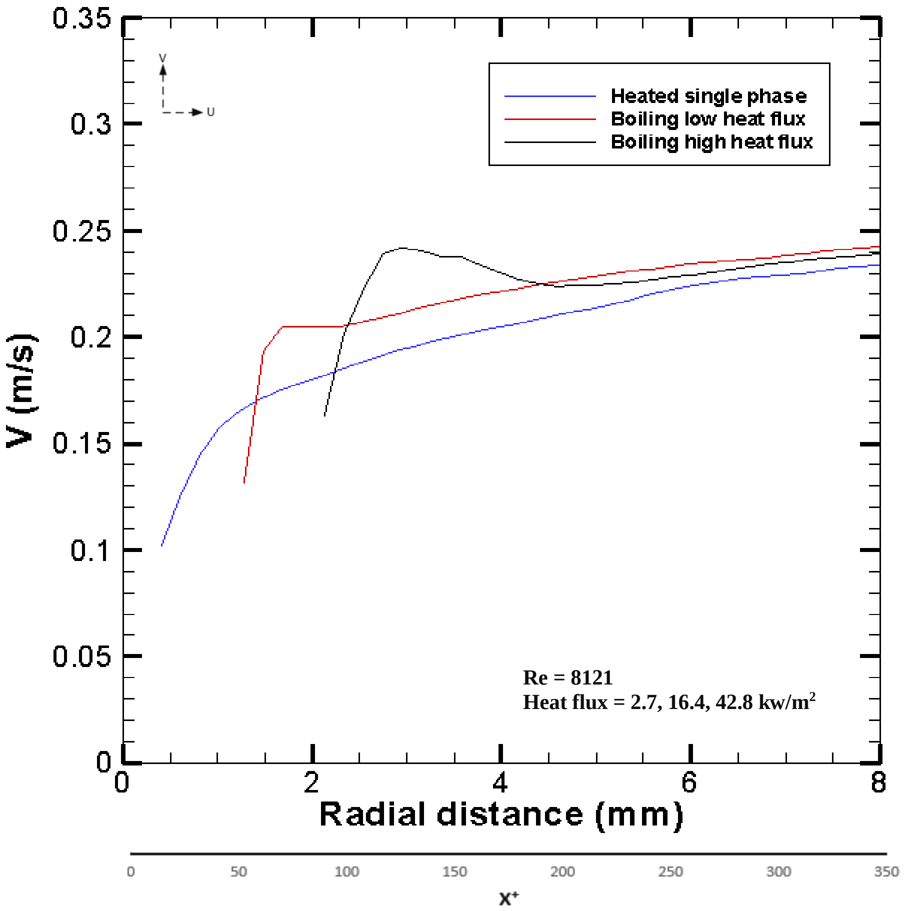

Figure 3.32: Average liquid velocity profiles given at the highest axial profiles for the three different heat fluxes with low Re.

Figure 3.33 shows the profiles of the mean axial velocity for Re= 20523 with the same heat flux values shown above. The single-phase condition here shows a similar trend observed before in the lower flow rate one but with a higher velocity magnitude due to the higher flow rate. The velocity value at 8 mm is shown to be around 0.31 m/s. However, the increase of axial liquid velocity due to the increase of wall heat flux is lower in both boiling conditions. This might suggest that the variations in the mean liquid density becomes less significant due to higher mixing with higher flow rate. In low boiling case, no peak near the wall is observed, but the velocity profile appears to increase steadily up until 1.75 mm. It, then, starts growing at a slower rate intersecting with the single phase profile at about 6 mm radially, but then it shows a slight increase to 0.315 at 8 mm. The influence of the wall heat flux is more noticeable in the high boiling case but with a smaller peak than the one seen in low Re condition; and no velocity reduction is observed in regions far from the wall as also seen previously. The velocity value at 8 mm appears to approach 0.32 m/s.

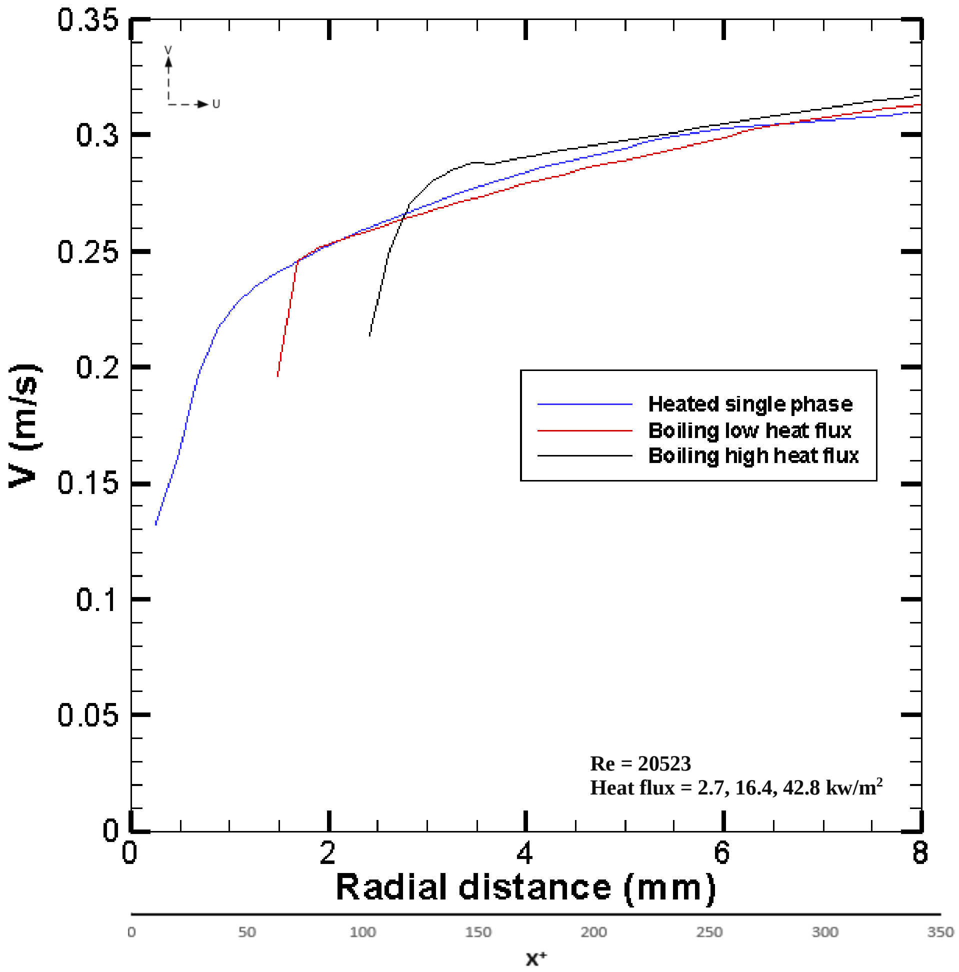

Figure 3.33: Average liquid velocity profiles given at the highest axial profiles for three different heat fluxes with the high Re.

3.5.2.2 Axial Liquid Velocity Fluctuation Intensity

The turbulence fluctuation intensities signify the turbulent levels and modifications occur in boiling processes. An increase in turbulent levels is expected here due to the mixing and stirring that happen to the liquid by the boiling bubbles. In this context, the axial turbulence intensity (V_{rms}) is defined as the root-mean-square of $V'(t)$. Where $V'(t)$ is nothing but a fluctuating component in an instantaneous recorded velocity at time (t). This fluctuating component is obtained by the following Reynold's decomposition,

$$\mathrm{V(t)} = \bar{V} + V'(t) \tag{3.2}$$

Where $\bar{V}$ is defined as the temporal mean velocity. Shown below in Figure 3.34 and 3.35 are the radial distributions of the average axial velocity fluctuation intensity for the heated single phase conditions, low and high Re, respectively. Those distributions are obtained from the same axial probes provided for the average velocity in previous section. In both single-phase cases, it appears that the intensity increases sharply toward the heater. In the high flow rate condition, the intensity profile seem to drop steadily as moving away from the heated surface and start to level off around 2 mm with apparently a random fluctuating fashion. It continues to fluctuate but drops slightly further toward the center of the channel. In the low flow condition, however, the intensity (near the heated wall) drops at a slower rate than the one seen in the high flow. It is clear that the turbulence intensity increase with the Reynold's number. Similar trends are seen in previous studies (Hasan et al., 1991; Estrada-Perez and Hassan, 2010; Roy et al., 1993).

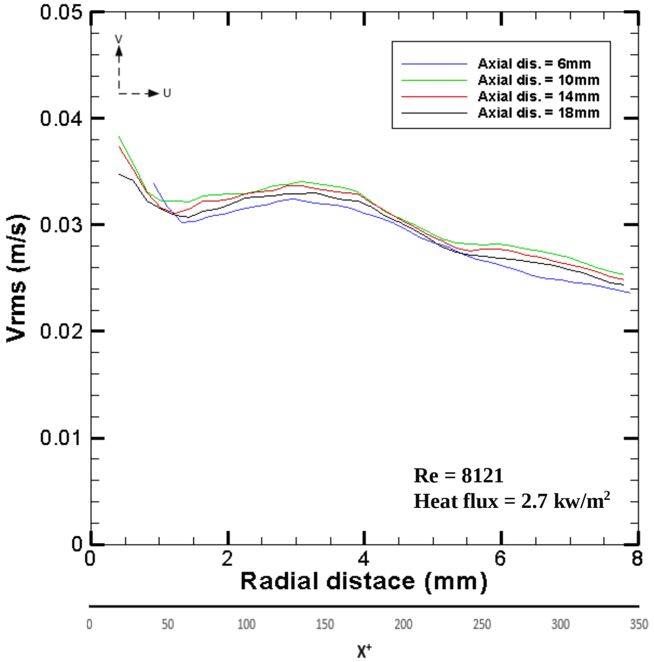

Figure 3.34: Average liquid axial intensity profiles for four different axial probes in heated single phase heat with low Re.

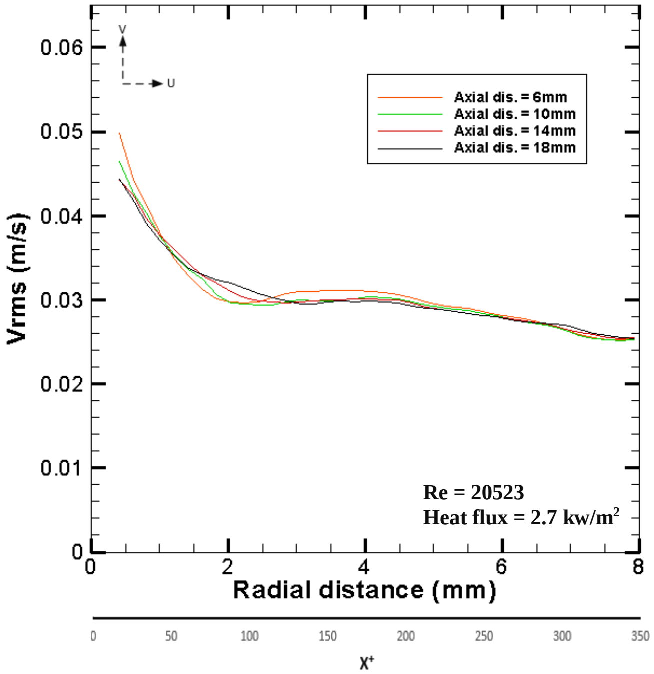

Figure 3.35: Average liquid axial intensity profiles for four different axial probes in heated single phase heat with high Re.

The turbulence intensity distributions for the boiling conditions are provided below in the following plots. As expected, significant increase in the intensity with wall heat flux and a strong effect in the proximity of the heated wall have been observed. The intensity profiles here are taken for regions just near the solid boiling layer and across the channel toward the center. In the low boiling condition with low flow rate (shown in Figure 3.36), a sharp increase is intensity is seen when the boiling layer forms. The concomitant radial shift with axial growth in intensity spikes is evident. The first intensity profile (at axial distance = 6 mm) seems to reach its maximum magnitude of about 0.05 m/s at around 1.25 mm. The intensity spikes continue to increase axially and shift radially to reach a value of 0.07 m/s at around 2 mm (at axial distance = 18 mm). This upward axial growth is attributed to the increase in turbulence level as bubbles layer grows in size inducing more liquid mixing and stirring. The high turbulent area (marked in the plots) where intensity level increase sharply is obtained to be between approximately 1 mm and 2.5 mm. The abrupt drop in intensity in region just adjoining the bubbles layer is observed to happen over a very small buffer regions (about 0.1 mm) where bubbles and liquid get mixed.

A similar trend is also seen in the high flow case (Figure 3.37). However, higher and shaper intensity spikes are observed due to the higher flow rate. As seen in the high flow for the heated single-phase, the intensity profiles appear to drop more abruptly than their counterparts in the low flow ones as the high turbulent region appear to approximately range between 1 mm and 2 mm. This trend may suggest that intensity profiles in the low flow rates develop slower but they spreads over wider radial distance.

The same trend can also be attributed to the formation and development of bubble layer thickness at different flow rates.

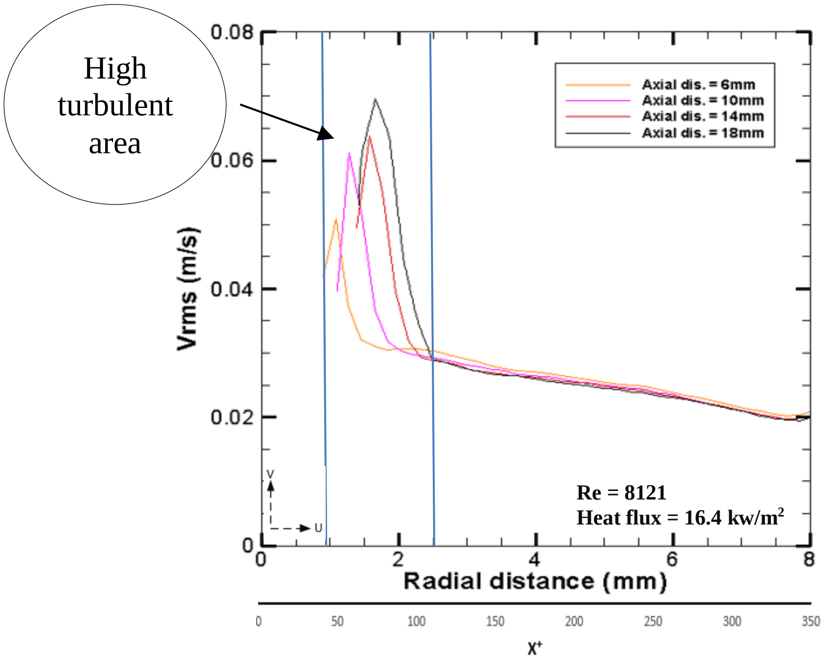

Figure 3.36: Average liquid axial intensity profiles for four different axial probes in low boiling case with low Re.

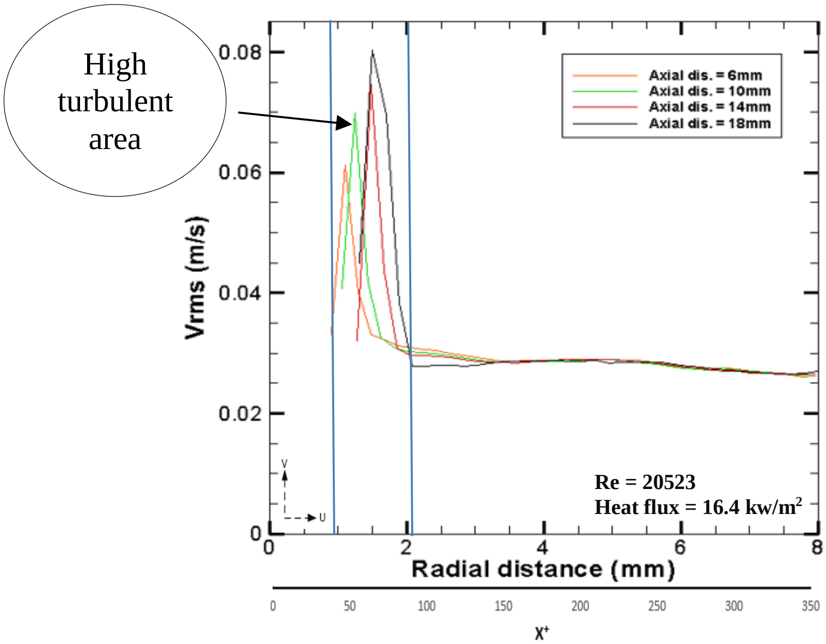

Figure 3.37: Average liquid axial intensity profiles for four different axial probes in low boiling case with high Re.

The high boiling conditions, low and high Re, are in provided in Figures 3.38 and 3.39, respectively. The increase of intensity (near the heated wall) with axial distance is evident in both of these cases as well. In the low Re one, the intensity profile at axial dis. = 6mm appear to reach its maximum value (0.06 m/s) at around 1.6 mm, whereas the highest axial profile (at dis. = 18mm) shows a maximum value of 0.14 m/s at around 2.5 mm. Higher intensity values (than those obtained in the low boiling cases) are expected here due to the higher heating applied to the liquid. Also, larger radial shift of spikes with axial distance can be observed as the solid bubbles layer grows larger in thickness while sliding upward. As a result, the high turbulent area, where intensity increases largely, is shown to spread over a wider radial distance than the those shown in the low boiling cases (on each respective axial location).

Similar behavior is also seen in the high flow case. And, because of the higher flow rate in high boiling condition, the intensity profiles are obtained to the highest (between 0.07 m/s at axial distance = 6 mm and 0.15 m/s at axial dis. = 18 mm). The radial spread of intensity here appears to be just slightly less than the one shown before (low Re and high heat flux) as the axial profiles appear to merge together just after 6 mm in radial distance.

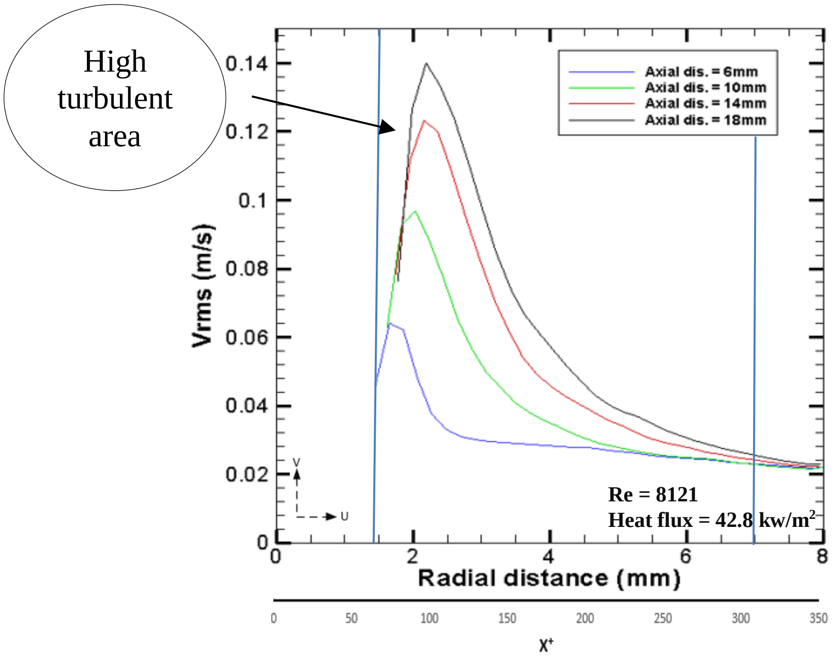

Figure 3.38: Average liquid axial intensity profiles for four different axial probes in high boiling case with low Re.

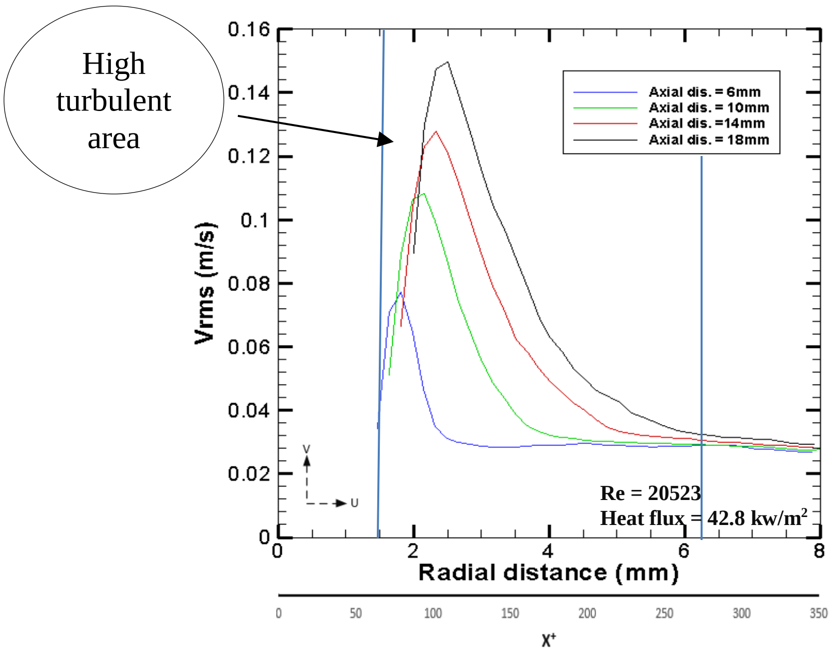

Figure 3.39: Average liquid axial intensity profiles for four different axial probes in high boiling with high Re.

3.5.2.3 Radial Liquid Velocity Fluctuation Intensity

The radial velocity fluctuations intensity (U_{rms}) can follow the same root-mean-square definition seen in the axial component. The Reynold's decomposition for the radial intensity is given as,

$$\mathrm{U(t)} = \bar{U} + U'(t) \tag{3.3}$$

Where $\bar{U}$ is defined as the temporal mean velocity in normal direction, and $U'(t)$ is the fluctuating component in an instantaneous recorded velocity at time (t). Provided below, in Figure 3.40 and 3.41, the intensity distributions for the low and high flow rates of low boiling case, respectively.

Figure 3.40 and 3.41 contains the radial profiles of this intensity (for low boiling conditions) for regions just near the bubbles layer and across the channel. The radial intensity does not seem to change much as the profile appear mostly flat with some fluctuation. A slight increase in regions adjoining the bubbles layer is seen especially in the high flow conditions. A noteworthy feature in Figure 3.40 and 3.41 is that the relative increase in the mean liquid radial velocity seem higher in lower axial locations. This connotes that the radial velocity field (near the bubbles layer) induced by the vapor bubbles is essentially random in nature with a rather small mean value. The bubbles are essentially moving in the axial direction while oscillating back and forth radially. This oscillating appear to be slightly higher at lower axial locations when first born and start sliding.

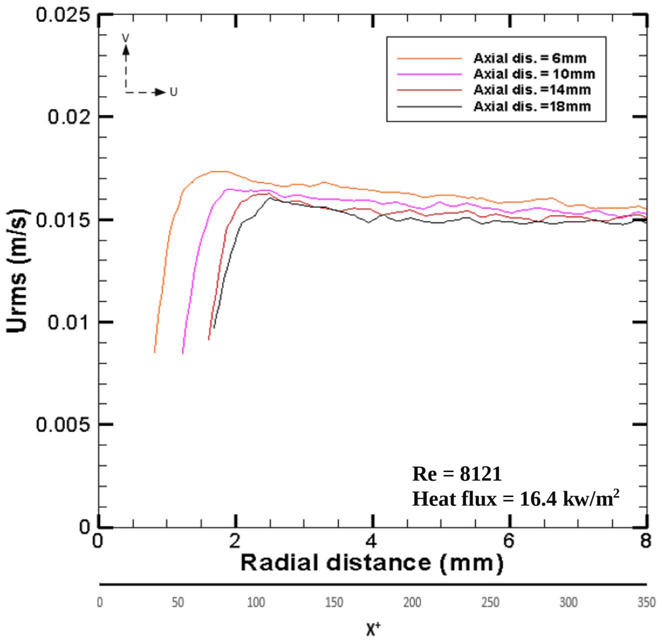

Figure 3.40: Average liquid radial intensity profiles for four different axial probes in low boiling with low Re.

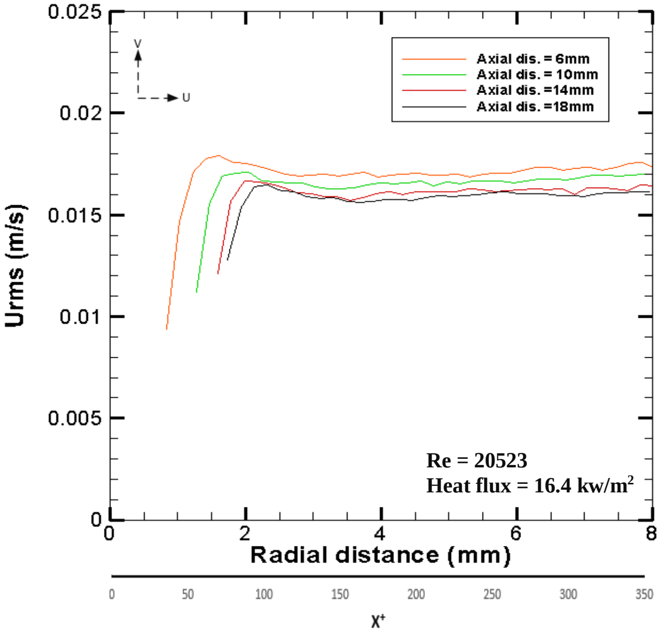

Figure 3.41: Average liquid radial intensity profiles for four different axial probes in low boiling case with high Re.

In the high boiling conditions, the radial intensity appear to be a lot higher. This is shown in Figure 3.42 and 3.43 for low and high Re, respectively. This increase in magnitude in high turbulent regions can be explained by the random oscillation of mixing and stirring of liquid neighboring the growing bubbles layer while sliding upward. Clearly, this mixing and stirring increase with the increasing bubble layer sizes.

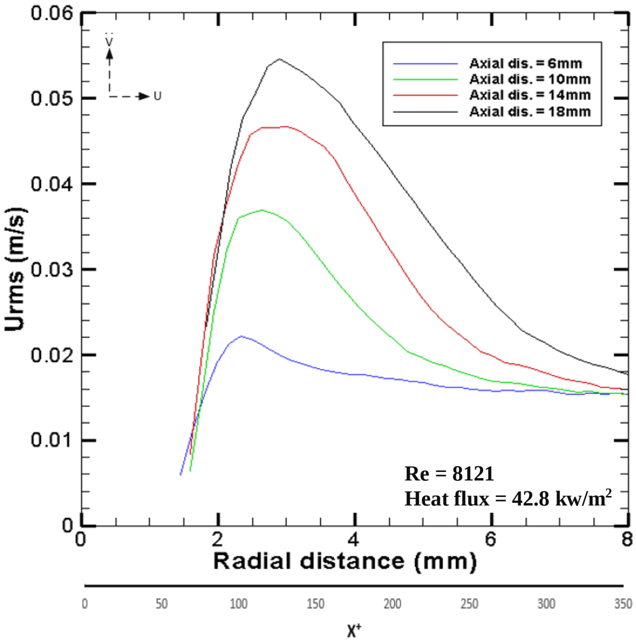

Figure 3.42: Average liquid radial intensity profiles for four different axial probes in high boiling case with low Re.

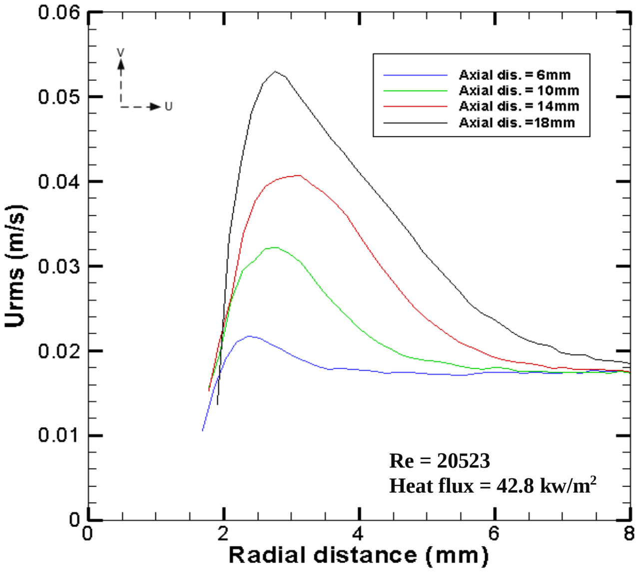

Figure 3.43: Average liquid radial intensity profiles for four different axial probes in high boiling case with high Re.

3.5.2.4 Liquid Reynold’s Stresses

The Reynold’s stresses (-$\overline{V'U'}$) for the low boiling conditions, with low and high Re, are given below in Figure 3.44 and 3.45, respectively. As expected, the Reynold’s stresses appear higher in regions adjoining the bubbles layer, which implies the turbulent nature of these regions. The obtained profiles near the bubbles layer seem to increase with axial distance in both conditions, as the developing bubble layers seem to push the liquid in the direction of the flow. The stresses in the higher flow reach higher values. This behavior is shown in other parameters.

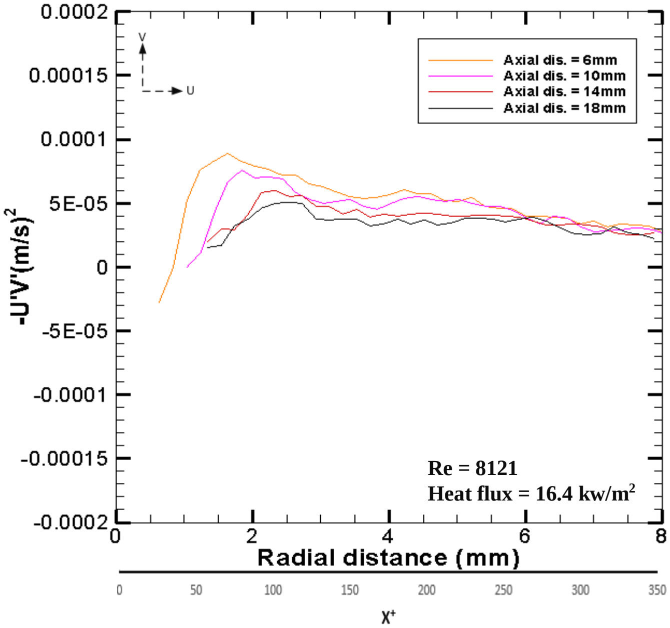

Figure 3.44: Average liquid Reynolds stress profiles for four different axial probes in low boiling case with low Re.

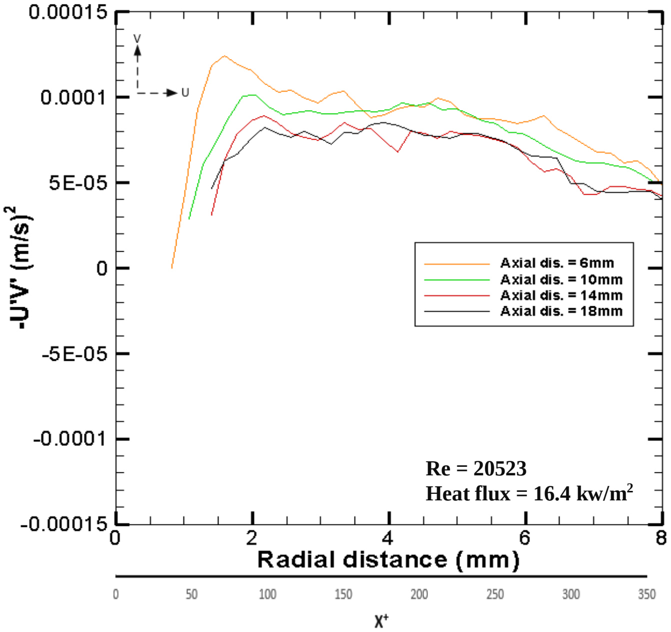

Figure 3.45: Average liquid Reynolds stress profiles for four different axial probes in low boiling case with high Re.

The plots in Figures 3.46 and 3.47 show the Reynold’s stresses for the high boiling conditions. Significant increase in stresses is obtained with higher heat flux. This increase in stress values appear, for low and high Re, concomitant with axial distance, where the adjoining bubbles layer areas become more chaotic as bubbles increase in size.

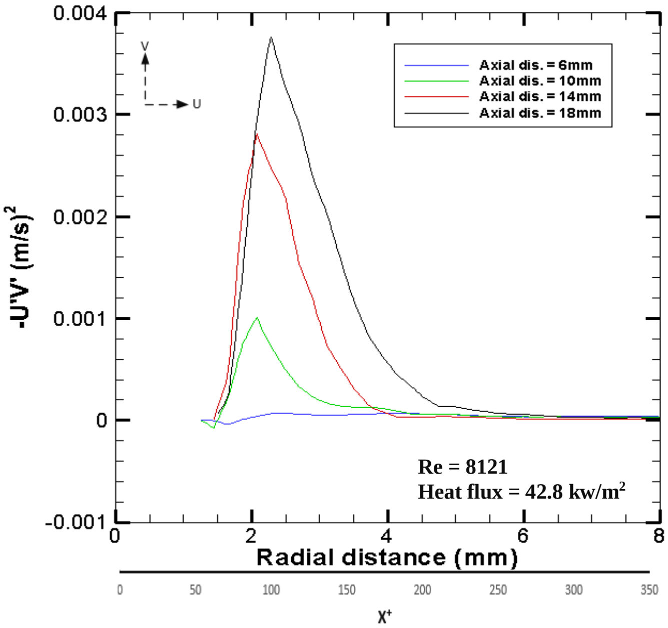

Figure 3.46: Average liquid Reynolds stress profiles for four different axial probes in high boiling case with low Re.

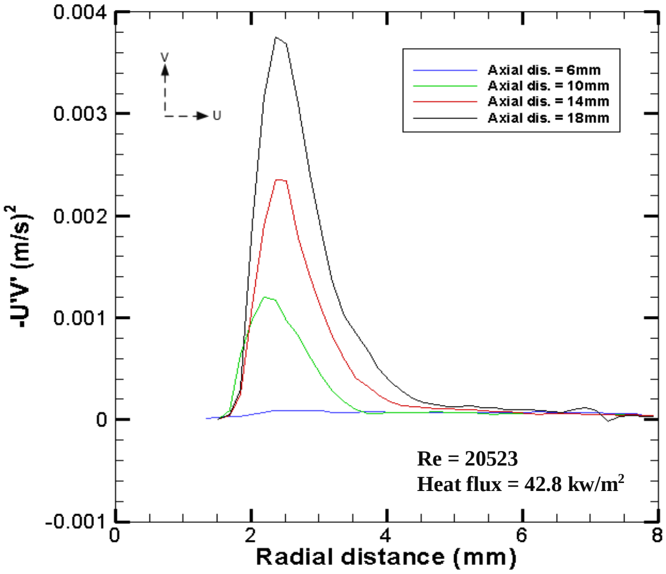

Figure 3.47: Average liquid Reynolds stress profiles for four different axial probes in high boiling case with high Re.

3.6 Experimental Uncertainties

The experimental uncertainties are addressed in this section. One major contributor to experimental uncertainties in this work is the statistical signification especially in the near-wall region. In order to quantify the measured flow statistics, an analysis is conducted to measure the sampling number across the radial distance at the axial locations of interest. This is done to quantify the influence of the statistical signification on the measured parameters. To this end, the number of samples (frames) that go into computing the liquid turbulence statistical parameters was calculated and plotted against the radial distance in Figure 3.48 and 3.49. The maximum sampling number shown here is 16662 frames, which represents the total frames in a stack of images obtained experimentally. It is shown clearly that the sampling number drops significantly in both of the low boiling conditions (see Figure 3.48) in the near-wall regions (below 2 mm) for all axial locations. This trend of sampling drop appear to be a function of the bubbles layer thickness as the sample numbers begin decreasing at further distance from the wall with higher axial distance. The sampling number is expected to be lower in regions mostly occupied by void due to the bubbles' masking technique employed in this work. In other words, for the purpose of this study, the bubble's occupied areas are considered zero liquid velocity regions and are not counted toward the liquid velocity measurements in that region. Therefore, the sampling number drops accordingly. This significant drop in sampling in those regions is seen to lead to higher measurement uncertainties, and as a result, it causes a large growth in standard deviations, which is shown in Figure 3.50 and 3.51.

In the higher boiling conditions (Figure 3.49), the sampling number starts dropping in around regions between 2 and 5 mm radially depending on the axial location. At higher axial location, the sampling number is seen to start dropping at a further distance from the heated wall due to the growing bubbles layer. The sampling number is shown to reach its lowest value (at all axial locations) in just below 2 mm, where the outer edge of bubbles layer starts forming. The standard deviations are shown to increase largely with the sampling number dropping especially in higher axial locations. It is suggested that the bigger the thickness of bubbles layer covering a wider radial distance, the less sampling number that can go into liquid velocity calculations, and so higher degree of deviations from the temporal mean are observed.

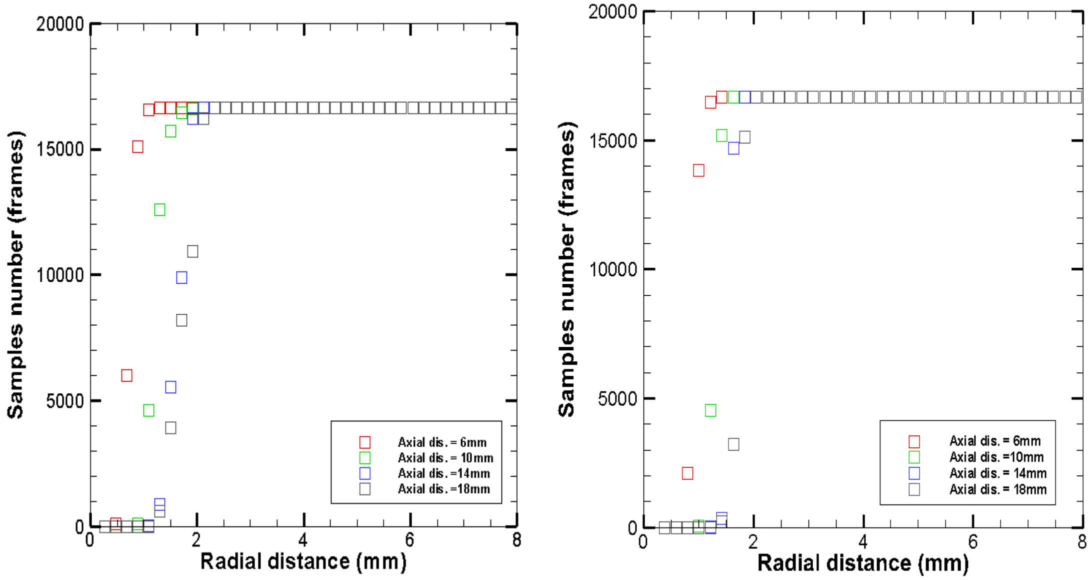

Figure 3.48: Sampling number obtained radially at different axial locations for low boiling condition with low Re (right) and high Re (left).

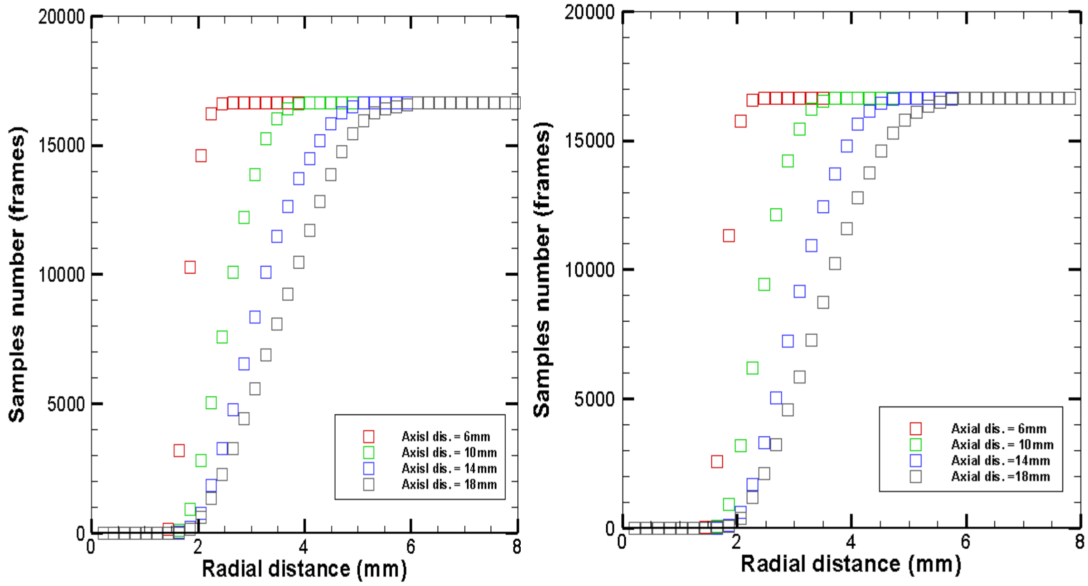

Figure 3.49: Sampling number obtained radially at different axial locations for high boiling conditions with low Re (right) and high Re (left).

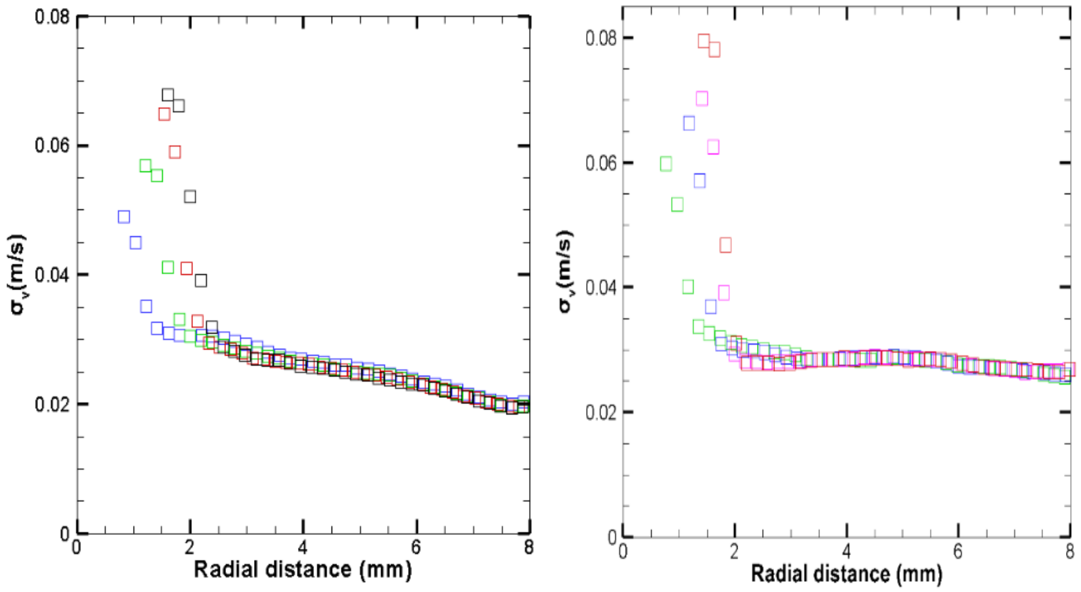

Figure 3.50: Standard deviations obtained radially at different axial locations for low boiling condition with low Re (right) and high Re (left).

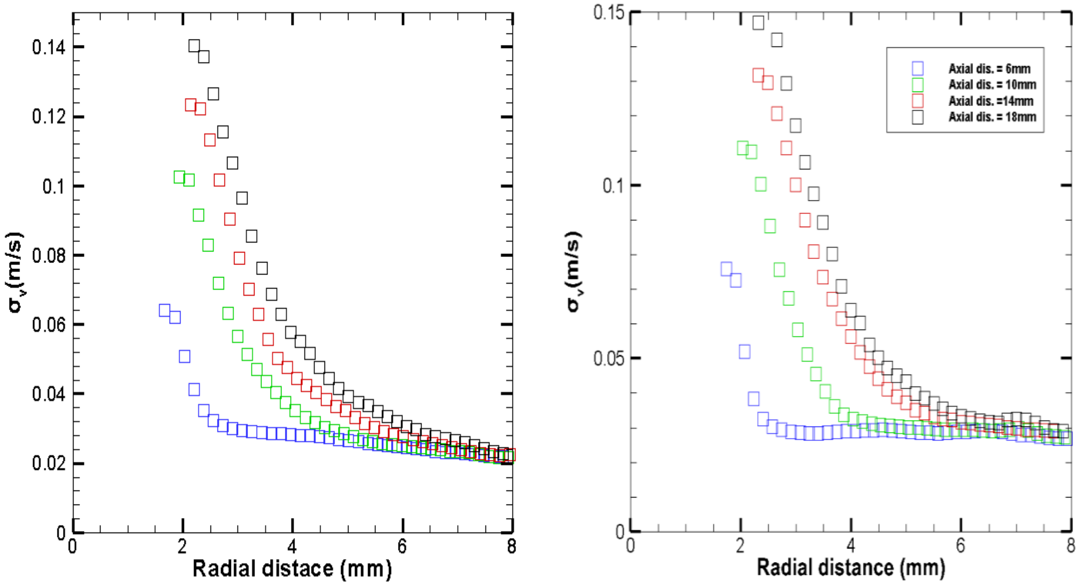

Figure 3.51 Standard deviations obtained radially at different axial locations for high boiling condition with low Re (right) and high Re (left).

Another error source can be induced by gravitational forces when the flow tracers' density differs vastly from the liquid's density. Such an affect can be quantified by the use of stokes drag law (Reithmuller, 2000). The gravitational induced velocity (U_g) follows the mathematical formulation given below as,

$$U_g = d_p^2 \frac{(\rho_p - \rho)}{18\mu} g \tag{3.4}$$

Where $d_p \; and \; \rho_p$ are the diameter and density of the particles, μ and ρ are the density and dynamic viscosity of the liquid, and g is the gravity constant. In this this study, the induced gravitational velocity (due to density variations) is obtained to be 42.8 µm/s. Therefore, the influence of density changes is assumed to be negligible.

Also, the Stoke number, which is often used to characterize the behavior of particles suspended in a fluid flow, is calculated using the following,

$$Stk = d_p^2 \frac{\rho_p}{18\mu \, D} U \tag{3.5}$$

Where U is the bulk liquid velocity at the middle of the channel, and D is the hydraulic diameter of the test section. The obtained value for the used silver coated particles with the working fluid's density being at room temperature (25 ºC) is shown to be very small (0.00012). In order to account for the boiling conditions, the same calculation is made when density drops by 50%. The obtained values was also shown to be very low as well (0.00025), which suggests that the flow tracers follow the working fluid closely even when its density varies significantly.

3.7 Conclusion

The PIV and the shadowgraph images acquired for the heated single-phase and boiling conditions are shown to provide information about the liquid turbulence statistics measurements near the bubbles layer region and the heated surface. The combinations of the information obtained from PIV and shadowgraph images as well as the infrared images are shown to provide faithful measurements for the two-dimensional axial liquid velocity profiles and thermometry measurements. This information provides insight into quantifying the heat flux influence on the liquid-phase behavior and liquid turbulence statistics. Four different horizontal line probes are marked in which liquid turbulence statistics profiles are obtained. In the heated single-phase, the velocity profiles are shown to exhibit the fully developed flow characteristics. The wall heating, as expected, has brought major changes in the velocity distribution profiles. The velocity boundary layer thicknesses are seen to grow with axial distance. This growth is shown to be a function of the bubbles' layer size. Higher heat flux levels induce thicker bubbles' layers, and as result higher velocity values and fluctuation intensities are shown near the bubble regions. This increase in values is associated with growing thickness of the velocity boundary layers. The bubbles layer is shown to grow thicker with lower flow rates as the bubbles are allowed to nucleate and grow in size with minimum liquid suppression. The thicker bubbles layer in the low flow rate conditions results in higher liquid velocity and fluctuation intensity values, near the bubbles region, than those obtained in higher flow rate cases. The bubbles layer velocities appear to increase with bubble sizes and flow rates. And so, the higher boiling condition with the higher flow exhibit highest bubbles layer velocities. This increase in velocity is observed to be concomitant with axial direction as bubbles gain momentum while sliding upward.

It is believed that this work can support the existing models developed to predict the wall heat flux partitioning, as it provides further understanding into the effect of the heat flux on the liquid statistical quantities and the flow patterns of the sub-cooled boiling flows. Such insights are needed to support and improve the modeling studies.

CHAPTER IV

CONCLUSIONS AND FUTUE WORK

This work has been developed in an effort to further understand, in a quantitative and a qualitative sense, the temperature distributions and flow structural behavior in sub-cooled boiling at various conditions. Temperature and velocity measurements are performed at different controlling parameters, namely, the heat flux levels and the flow rates, and the results are reported for each considered case. However, the available temperature and velocity information are still limited, and simultaneous temperature and velocity measurements are scarce. Previously, multiple boiling studies have been conducted to measure the temperature and velocity distributions simultaneously in order to estimate the turbulent momentum and heat transport. Determination of such parameters requires instantaneous and simultaneous measurements at the same location with high frequency resolutions (Estrada-Perez, 2014). Nonetheless, these studies were limited to intrusive sensors and probes and point-wise measurements. Therefore, the need for non-intrusive, whole-field, high fidelity, and simultaneous temperature and velocity measurements is at rise. The simultaneous temperature and velocity measurements may involve a similar set up provided for the PIV and shadowgraph experiment with some modifications. The fluorescent dye and the seeding particles may be both injected into the working liquid. With the experimental conditions remain the same, the acquired PIV images can provide the liquid turbulence statistics, and the shadowgraph images can be used to obtain the bubbles dynamics information as well as the fluorescent intensities for temperature measurements. Some other modifications can be done to better obtain more accurate measurements. These modifications can involve the dye selections and use of ratiometric method. As mentioned earlier, the ratiometric technique is shown to reduce the dependence on the incident laser light and enhance the fluorescent image qualities. The use of a two colors and single dye method with proper filtering tools is also a promising temperature measurements' candidate. Although the laser light reflections are reduced by the use of the bandpass filter, additional laser reflection reduction can be implemented by using less reflective heated surface material than the one used is this work (silicon wafer). Reducing the laser effects can minimize an additional heating at the heated surface and improve the measurement qualities (Jones, 2010). As discussed earlier, resolving the temperature distribution at the interfaces (especially near the bubbles region) is a subject to low spatial resolutions (approx. 1 pixel is obtained for the bubbles-liquid interface in this study). Therefore, enhancing the image qualities near the bubble-liquid boundaries and near heated wall is crucial for more accurate estimations at those regions. This enhancement can be done with higher magnification lenses and newer camera sensors. With the help of LED backlight (for better image illuminations), a faster camera shutter can also be useful in obtaining higher temporal resolutions to capture the fast moving temperature field at the interfaces.

REFERENCES

Alvarez-Herrera, C., Moreno-Hernández, D., Barrientos-García, B., & Guerrero-Viramontes, J. A. (2009). Temperature measurement of air convection using a schlieren system. *Optics & Laser Technology*, *41*(3), 233-240.

Basu, N., Warrier, G. R., & Dhir, V. K. (2005). Wall heat flux partitioning during subcooled flow boiling: Part 1—model development. *Journal of heat Transfer*, *127*(2), 131-140.

Bruchhausen, M., Guillard, F., & Lemoine, F. (2005). Instantaneous measurement of two-dimensional temperature distributions by means of two-color planar laser induced fluorescence (PLIF). *Experiments in fluids*, *38*(1), 123-131.

Castanet, G., Lavieille, P., Lebouché, M., & Lemoine, F. (2003). Measurement of the temperature distribution within monodisperse combusting droplets in linear streams using two-color laser-induced fluorescence. *Experiments in Fluids*, *35*(6), 563-571.

Chu, I. C., Lee, S. T., Cho, Y. I., & Song, C. H. (2010). Bubble Lift-off Diameter and frequency in a Vertical Subcooled Boiling Flow.

Coppeta, J., & Rogers, C. (1998). Dual emission laser induced fluorescence for direct planar scalar behavior measurements. *Experiments in Fluids*, *25*(1), 1-15.

Coolen, M. C. J., Kieft, R. N., Rindt, C. C. M., & Van Steenhoven, A. A. (1999). Application of 2-D LIF temperature measurements in water using a Nd: YAG laser. *Experiments in Fluids*, *27*(5), 420-426.

Donnelly, B., Meehan, R. R., Nolan, K., & Murray, D. B. (2015). The dynamics of sliding air bubbles and the effects on surface heat transfer. *International Journal of Heat and Mass Transfer*, *91*, 532-542.

Donnelly, B., Persoons, T., Nolan, K., & Murray, D. B. (2016, September). Forced convection in the wakes of sliding bubbles. In *Journal of Physics: Conference Series* (Vol. 745, No. 3, p. 032117). IOP Publishing.

Dhir, V. K., Abarajith, H. S., & Li, D. (2007). Bubble dynamics and heat transfer during pool and flow boiling. *Heat Transfer Engineering*, *28*(7), 608-624.

Di, Y. (2012). *Experimental Observation and Measurements of Pool Boiling Heat Transfer using PIV, Shadowgraphy, RICM Techniques* (Doctoral dissertation).

Euh, D., Ozar, B., Hibiki, T., Ishii, M., & Song, C. H. (2010). Characteristics of bubble departure frequency in a low-pressure subcooled boiling flow. *Journal of nuclear science and technology*, *47*(7), 608-617.

Estrada Perez, C. E. (2014). *Multi-Scale Experiments in Turbulent Subcooled Boiling Flow through a Square Channel with a Single Heated Wall* (Doctoral dissertation).

Estrada-Perez, C. E., & Hassan, Y. A. (2010). PTV experiments of subcooled boiling flow through a vertical rectangular channel. *International Journal of Multiphase Flow*, *36*(9), 691-706.

Estrada-Pérez, C. E., Hassan, Y. A., Alkhudhiri, B., & Yoo, J. (2018). Time-resolved measurements of liquid–vapor thermal interactions throughout the full life-cycle of sliding bubbles at subcooled flow boiling conditions. *International Journal of Multiphase Flow*, *99*, 94-110.

Estrada-Pérez, C. E., Hassan, Y. A., & Tan, S. (2011). Experimental characterization of temperature sensitive dyes for laser induced fluorescence thermometry. *Review of Scientific Instruments*, *82*(7), 074901.

Fenner, A. J. (2017). *Two-Color/Two-Dye Planar Laser-Induced Fluorescence Thermography for Temperature Measurements at an Evaporating Meniscus* (Doctoral dissertation, Technische Universität).

Fenner, A., & Stephan, P. (2017). Two dye combinations suitable for two-color/two-dye laser-induced fluorescence thermography for ethanol. *Experiments in Fluids*, *58*(6), 65.

Jones, B. J. (2010). Fundamental studies of thermal transport and liquid-vapor phase change using microscale diagnostic techniques.

Funatani, S., Fujisawa, N., & Ikeda, H. (2004). Simultaneous measurement of temperature and velocity using two-colour LIF combined with PIV with a colour CCD camera and its application to the turbulent buoyant plume. *Measurement Science and Technology*, *15*(5), 983.

Gerardi, C., Buongiorno, J., Hu, L. W., & McKrell, T. (2011). Infrared thermometry study of nanofluid pool boiling phenomena. *Nanoscale research letters*, *6*(1), 232.

Gerardi, C., Buongiorno, J., Hu, L. W., & McKrell, T. (2010). Study of bubble growth in water pool boiling through synchronized, infrared thermometry and high-speed video. *International Journal of Heat and Mass Transfer*, *53*(19-20), 4185-4192.

Guan, P., Jia, L., Yin, L., & Tan, Z. (2016). Effect of bubble contact diameter on bubble departure size in flow boiling. *Experimental Heat Transfer*, *29*(1), 37-52.

Hassan, Y. A., Estrada-Perez, C. E., & Yoo, J. S. (2014). Measurement of subcooled flow boiling using Particle Tracking Velocimetry and infrared thermographic technique. *Nuclear Engineering and Design*, *268*, 185-190.

Hasan, A., Roy, R. P., & Kalra, S. P. (1992). Velocity and temperature fields in turbulent liquid flow through a vertical concentric annular channel. *International journal of heat and mass transfer*, *35*(6), 1455-1467.

Hishida, K., & Sakakibara, J. (2000). Combined planar laser-induced fluorescence–particle image velocimetry technique for velocity and temperature fields. *Experiments in Fluids*, *29*(1), S129-S140.

Jung, S., & Kim, H. (2014). An experimental method to simultaneously measure the dynamics and heat transfer associated with a single bubble during nucleate boiling on a horizontal surface. *International Journal of Heat and Mass Transfer, 73*, 365-375.

Kang, S., Patil, B., Zarate, J. A., & Roy, R. P. (2001). Isothermal and heated turbulent upflow in a vertical annular channel–Part I. Experimental measurements. *International journal of heat and mass transfer*, *44*(6), 1171-1184.

Kang, S., Zarate, J. A., & Laporta, A. (2002). Turbulent Subcooled Boiling Flow—Experiments and Simulations.

Lemoine, F., Antoine, Y., Wolff, M., & Lebouche, M. (1999). Simultaneous temperature and 2D velocity measurements in a turbulent heated jet using combined laser-induced fluorescence and LDA. *Experiments in fluids*, *26*(4), 315-323.

Loitsianskii, L. G. (1945). *Some basic laws of isotropic turbulent flow*. TSAGI (CENTRAL AEROHYDRODYNAMIC INST) ZHUKOVSKY (RUSSIA).

Pope, S. B. (2001). Turbulent flows.

Lindken, R., & Merzkirch, W. (2002). A novel PIV technique for measurements in multiphase flows and its application to two-phase bubbly flows. *Experiments in fluids*, *33*(6), 814-825.

Lavieille, P., Delconte, A., Blondel, D., Lebouché, M., & Lemoine, F. (2004). Non-intrusive temperature measurements using three-color laser-induced fluorescence. *Experiments in Fluids*, *36*(5), 706-716.

Lavieille, P., Lemoine, F., Lavergne, G., & Lebouché, M. (2001). Evaporating and combusting droplet temperature measurements using two-color laser-induced fluorescence. *Experiments in fluids*, *31*(1), 45-55.

Lavieille, P., Lemoine, F., Lavergne, G., Virepinte, J. F., & Lebouché, M. (2000). Temperature measurements on droplets in monodisperse stream using laser-induced fluorescence. *Experiments in Fluids*, *29*(5), 429-437.

Lavieille, P., Lemoine, F., & Lebouché, M. (2002). Investigation on temperature of evaporating droplets in linear stream using two-color laser-induced fluorescence. *Combustion science and technology*, *174*(4), 117-142.

Meehan, R. R., Donnelly, B., Nolan, K., Persoons, T., & Murray, D. B. (2016). Flow structures and dynamics in the wakes of sliding bubbles. *International Journal of Multiphase Flow*, *84*, 145-154.

Maurus, R., & Sattelmayer, T. (2006). Bubble and boundary layer behaviour in subcooled flow boiling. *International journal of thermal sciences*, *45*(3), 257-268.

MIT. Basics of Turbulent Flow. Retrieved from http://www.mit.edu/course/1/1.061/www/dream/SEVEN/SEVENTHEORY.PDF

3M Novec 7000 Engineered Fluid. (2014, November). Retrieved from https://multimedia.3m.com/mws/media/121372O/3m-novec-7000-engineered-fluid-tds.pdf

Natrajan, V. K., & Christensen, K. T. (2008). Two-color laser-induced fluorescent thermometry for microfluidic systems. *Measurement Science and Technology*, *20*(1), 015401.

Prevosto, L., Artana, G., Mancinelli, B., & Kelly, H. (2010). Schlieren technique applied to the arc temperature measurement in a high energy density cutting torch. *Journal of Applied Physics*, *107*(2), 023304.

Ross, D., Gaitan, M., & Locascio, L. E. (2001). Temperature measurement in microfluidic systems using a temperature-dependent fluorescent dye. *Analytical chemistry*, *73*(17), 4117-4123.

Roy, R. P., Hasan, A., & Kalra, S. P. (1993). Temperature and velocity fields in turbulent liquid flow adjacent to a bubbly boiling layer. *International journal of multiphase flow*, *19*(5), 765-795.

Roy, R. P., Velidandla, V., & Kalra, S. P. (1997). Velocity field in turbulent subcooled boiling flow. *Journal of Heat Transfer*, *119*(4), 754-766.

Roy, R. P., Velidandla, V., Kalra, S. P., & Peturaud, P. (1994). Local measurements in the two-phase region of turbulent subcooled boiling flow. *Journal of heat transfer*, *116*(3), 660-669.

Seuntiëns, H. J., Kieft, R. N., Rindt, C. C. M., & Van Steenhoven, A. A. (2001). 2D temperature measurements in the wake of a heated cylinder using LIF. *Experiments in Fluids*, *31*(5), 588-595.

Sakakibara, J., & Adrian, R. J. (2004). Measurement of temperature field of a Rayleigh-Benard convection using two-color laser-induced fluorescence. *Experiments in fluids*, *37*(3), 331-340.

Sakakibara, J., & Adrian, R. J. (1999). Whole field measurement of temperature in water using two-color laser induced fluorescence. *Experiments in Fluids*, *26*(1-2), 7-15.

Sakakibara, J., Hishida, K., & Maeda, M. (1997). Vortex structure and heat transfer in the stagnation region of an impinging plane jet (simultaneous measurements of velocity and temperature fields by digital particle image velocimetry and laser-induced fluorescence). *International journal of heat and mass transfer*, *40*(13), 3163-3176.

Situ, R., Ishii, M., Hibiki, T., Tu, J. Y., Yeoh, G. H., & Mori, M. (2008). Bubble departure frequency in forced convective subcooled boiling flow. *International Journal of Heat and Mass Transfer*, *51*(25-26), 6268-6282.

http://www.iss.com/resources/research/technical_notes/PC1_PolarizationStandards.html

Timmins, B. H., Wilson, B. W., Smith, B. L., & Vlachos, P. P. (2012). A method for automatic estimation of instantaneous local uncertainty in particle image velocimetry measurements. *Experiments in fluids*, *53*(4), 1133-1147.

Terpetschnig, E., Yevgen, P., Eichorst, J. (2015). Polarization Standards. Retrieved from http://www.iss.com/resources/research/technical_notes/PC1_PolarizationStandards.html

Tong, L. S. (2018). *Boiling heat transfer and two-phase flow*. Routledge.

Vogt, J. (2014). *Development of novel Particle Image Thermometry methods for highly resolved measurements of temperature and velocity fields in fluids* (Doctoral dissertation, Technische Universität).

Velidandla, V., Putta, S., & Roy, R. P. (1996). Turbulent velocity field in isothermal and heated liquid flow through a vertical annular channel. *International Journal of Heat and Mass Transfer*, *39*(16), 3333-3346.

Virginia Polytechnic Institute and State University. (2011). Prana PIV Manual: Version 1.0, VA: Virginia Polytechnic Institute.

Wilson, B. M., & Smith, B. L. (2013). Uncertainty on PIV mean and fluctuating velocity due to bias and random errors. *Measurement Science and Technology*, *24*(3), 035302.

Warrier, G. R., & Dhir, V. K. (2006). Heat transfer and wall heat flux partitioning during subcooled flow nucleate boiling—a review. *Journal of Heat Transfer*, *128*(12), 1243-1256.

Yeoh, G. H., Cheung, S. C., Tu, J. Y., & Ho, M. K. (2008). Fundamental consideration of wall heat partition of vertical subcooled boiling flows. *International Journal of Heat and Mass Transfer*, *51*(15-16), 3840-3853.

Yoo, J., Estrada-Perez, C. E., & Hassan, Y. A. (2015). An accurate wall temperature measurement using infrared thermometry with enhanced two-phase flow visualization in a convective boiling system. *International Journal of Thermal Sciences*, *90*, 248-266.

Yoo, J., Estrada-Perez, C. E., & Hassan, Y. A. (2016). Experimental study on bubble dynamics and wall heat transfer arising from a single nucleation site at subcooled flow boiling conditions–Part 1: Experimental methods and data quality verification. *International Journal of Multiphase Flow*, *84*, 315-324.

Yang, L. X., Guo, A., & Liu, D. (2016). Experimental investigation of subcooled vertical upward flow boiling in a narrow rectangular channel. *Experimental Heat Transfer*, *29*(2), 221-243.

Zarate, J. A., Roy, R. P., & Laporta, A. (2001). Isothermal and heated turbulent upflow in a vertical annular channel–Part II. Numerical simulations. *International journal of heat and mass transfer*, *44*(6), 1185-1199.

APPENDIX A

IR TEMPERATURE FIELDS AND INSTANTANEOUS IMAGES

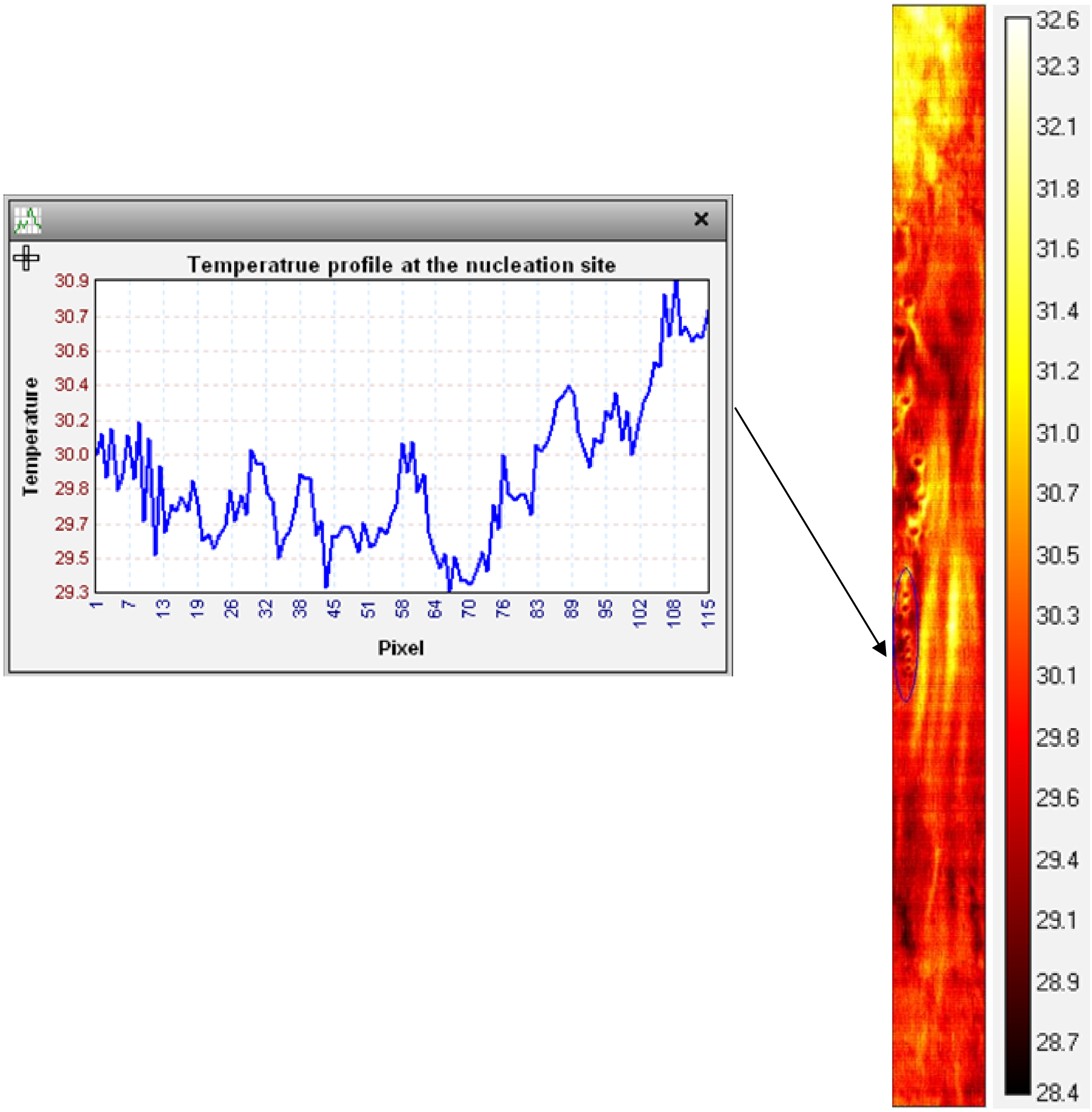

Figure A.1: IR image for low boiling and high Re condition (right) and the liquid temperature profile at the nucleation site (left).

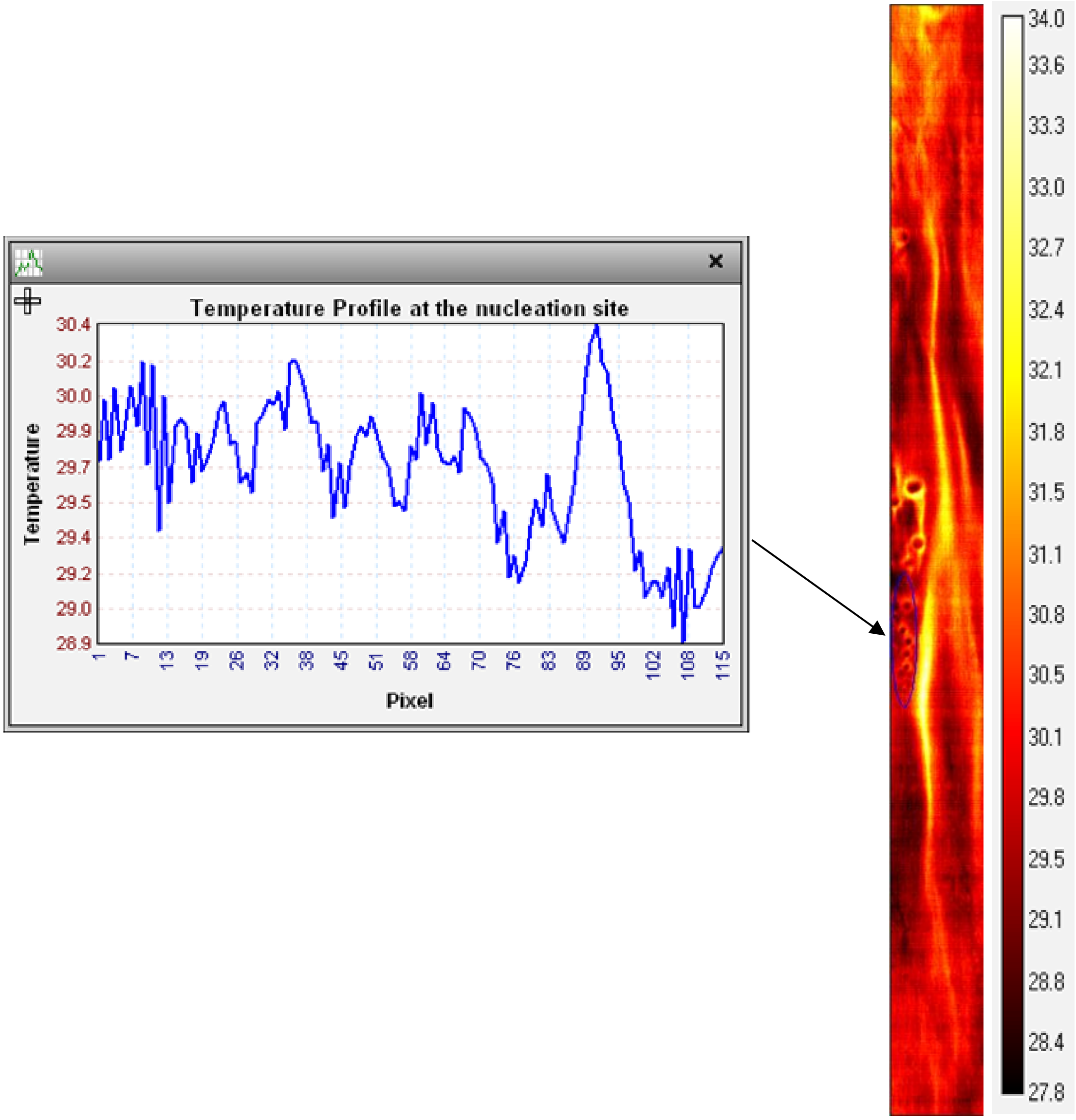

Figure A.2: IR image for low boiling and low Re condition (right) and the liquid temperature profile at the nucleation site (left).

APPENDIX B

LIQUID TURBULENCE STATSTICS AND IR IMAGES

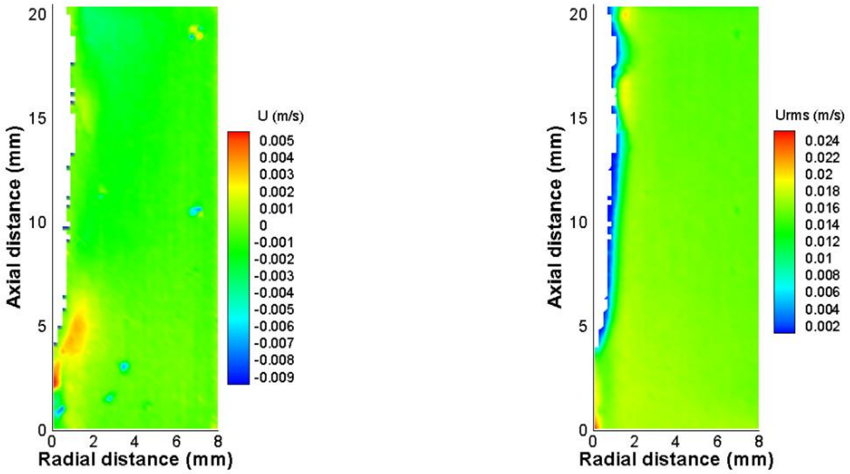

Figure B.1: Radial velocity field of the low boiling with low Re (left) and radial velocity fluctuation intensity field of the same condition (right).

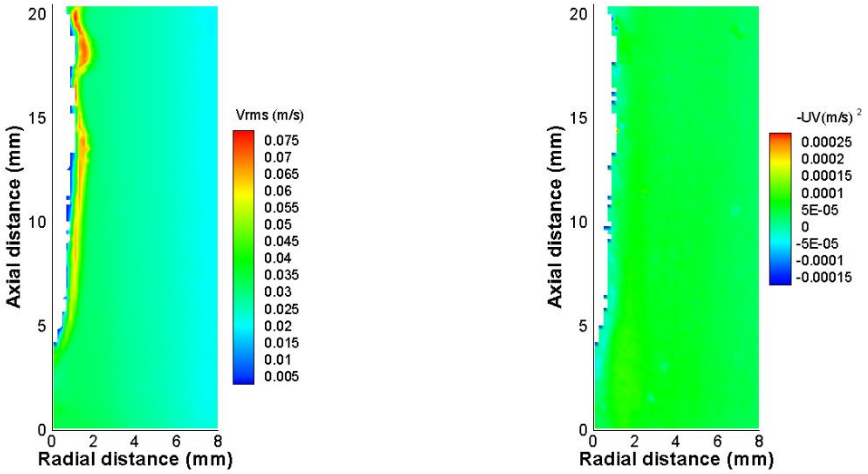

Figure B.2: Axial velocity fluctuation intensity field for low boiling with low Re condition (left) and Reynold's stress field of the same condition (right).

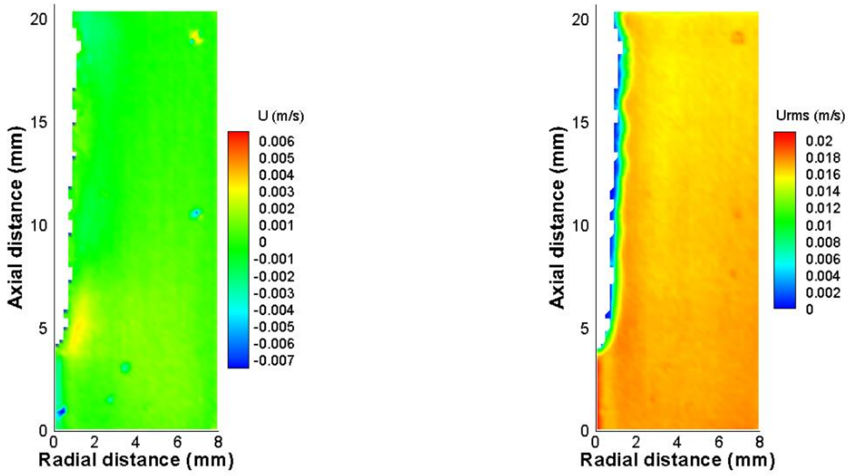

Figure B.3: Radial velocity field of the low boiling with high Re (left) and radial velocity fluctuation intensity field of the same condition (right).

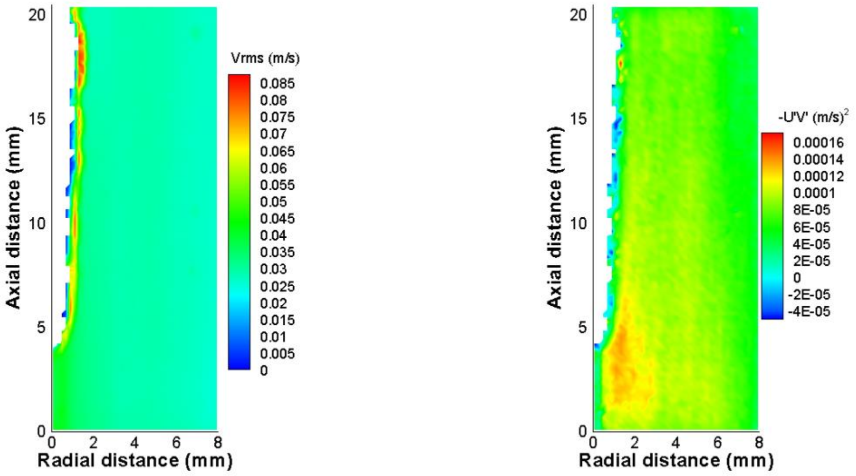

Figure B.4: Axial velocity fluctuation intensity field for low boiling with high Re condition (left) and Reynold's stress field of the same condition (right).

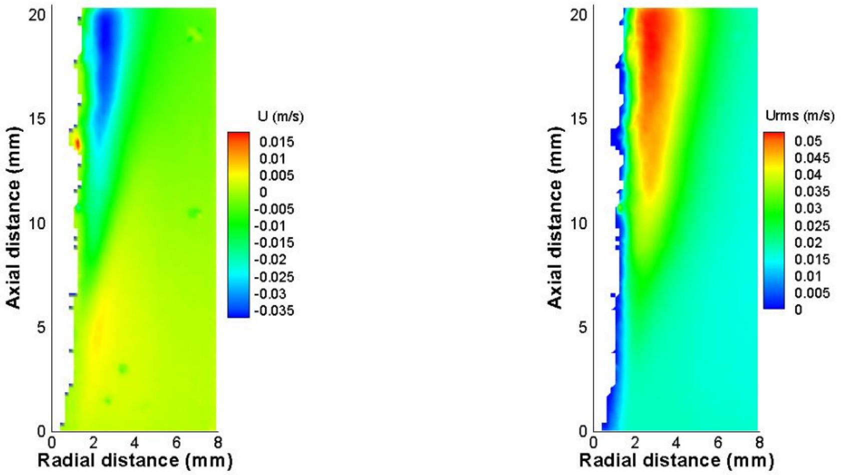

Figure B.5: Radial velocity field of the high boiling with low Re (left) and radial velocity fluctuation intensity field of the same condition (right).

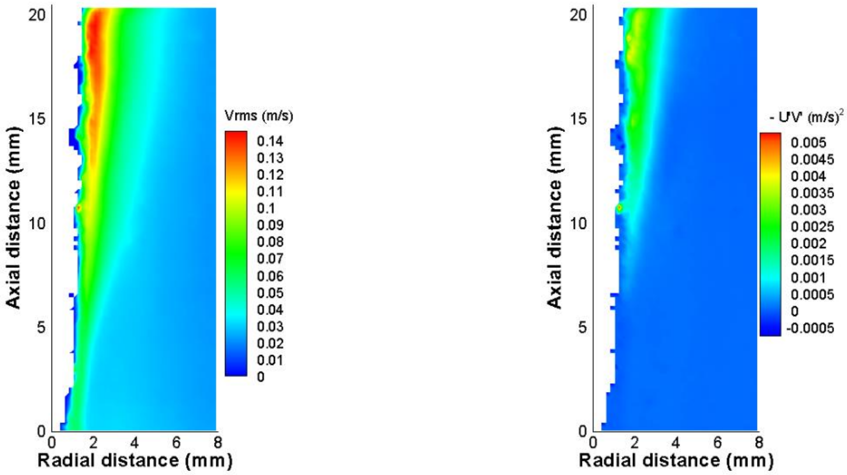

Figure B.6: Axial velocity fluctuation intensity field for high boiling with low Re condition (left) and Reynold’s stress field of the same condition (right).

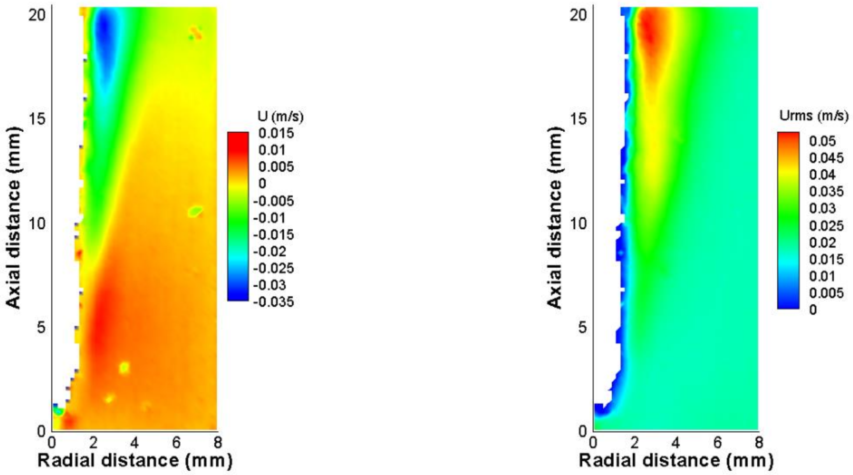

Figure B.7: Radial velocity field of the high boiling with high Re (left) and radial velocity fluctuation intensity field of the same condition (right).

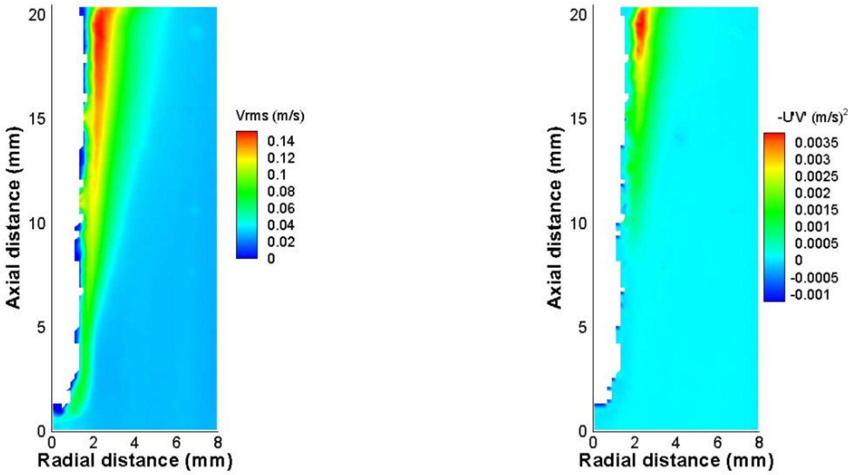

Figure B.8: Axial velocity fluctuation intensity field for high boiling with high Re condition (left) and Reynold's stress field of the same condition (right).

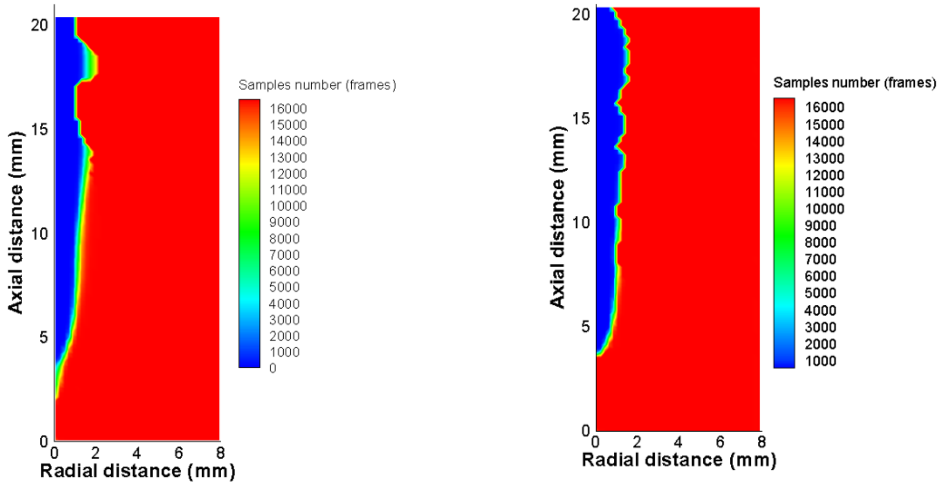

Figure B.9: Sample number field for low boing with low Re condition (left) and low boiling with high Re condition (right).

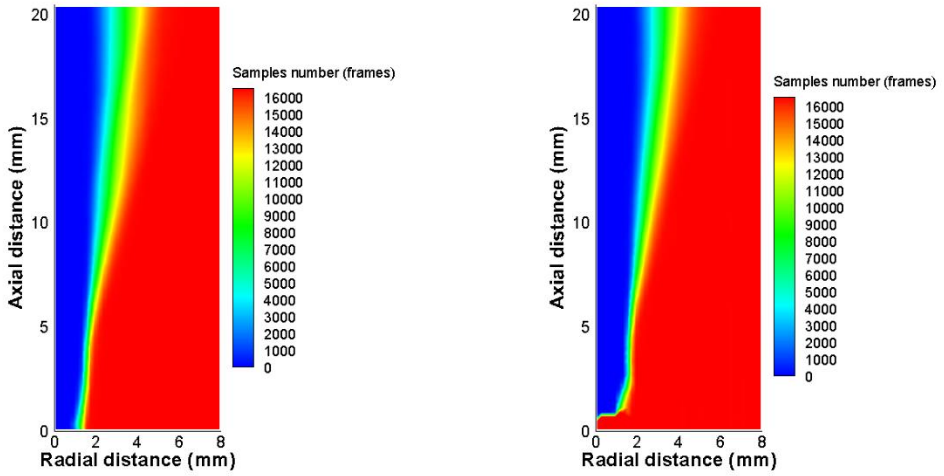

Figure B.10: Sample number field for high boiling with low Re (left) and high boiling with high Re condition (right)

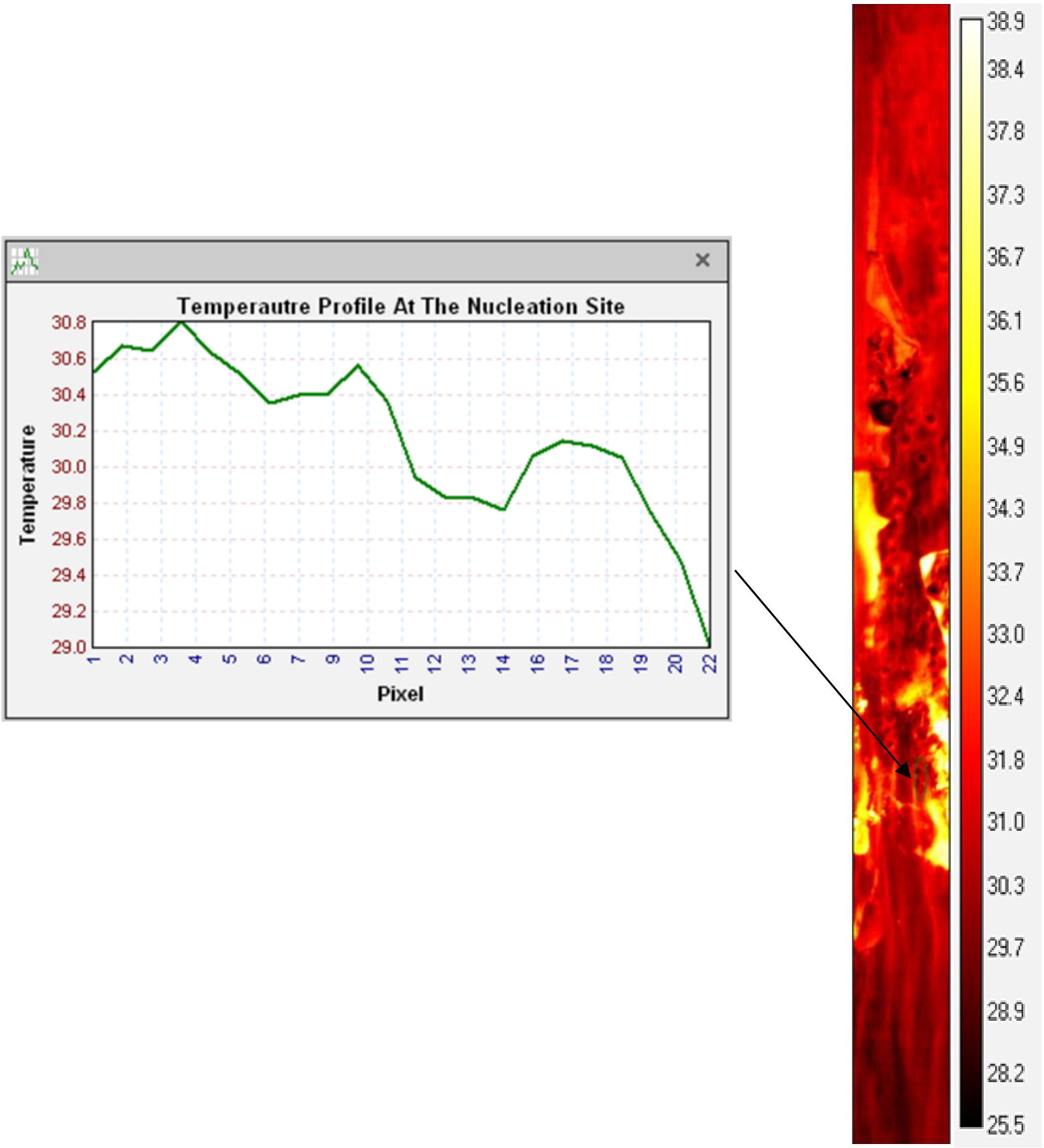

Figure B.11: IR image for low boiling and high Re condition (right) and the liquid temperature profile at the nucleation site (left).

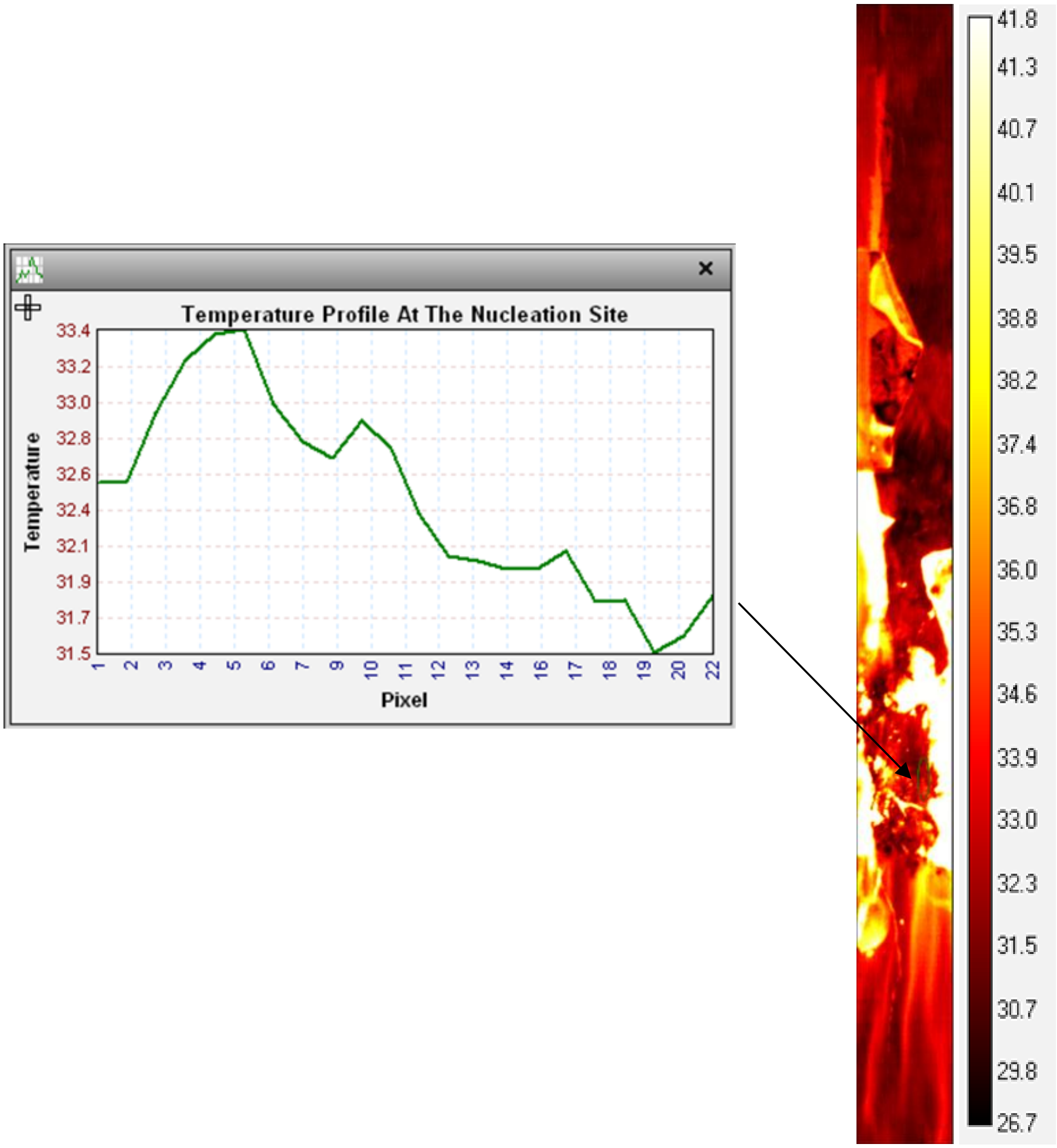

Figure B.12: IR image for high boiling and low Re condition (right) and the liquid temperature profile at the nucleation site (left).

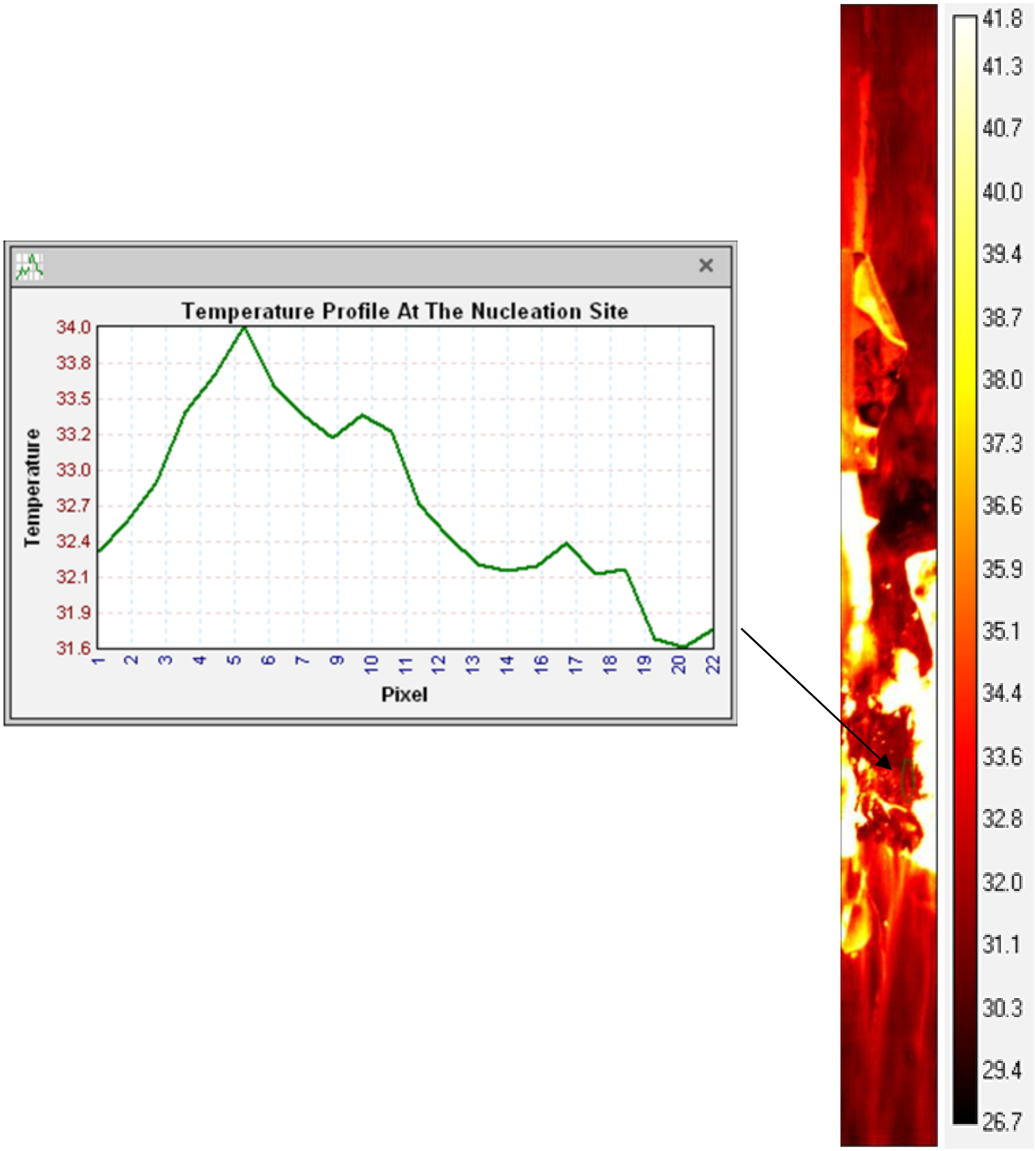

Figure B.13: IR image for high boiling and high Re condition (right) and the liquid temperature profile at the nucleation site (left).

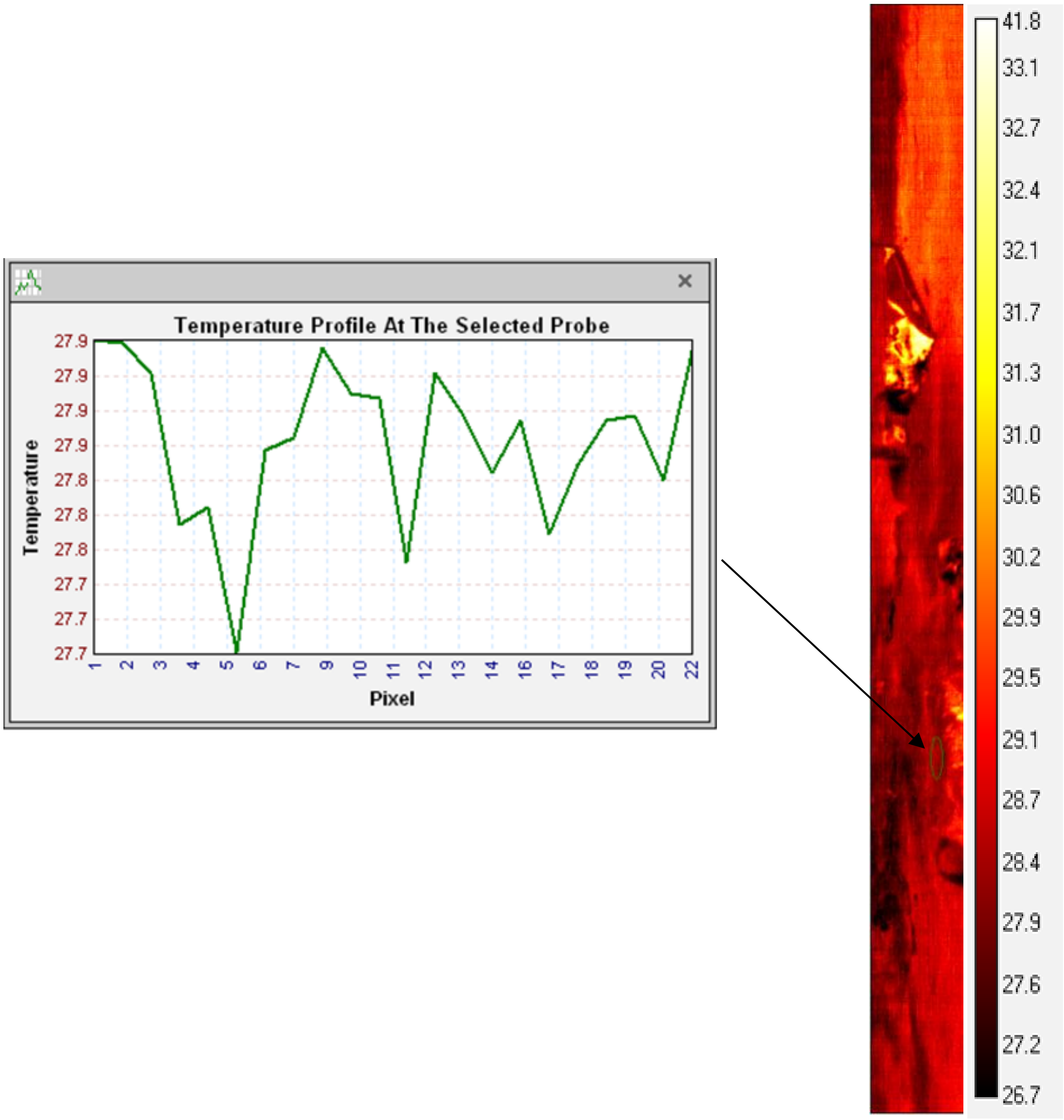

Figure B.14: IR image for the heated single-phase and low Re condition (right) and the liquid temperature profile at the nucleation site (left).

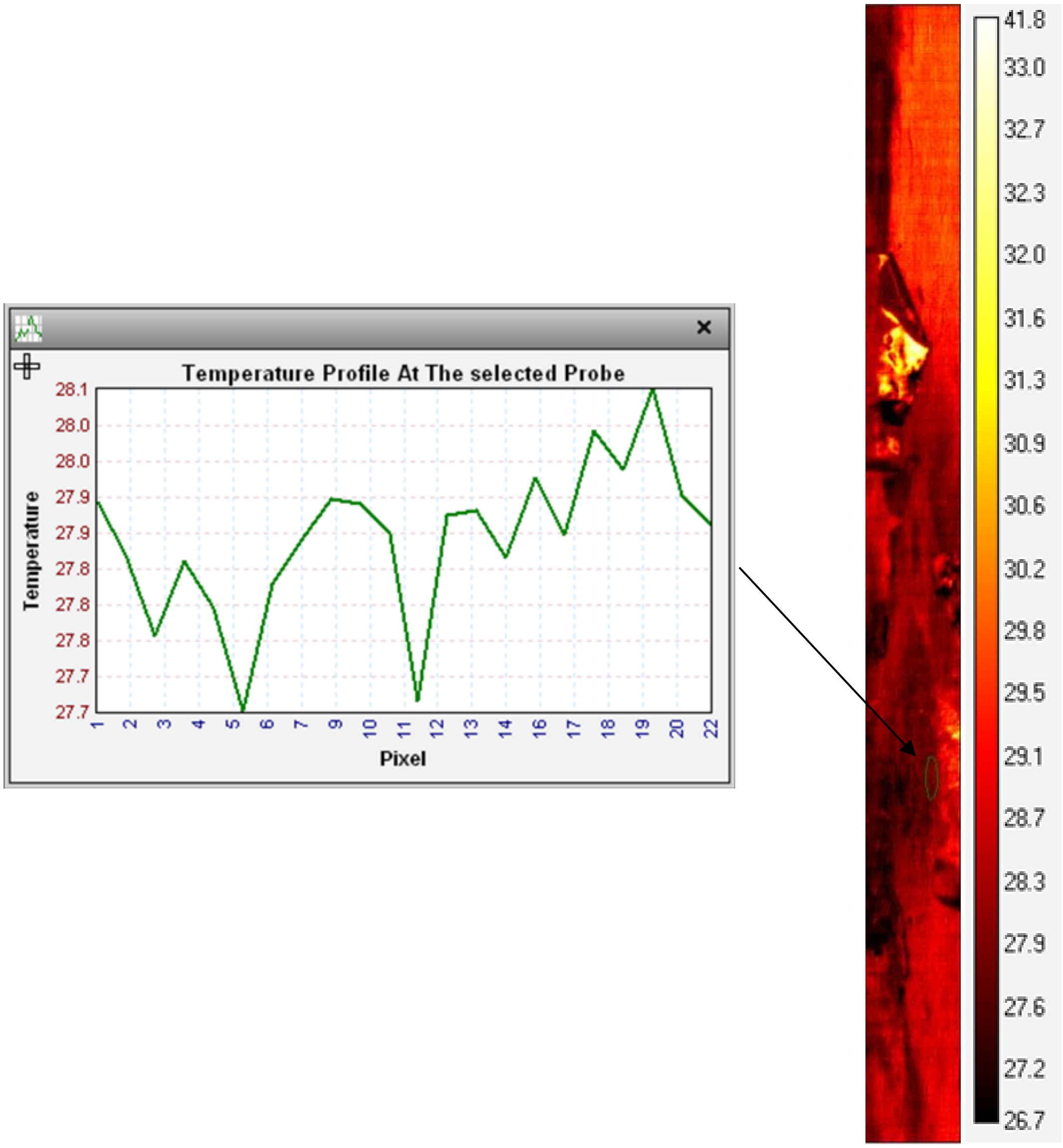

Figure B.15: IR image for heated single-phase and high Re condition (right) and the liquid temperature profile at the nucleation site (left).